

EV 619616113 US

B189RCE

IN THE UNITED STATES PATENT AND TRADEMARK OFFICE

Examiner : Marjorie A. Moran
Group : 1631
Applicants : Mihail N. Karpusas,
Juswinder Singh and
David W. Thomas
Application No. : 09/180,209
Confirmation No. : 6529
Filing Date : December 22, 1999 (RCE filed on
July 17, 2003)
For : CRYSTALS OF FRAGMENTS OF CD40
LIGAND AND THEIR USE

Mail Stop Amendment
Hon. Commissioner for Patents
P.O. Box 1450
Alexandria, Virginia 22313-1450

DECLARATION OF JUSWINDER SINGH, PH.D.
UNDER 37 C.F.R. § 1.132

I, JUSWINDER SINGH, Ph.D. hereby declare that:

1. I am one of the named inventors of the
above-identified patent application.

2. I am a scientist at Biogen Idec MA Inc.
Currently, I am the Associate Director of Computational
Drug Design at Biogen Idec MA Inc. I have a Ph.D. degree

in Rational Drug Design from the University of London.
My CV is attached at Tab A.

3. I have reviewed the January 27, 2005 Office Action in the above-identified application. I have also reviewed claims 39, 42 and 43 in their form as I understand them to be at this time, as well as at the time of that Office Action.

4. I understand that the Examiner has rejected claims 39, 42 and 43 as being obvious in view of United States patent 6,703,486 ("Mandel"). I understand that the Examiner relies on Mandel for teaching:

- a computer for producing a 3-D representation of binding and active sites of a protein;

- that such a computer may comprise a variety of programs for 3-D modeling based on atomic or X-ray coordinates;

- that the data may be carried on computer-readable media; and

- that a monitor may be used for displaying results.

I also understand that the Examiner believes: (1) that the crystal structure coordinates of CD40L recited in the claims do not functionally interact with the computer or the programs stored in the computer; and (2) that the computer or the programs are not structurally or

functionally changed by the coordinates of CD40L. As a result, the Examiner considers the crystal structure coordinates of CD40L to be nonfunctional descriptive material, which do not distinguish the claimed computers from the computers of Mandel.

5. I make this declaration to explain why the computer according to claims 39, 42 and 43, or a program contained in such a computer, interacts functionally with the novel crystal structure coordinates of human CD40L set forth in those claims and is functionally changed by them. As I explain below, a person of ordinary skill in the art as of the filing date of the pending application, and each of the applications to which this application claims priority, would appreciate that the coordinates of CD40L set forth in this application functionally interact with the computer, or the program contained in it, to produce a model which is dependent on the coordinates contained therein. Consequently, the crystal structure coordinates of CD40L should not be considered nonfunctional descriptive material and, as a result, do distinguish the computers of claims 39, 42 and 43 from the computers of Mandel.

6. Claims 39, 42 and 43 refer to a computer comprising a program for producing a 3-D representation of the specified novel binding site, molecule or molecular complex of human CD40L. The claims further state that the computer comprises a computer-readable data storage medium comprising a data storage material encoded with computer-readable data, wherein the data comprises specific and novel structure coordinates of CD40L.

7. The previously unknown structure coordinates of CD40L first described in the pending application were generated by using the technique of X-ray crystallography. Scientists use X-ray crystallography to solve and provide novel molecular structures of macromolecules.¹ The molecular structures solved by X-ray crystallography can be displayed in a computer as a three-dimensional (3-D) representation. The 3-D representations displayed by computers provide scaffolds for *in silico* drug design useful in finding new drugs for treating diseases. Only a 3-D representation

¹ See, e.g., Cantor, C.R. and Schimmel, P.R., *Biophysical Chemistry, Part II: Techniques for the Study of Biological Structure and Function*, W.H. Freeman and Company, Chapter 13, pp. 687-791 (1980), attached at Tab B.

of the structure coordinates for a particular protein, e.g. CD40L, can act as a scaffold for drug design based on that protein. No other 3-D representation is capable of substituting as a scaffold for drug design using that specific protein as a target.

8. Hence, a computer that produces a 3-D representation of a particular protein, e.g., CD40L, is a functionally unique entity as compared to a computer that produces a 3-D representation of another protein. For instance, only a computer and the structure coordinates of a particular protein can be used to perform the *in silico* manipulations on that particular protein. Thus, using a computer of the present application, one of ordinary skill in the art can mutate side-chains, perform alterations of bond lengths or angles, interactively calculate distances to identify interactions within and between atoms as the model is changed, vary conformations of amino acid residues, build ligands to fit into binding pockets, dock molecules into binding sites, and perform energy minimizations for the CD40L protein and complexes containing that protein. It is important to understand that, as illustrated in the present application, the novel structure coordinates of CD40L actually functionally integrate with the computer to provide a

dynamic 3-D representation of that particular protein. That representation in turn has a function: it can be used as a scaffold for drug design based on the particular structure of CD40L. Structure coordinates that are integrated with computers, as presently claimed, are crucial to modern-day drug design.

9. Furthermore, in modern-day science, the structure of a particular target protein need not even be displayed for a scientist to conduct *in silico* drug design on that protein. However, the computer must contain the specific structure coordinates of a particular molecule or molecular complex and have the ability to display that structure.

10. The pending application, for the first time, provided computers for producing novel 3-D representations of the specified binding sites, molecules or molecular complexes of CD40L, by converting the structure coordinates of CD40L into those representations.

11. The computers of the pending application are functionally changed by the crystal structure coordinates of CD40L as follows. The computers contain computer program(s) for displaying a 3-D representation

of a specified molecular structure, i.e., CD40L. See, for example, the description of how Molecular Graphics manipulations are performed with QUANTA software run on a Silicon Graphics Indigo2 computer (see, e.g., page 35, lines 29-32 of the application). Computer programs for visualization and molecular modeling, such as QUANTA (see the application at page 35, lines 29-32; and page 26, lines 14-21) and Sybyl (see the application at page 26, lines 14-21) are described as well. A molecular model for a novel protein is dependent on novel structure coordinates. The computer program(s) interrelate and integrate the computer and the novel structure coordinates to produce novel 3-D representations of molecular structures.² One of ordinary skill in the art can then visually inspect and dynamically interact with the 3-D representation of the particular molecular structure and use that representation for drug design. By means of such computer program(s), the computers of the present application read the specified coordinates of CD40L from memory and upon recognizing each coordinate, cause a novel 3-D representation of the specific binding

² See Lesk and Hardman, *Methods in Enzymology*, Vol. 115: pp. 381-390 (1985), attached at Tab C.

site, molecule or molecular complex of CD40L to be constructed in a proper axis system.

12. Thus, a computer according to the present application displays the particular structure of CD40L dictated by the structure coordinates of that protein. Those structure coordinates enable the computer to display 3-D representations of particular CD40L molecular structures. Such a computer may then be used for drug design involving a particular CD40L molecular structure. In contrast, another computer that is identical, except that it does not contain the claimed novel set of CD40L structure coordinates, would not display the CD40L molecular structure and could not be used for drug design involving that structure. Therefore, a computer containing the structure coordinates for CD40L is endowed with function.

13. A computer of the present application is very different from a computer/machine which produces images and sounds from a computer-readable data storage medium containing a musical, artistic or literary work. The former produces a specific 3-D representation based on the structure coordinates of CD40L, which can interactively and dynamically be used for drug design

involving the CD40L structure defined by those coordinates. As explained in detail above, such a computer can be used to manipulate the structure of CD40L, e.g., by mutating side-chains of the CD40L protein, changing conformation of amino acid residues of the CD40L protein, building ligands to fit into the binding pockets of the CD40L molecular structure, docking molecules into binding sites of the CD40L protein and performing energy minimizations for CD40L and its complexes. In contrast, a computer disk with music, a painting or a literary work stored on computer-readable data storage medium is designed only to be read by the computer and to produce sound or static two-dimensional visual or print images. In other words, unlike the computers of the present application, such a computer simply translates the data and does nothing more. Also, unlike the computers of the present application, such a computer does not produce an interactive, dynamic entity capable of functional use.

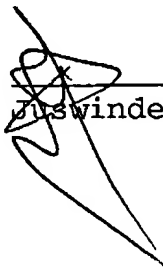
14. A computer according to the present application and the set of CD40L structure coordinates combine as a whole to produce a functional relationship and a functional entity. In this sense, the structure coordinates of CD40L are integrated into the computer,

and in fact, do functionally interact with the computer, and the computer is functionally changed by those coordinates.

15. For all of these reasons, there is no question that a functional relationship exists between the computers of claims 39, 42 and 43 and the stored structure coordinates of CD40L specified therein. The structure coordinates of CD40L integrate with those computers to produce this functional relationship. The computers are novel and represent an advancement in the art beyond the computers of Mandel. This is so because Mandel's computers do not contain the structure coordinates of CD40L recited in claims 39, 42 and 43 and, as a result, they are of no use for drug design targeting CD40L.

16. I declare further that all statements made herein of my own knowledge are true and that all statements made herein on information and belief are believed to be true; and further, that these statements were made with the knowledge that willful false statements and the like so made are punishable by fine or imprisonment, or both, under Section 1001, Title 18, United States Code, and that such willful false statements may jeopardize the validity of this application and any patent issuing thereon.

Date: 6/27/05



Jaswinder Singh, Ph.D.

JUSWINDER SINGH

WORK EXPERIENCE

OCT2000–PRESENT ASSOCIATE DIRECTOR, COMPUTATIONAL DRUG
DESIGN, BIOGEN IDEC

OCT1994–OCT2000 HEAD OF MOLECULAR MODELING, BIOGEN INC

OCT1991–OCT1994 SENIOR SCIENTIST, CADD GROUP, PARKE-DAVIS
RESEARCH

EDUCATION

1981-1984 DEPARTMENT OF BIOCHEMISTRY
UNIVERSITY OF SUSSEX, ENGLAND
B.SC. BIOCHEMISTRY (FIRST CLASS HONORS)

1984-1987 PHD. RATIONAL DRUG DESIGN, UNIVERSITY OF
LONDON
AN ANALYSIS OF SIDE CHAIN INTERACTIONS IN
PROTEIN AND ITS APPLICATION TO DRUG DESIGN:
SUPERVISED BY SIR T.L. BLUNDELL F.R.S.
(CAMBRIDGE UNIVERSITY), PROF. J. THORNTON F.R.S.
(UNIVERSITY COLLEGE LONDON) AND DR. S.
CAMPBELL F.R.S. (FORMER V.P. OF DISCOVERY
RESEARCH, PFIZER, SANDWICH, KENT)

POST-DOCTORAL EXPERIENCE

MAY87 - SEPT91 POST-DOCTORAL RESEARCH SCIENTIST
BIOMOLECULAR STRUCTURE AND MODELING GROUP
UNIVERSITY COLLEGE LONDON
SUPERVISOR: PROF. JANET THORNTON F.R.S.

PUBLICATIONS

1. **SINGH J**, THORNTON JM. "THE GEOMETRIES OF INTERACTING PHENYLALANINE RINGS IN PROTEINS," FEBS LETT 1985;191:1-6.
2. BLUNDELL TL, **SINGH J**, THORNTON JM, BURLEYSK, PETSKOGA. "AROMATIC INTERACTIONS," SCIENCE 1986;1005:234
3. **SINGH J**, THORNTON JM, SNAREY M, CAMPBELL SF. "THE GEOMETRIES OF INTERACTING ARGININE-CARBOXYLS IN PROTEINS," FEBS LETT 1987;224:161-71.
4. BLUNDELL, TL, ELLIOTT, G., GARDNER, SP, HUBBARD, T., ISLAM, S., JOHNSON, M., MANTAFOUNIS, D., MURRAY-RUST, P., OVERINGTON, J., PITTS, JE, SALI, A., SIBANDA, BL., **SINGH, J.**, STERNBERG, MJE, SUTCLIFFE, MJ., THORNTON, JM., TRAVERS, "PROTEIN ENGINEERING AND DESIGN", 1989 P. PHIL. TRANS. R. SOC. LOND. B324, 447-460
5. THORNTON JM, **SINGH J**, CAMPBELL SF, BLUNDELL TL. "PROTEIN-PROTEIN RECOGNITION VIA SIDE CHAIN-SIDE CHAIN INTERACTIONS," BIOCHEMICAL SOCIETY TRANSACTIONS 1988;16:927-93.
6. **SINGH J**, THORNTON JM. "SIRIUS-AN AUTOMATED METHOD FOR ANALYZING PROTEIN INTERACTIONS," JMOL BIOL 1990;211:595-615
7. **SINGH J**, THORNTON JM, SALDANHA JW. "A NOVEL METHOD FOR THE MODELLING OF LIGANDS TO THEIR RECEPTORS," PROTEIN ENGINEERING 1991;4:251-61.
8. HUNTER C, **SINGH J.** AND THORNTON, J.M., "ENERGETICS OF AROMATIC-AROMATIC INTERACTIONS," JMOL BIOL 1991;218, 837-849
9. **SINGH J**, NANDI L, THORNTON JM. "TOWARDS UNDERSTANDING HOW SIDE CHAINS PACK IN PROTEINS" 1991, IN "MOLECULAR CONFORMATIONS AND BIOLOGICAL INTERACTIONS", EDS., BALARAM P. AND RAMASESHAN S., BANGALORE, 1-18
10. THORNTON JM, SIBANDA BL, WILMOT CM AND **SINGH J.** "PATTERNS IN PROTEIN SEQUENCE AND STRUCTURE" SPRINGER SERIES IN BIOPHYSICS, TAYLOR WR, SPRINGER-VERLAGHD (EDS). 1991; VOLUME-6.

11. MITCHELL J, THORNTON JM, **SINGH J.** AND PRICE, S.L., "TOWARDS UNDERSTANDING THE ENERGETICS OF ARGININE-CARBOXYLATE PAIRS IN PROTEINS," J MOL BIOL 1992; **226**, 251-264
12. **SINGH J**, NANDI CL, THORNTON JM. "ATOMIC ENVIRONMENTS OF ARGININE SIDE CHAINS IN PROTEINS," PROTEIN ENGINEERING 1993, **6**, 247-259
13. **SINGH, J.** "COMPARATIVE ANALYSIS OF THE SER/THR AND TYR PROTEIN KINASES : PROPOSED MODEL FOR THE CATALYTIC DOMAIN OF THE EPIDERMAL GROWTH FACTOR RECEPTOR", PROTEIN ENGINEERING, 1994, **7**, 849-858
14. MITCHELL J.B , NANDI, C.L., PRICE S, **SINGH J**, SNAREY M AND THORNTON, J.M " A COMPARISON OF THREE THEORETICAL APPROACHES TO THE STUDY OF SIDE CHAIN INTERACTIONS IN PROTEINS " J. CHEM. SOC. FARADAY TRANS., 1993, **89**, 2619-2630
15. MITCHELL, J.B., THORNTON, J.M., PRICE, S.L., MCDONALD, I., NANDI, C.L. AND **SINGH, J.** "AROMATIC-AMINO HYDROGEN-BONDS", NATURE, 1993, 366, 413
16. MAHDEVAN, D., THANKI, N., **SINGH, J.**, WANG, A.C., MCPHEE, P., ZANGRILLI, D., WANG, L., GURRERO, C., HUMBLET, C., SALDANHA, J., AND HASKE, T. "STRUCTURAL STUDIES ON THE PH DOMAINS OF DBL, SOS1, IRS-1 AND π ARK-1 AND THEIR DIFFERENTIAL BINDING TO G α SUBUNITS", 1995, BIOCHEMISTRY, **34**, 9111-9117
17. ZHU, G., DECKER, S.J., MACLEAN, D., MCNAMARA, D.J., **SINGH, J.**, SAWYER, T.K. AND SALTIEL, A.R., 1994, "SEQUENCE SPECIFICITY IN THE RECOGNITION OF THE EPIDERMAL GROWTH FACTOR RECEPTOR BY THE ABL SRC HOMOLOGY 2 DOMAIN", ONCOGENE, **9**, 1379-1385
18. FRY, D.W., MCMICHAEL, A., **SINGH, J.**, DOBRUSIN, E.M., AND MCNAMARA, D., (1994) "DESIGN OF A POTENT PEPTIDE INHIBITOR OF THE EPIDERMAL GROWTH FACTOR RECEPTOR TYROSINE KINASE UTILIZING SEQUENCES BASED ON THE NATURAL PHOSPHORYLATION SITES OF PHOSPHOLIPASE C α 1", PEPTIDES, **15**, 951-957
19. EVANS, R.W., CRAWLEY, J.B., GARRATT, R.C., GROSSMANN, J.G., NEU, M., AITKEN, A., PATEL, K.J., MEILAK, A., WONG, C., **SINGH, J.**, BOMFORD, A. AND HUSNAIN, S.S. "CHARACTERISATION AND STRUCTURAL ANALYSIS OF A FUNCTIONAL HUMAN SERUM TRANSFERRIN VARIANT AND ITS IMPLICATIONS FOR RECEPTOR RECOGNITION", 1994, BIOCHEMISTRY, **33**, 12512-12520

20. MACLEAN, D., THIEME-SEFLER, A.M., ZHU, G., DECKER, S.J., SALTIEL, A.R., **SINGH, J.**, MCNAMARA, D., DOBRUSIN, E.M. AND SAWYER, T.K. "DIFFERENTIATION OF PEPTIDE MOLECULAR RECOGNITION BY PHOSPHOLIPASE C-1 α SRC HOMOLOGY-2 DOMAIN AND A MUTANT PHOSPHATASE PTP1B^{C215S}", 1995, PROTEIN SCIENCE, 4, 13-20
21. NARASIMHAN, L., **SINGH, J.**, HUMBLET, C., GURUPRASAD, K. AND BLUNDELL, T.L. "SNAIL AND SPIDER TOXINS SHARE SIMILAR STRUCTURE AND 'CYSTINE PATTERN'", 1995, NATURE STRUCTURAL BIOLOGY, 1, 850-852
22. SHAHRIPOUR, A., PLUMMER, M.S., LUNNEY, E.A., VARA PRASAD J.V.N., **SINGH, J.**, PARA, K.S., STANKOVIC, C.J., EATON, S.R., RUBIN, J.R., PAVLOVSKY, A.G., HUMBLET, C., FERGUS, J.H., MARKS, J.S., DECKER, S.J., HERRERA, R., HUBBELL, S., SALTIEL, A.R., AND SAWYER, T.K. (1995) "NOVEL PHOSPHOTYROSINE AND HYDROPHOBIC D-AMINO ACID REPLACEMENTS IN THE DESIGN OF PEPTIDE LIGANDS FOR PP60^{SRC} SH2 DOMAIN", PEPTIDES: CHEMISTRY, STRUCTURE AND BIOLOGY, 394-396
23. PLUMMER, M.S., LUNNEY, E.A., PARA, K.S., VARA PRASAD J.V.N., SHAHRIPOUR A., **SINGH, J.**, STANKOVIC, C.J., HUMBLET, C., FERGUS, J.H., MARKS, J.S., AND SAWYER, T.K. (1995) "HYDROPHOBIC D-AMINO ACIDS IN THE DESIGN OF PEPTIDE LIGANDS FOR THE PP60SRC SH2 DOMAIN", DRUG DESIGN AND DISCOVERY, 13,75-81
24. LASKWOSKI, R.A., THORNTON, J., HUMBLET, C. AND **SINGH, J.** (1996) "XSITE: USE OF EMPIRICALLY DERIVED ATOMIC PACKING PREFERENCES TO IDENTIFY FAVOURABLE INTERACTION REGIONS IN THE BINDING SITES OF PROTEINS', J. MOL. BIOL., 259, 175-201
25. **SINGH, J.**, FRY, D., DOBRUSIN, E., WHITTY, A., HASKE, T. AND MCNAMARA, D. (1997) "STRUCTURE-BASED DESIGN OF A POTENT, SELECTIVE AND IRREVERSIBLE INHIBITOR OF THE ERBB RECEPTOR SUBFAMILY OF PROTEIN TYROSINE KINASES", J. MED. CHEM, 40, 1130-1135
26. WALLACE, A., LASKOWSKI, R.A., **SINGH, J.** AND THORNTON, J. (1996) 'MOLECULAR RECOGNITION BY PROTEINS: PROTEIN-LIGAND INTERACTIONS FROM A STRUCTURAL PERSPECTIVE", BIOCHEMICAL SOCIETY TRANSACTIONS, 24, 280-284
27. **SINGH, J** ET AL. (1998) 'THE ROLE OF POLAR INTERACTIONS IN THE MOLECULAR RECOGNITION OF CD40L WITH ITS COUNTER-RECEPTOR CD40", PROTEIN SCIENCE, 7:1124-1135
28. SALDANHA, J., **SINGH, J.** AND MAHADEVAN, M. (1998) 'FRIZZLED-LIKE CYSTEINE-RICH DOMAIN IN THE EXTRACELLULAR REGION OF DEVELOPMENTAL TYROSINE KINASES', 7, PROTEIN SCIENCE, 1632-1635

29. GOTWALS, P., CHI-ROSSO, G., RYAN, S.T., SIZING, I., ZAFARI, M., BENJAMIN, C., **SINGH, J.**, VENYAMINOV, S.Y., PEPINSKY, R.B. AND KOTELIANSKY, 1999, 'Divalent cations stabilize the A4B1 integrin I domain', *BIOCHEMISTRY*, 38, 8280-8288
30. **SINGH, J.**, VAN VLIJMEN, H., LEE, WC, LIAO, Y., LIN, KC, ATEEQ, H., CUERVO, H., ZIMMERMAN, C., HAMMOND, C., KARPUSAS, M., PALMER, R., CHATTOPADHYAY, T., AND ADAMS, SP 2002 J. COMPUTER-AIDED MOLECULAR DESIGN, "3D-QSAR (COMFA) OF A SERIES OF POTENT AND HIGHLY SELECTIVE VLA4 ANTAGONISTS", 16, 201-211
31. **SINGH, J.**, VAN VLIJMEN, H., LIAO, Y., LEE, WC, CORNEBISE, M., HARRIS, M., SHU, I., GILL, A., CUERVO, J., ABRAHAM, WM, AND ADAMS, SP 2002 "IDENTIFICATION OF POTENT AND NOVEL $\alpha 4\beta 1$ ANTAGONISTS USING IN SILICO SCREENING", *J. MED. CHEM.*, 45:2988-299
32. FOLEY, S., VAN VLIJMEN, H., BOYNTON, R.E., ADKINS, H.B., CHEUNG, A.E., **SINGH, J.**, SANICOLA, M., YOUNG, C.N., WEN, D. 2003 "THE CRIPTO/FRL-1/CRYPTIC (CFC) DOMAIN OF HUMAN CRIPTO: FUNCTIONAL AND STRUCTURAL INSIGHTS THROUGH DISULFIDE STRUCTURE ANALYSIS", *EUR. J. BIOCHEM.*, 270, 3610-3618
33. **SINGH, J.**, CLAUDIO A. CHUAQUI, P. ANN BORIACK-SJODIN, WEN-CHERNG LEE, MICHAEL J. CORBLEY, H.-KAM CHEUNG, SERENE JOSIAH, ROBERT M. ARDUINI, JONATHAN N. MEAD, MIKI NEWMAN, JAMES L. PAPADATOS AND LEONA E. LING, 2003, SUCCESSFUL SHAPE-BASED VIRTUAL SCREENING: THE DISCOVERY OF A POTENT INHIBITOR OF THE TYPE I TGF β RECEPTOR KINASE (T β RI), *BIOORGANIC MEDICINAL CHEMISTRY LETTERS*, 2003, 13, 4355-4359
34. DENG, Z., CHUAQUI, C. AND **SINGH, J.** 2004, STRUCTURAL INTERACTION FINGERPRINT (SIFT): A NOVEL METHOD FOR ANALYZING THREE-DIMENSIONAL PROTEIN-LIGAND BINDING INTERACTIONS, *J. MED. CHEM.*, 47, 337-344
35. VAN VLIJMEN, H. GUPTA, A., NARASIMHAN, L. AND **SINGH, J.** 2004, UNCOVERING HOMOLOGS THROUGH DISULFIDE BOND SIMILARITY, *J. MOL. BIOL.*, 335, 1083-1092
36. GUPTA, A. VAN VLIJMEN, H., **SINGH, J.** 2004, A CLASSIFICATION OF DISULFIDE PATTERNS AND ITS RELATIONSHIP TO PROTEIN STRUCTURE AND FUNCTION, *PROTEIN SCIENCE*, 13, 2045-2058
37. D. N. CHIN; C. E. CHUAQUI; AND **SINGH, J.** 2004, INTEGRATION OF VIRTUAL SCREENING INTO THE DRUG DISCOVERY PROCESS, *MINI-REVIEWS IN MEDICINAL CHEMISTRY*, 4, 1053-1065

38. **SINGH, J.**, STEVE ADAMS, MARY BETH CARTER, HERNAN CUERVO, WENCHERNG LEE, ROY R. LOBB, R. BLAKE PEPINSKY, RUSSELL PETTER AND DANIEL SCOTT, 2004 RATIONAL DESIGN OF POTENT AND SELECTIVE VLA-4 INHIBITORS AND THEIR UTILITY IN THE TREATMENT OF ASTHMA, CURRENT TOPICS IN MEDICINAL CHEMISTRY, 4, 1497-1507
39. **SINGH, J.**, LING, L.E., SCOTT-SAWYER, J.S., LEE, W.C., ZHANG, F. AND YINGLING, J.M. TRANSFORMING THE TGF β PATHWAY: CONVERGENCE OF DISTINCT LEAD GENERATION STRATEGIES ON A NOVEL KINASE PHARMACOPHORE FOR TBRI, CURRENT OPINIONS IN DRUG DISCOVERY AND DEVELOPMENT, 2004, 7(4), 1367
40. CHUAQUI, C., DENG, Z. AND **SINGH, J.** 2005, INTERACTION PROFILES OF PROTEIN KINASE-INHIBITOR COMPLEXES AND THEIR APPLICATION TO VIRTUAL SCREENING, J. MED. CHEM, 28, 121-133
41. DENG, Z., CHUAQUI, C. AND **SINGH, J.** KNOWLEDGE-BASED DESIGN OF TARGET-FOCUSED LIBRARIES USING PROTEIN-LIGAND INTERACTION CONSTRAINTS, J. MED. CHEM. SUBMITTED
42. **SINGH, J.**, CHUAQUI, C AND DENG, Z., EXTENDED ABSTRACT FOR 40TH QSAR CONFERENCE, IN THE PRESS
43. **SINGH, J.**, CHUAQUI, C. AND DENG, Z., 2005, "SIFTING FOR PROTEIN KINASE INHIBITORS", "PHARMACOPHORES AND PHARMACOPHORE SEARCHES" EDITORS VON THIERRY LANGER UND RÉMY D. HOFFMANN IN THE SERIES "METHODS AND PRINCIPLES IN MEDICINAL CHEMISTRY", IN THE PRESS
44. **SINGH, J.** SUCCESSFUL VIRTUAL SCREENING, CHEMISTRY TODAY, IN THE PRESS

BOOKS

45. **SINGH J** AND THORNTON JM. "AN ATLAS OF SIDE CHAIN PACKING IN PROTEINS," VOLUMES I AND II, OXFORD UNIVERSITY PRESS, 1992, ISBN 0-19-0963302-9.

PATENTS

46. **US 6306840** CELL ADHESION INHIBITORS
47. **US 6552216** MOLECULAR MODEL FOR VLA-4 CELL ADHESION INHIBITORS
48. **US 6376538** ANTIINFLAMMATORY AGENTS; AUTOIMMUNE DISEASES
49. **US 5922697** COMPOUNDS, COMPOSITIONS AND METHODS FOR INHIBITING THE BINDING OF PROTEINS CONTAINING AN SH2 DOMAIN TO COGNATE PHOSPHORYLATED PROTEINS
50. **WO 200508240** STRUCTURAL INTERACTION FINGERPRINT (SIFT)

51. **WO 200472033** PYRAZOLES AND METHODS OF MAKING AND USING THE SAME
52. **WO 200421989** IMIDAZOLOPYRIDINES
53. **WO 200422054** PYRAZOLOPYRIDINES
54. **WO 9700895** CRYSTALS OF FRAGMENTS OF CD40 LIGAND AND THEIR USE
55. **WO 9411392** PEPTIDE INHIBITORS OF TYROSINE KINASES AND THERAPEUTIC USES THEREOF

2004 INVITED PRESENTATIONS

- CHI STRUCTURE-BASED DESIGN CONFERENCE, BOSTON, 2004 "SIFT: A NOVEL TOOL FOR ANALYZING PROTEIN-LIGAND INTERACTIONS"
 - SYMPOSIUM CHAIR AND SPEAKER DRUG DESIGN TECHNOLOGIES WORLD CONGRESS, BOSTON, 2004 "DISCOVERY OF A POTENT SELECTIVE INHIBITOR OF T β RI USING VIRTUAL SCREENING"
 - PLENARY SPEAKER KEYSTONE SYMPOSIUM ON STRUCTURAL GENOMICS "A NOVEL DATABASE OF DISULFIDE PATTERNS AND ITS APPLICATION TO STRUCTURAL GENOMICS"
 - 40TH ANNIVERSARY OF QSAR "SIFT-BASED PROFILES AND THEIR APPLICATION TO LEAD DISCOVERY IN THE KINASE FAMILY"
 - ACS FLORIDA 2004 "INTEGRATED VIRTUAL CHEMISTRY"
-

TAB B

BIOPHYSICAL CHEMISTRY

PART

II

TECHNIQUES FOR THE STUDY OF BIOLOGICAL STRUCTURE AND FUNCTION

Charles R. Cantor

COLUMBIA UNIVERSITY

Paul R. Schimmel

MASSACHUSETTS INSTITUTE OF TECHNOLOGY



W. H. FREEMAN AND COMPANY

New York

Cover drawing after R. D. B. Fraser and T. P. McRae.
in *Physical Principles and Techniques of Protein
Chemistry*, part A, ed. S. J. Leach (New York:
Academic Press, 1969).

Sponsoring Editor: Arthur C. Bartlett
Project Editor: Pearl C. Vapnek
Manuscript Editor: Lawrence W. McCombs
Designer: Robert Ishi
Production Coordinator: Linda Jupiter
Illustration Coordinator: Cheryl Nufer
Artists: Irving Geis and Eric Hieber
Compositor: Syntax International
Printer and Binder: R. R. Donnelley & Sons Company

Figures 13-17, 13-19
copyright © 1980 by Irving Geis.

Library of Congress Cataloging in Publication Data

Cantor, Charles R 1942—
Techniques for the study of biological structure and
function.

(Their Biophysical chemistry: pt. 2)

Includes bibliographies and indexes.

1. Molecular biology—Technique. 2. Biological
chemistry—Technique. I. Schimmel, Paul Reinhard,
1940— joint author. II. Title.

QH345.C36 pt. 2 [QH506] 574.1'9283s [574.1'9283]

ISBN 0-7167-1189-3

79-24854

ISBN 0-7167-1190-7 pbk.

Copyright © 1980 by W. H. Freeman and Company

No part of this book may be reproduced by any mechanical,
photographic, or electronic process, or in the form of a
phonographic recording, nor may it be stored in a retrieval
system, transmitted, or otherwise copied for public or private
use, without written permission from the publisher.

Printed in the United States of America

4 5 6 7 8 9 0 DO 4 3 2 1 0 8 9 8 7 6

13-1 X-RAY SCATTERING BY ATOMS AND MOLECULES

X-ray diffraction is the most powerful technique currently available for studying the structure of large molecules. In many cases, x-ray diffraction studies on protein or nucleic acid crystals have yielded the complete tertiary structure at a level of resolution of 3 Å or better. If only a less-well-ordered sample (such as an oriented fiber) is available, x-ray diffraction still provides a wealth of structural information. Though insufficient to determine the structure uniquely, this information in many cases can provide decisive tests of structural models. Here we develop the theory of x-ray diffraction and describe some of the steps involved in obtaining structures from diffraction data.

Outline and limitations of our treatment

As one might expect, a technique that can provide so many structural details is intrinsically rather complex. We omit as many of the complications as possible and try to focus on the essential features of the method. Thus, atoms are treated as motionless, even though in crystals there is appreciable motion at finite temperatures. Crystals are treated as perfectly ordered arrays, even though they may actually be ordered only in local domains, X-ray radiation is treated as monochromatic, even though a distribution of wavelengths is always used in practice. Finally, diffraction data are considered

to be very precise, even though experimental errors often are a significant problem in practice.

To understand x-ray diffraction, one must know how x rays interact with atoms and the manner in which atoms can be organized into crystals. Most traditional descriptions of the technique start with a discussion of the symmetry and structure of crystals. Diffraction of x rays is described in terms of reflections from crystal planes. The structure of molecules within the crystal is introduced into the discussion only later. The reader probably has seen this approach before in more elementary texts. Here we use a different approach, elaborated by H. Lipson and C. A. Taylor (1958). The x-ray scattering of single atoms is explained. Then we build in complexity to describe the x-ray scattering of sets of atoms (one-dimensional arrays) and, finally, of the three-dimensional arrays found in crystals. Although this treatment requires somewhat more sophisticated mathematics, there seems to be a consensus among practicing crystallographers that it ultimately affords much greater insight and understanding.

X rays: short-wavelength electromagnetic radiation

X rays are photons with wavelengths in the range of 0.1 Å to 100 Å. They usually are generated by bombarding a target with electrons of energies of 10,000 electron volts (eV) or more. Upon collision, these high-energy electrons can knock electrons out of the target atoms, leaving vacancies in atomic shells. If, for example, a vacancy is produced in the innermost (*K*) shell of an atom, it rapidly will be filled by an electron descending from the next (*L*) shell, or one from the one after that (*M*). The photons emitted as a result of these transitions are called, respectively, K_α and K_β x rays. Their wavelengths are

$$\lambda_{K_\alpha} = hc/(E_L - E_K) \quad \text{and} \quad \lambda_{K_\beta} = hc/(E_M - E_K) \quad (13-1)$$

where h is Planck's constant, c is the speed of light, and E refers to the energy of a particular state (*K*, *L*, or *M*). Typical x rays used in structure determination are Cu K_α ($\lambda = 1.54$ Å) and Mo K_α ($\lambda = 0.71$ Å).

Parameters that describe an electromagnetic wave

X rays, like any other photons, are electromagnetic waves. A general expression for the propagation of one such wave in the \mathbf{k} direction through space and time is

$$\begin{aligned} E(\mathbf{r}, t) &= E_0 e^{2\pi i(\mathbf{k} \cdot \mathbf{r}/\lambda - \nu t + \delta')} \\ &= E_0 \{ \cos[2\pi(\mathbf{k} \cdot \mathbf{r}/\lambda - \nu t + \delta')] + i \sin[2\pi(\mathbf{k} \cdot \mathbf{r}/\lambda - \nu t + \delta')] \} \quad (13-2) \end{aligned}$$

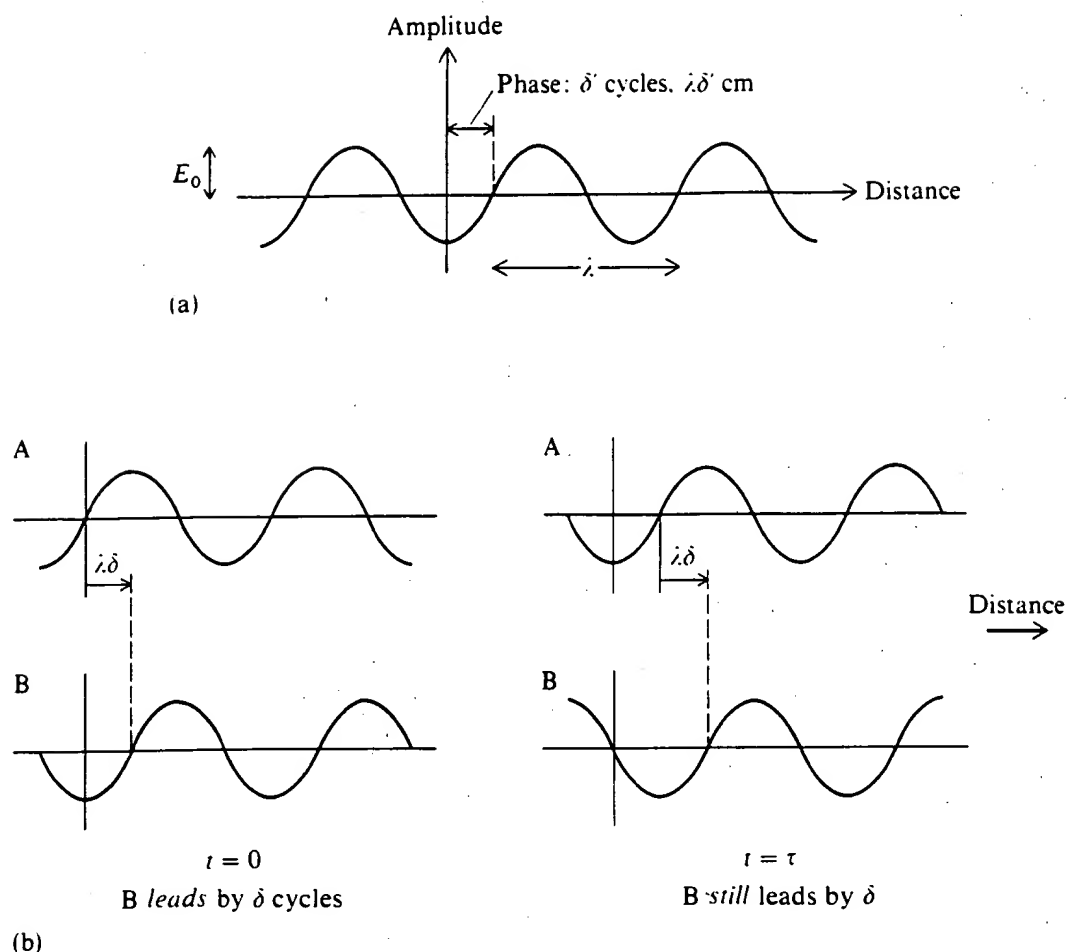


Figure 13-1

Characteristics of electromagnetic waves. (a) The electric field amplitude as a function of distance at time zero. (b) The relative phase of two waves remains constant with time. The phase difference is δ cycles ($\lambda\delta$ cm) both at $t = 0$ and at t .

where $E(\mathbf{r}, t)$ is the electric field at point \mathbf{r} and time t ; $\hat{\mathbf{k}}$ is a unit vector in the \mathbf{k} direction; λ is the wavelength in cm cycle $^{-1}$; ν is the frequency in cycles sec $^{-1}$ past a fixed point; δ' is the phase of the wave (in cycles) that defines its amplitude at $\mathbf{r} = 0$ and $t = 0$; and E_0 is the maximal amplitude (Fig. 13-1). Such a transverse wave oscillates periodically in both time and space.

It would be equally accurate to describe the wave by a real function, such as $\sin[2\pi(\hat{\mathbf{k}} \cdot \mathbf{r}/\lambda - \nu t + \delta')]$, rather than by a complex function (Box 13-1). However, the measured radiation intensity of a wave depends on the square of the amplitude, and this always will be a real quantity. We choose to describe x rays by complex exponentials because of the great mathematical convenience of working with such functions. For example, $e^{a+b} = e^a e^b$, whereas $\sin(a+b) = \sin a \cos b + \cos a \sin b$.

Two waves propagating in the same direction with the same amplitude, wave-

length, and frequency can differ only in phase. We can describe them as

$$E_1(\mathbf{r}, t) = E_0 e^{2\pi i(\mathbf{k} \cdot \mathbf{r}/\lambda - \nu t + \delta'_1)}$$

$$E_2(\mathbf{r}, t) = E_0 e^{2\pi i(\mathbf{k} \cdot \mathbf{r}/\lambda - \nu t + \delta'_2)} = E_1(\mathbf{r}, t) e^{2\pi i\delta}$$

where $\delta = \delta'_2 - \delta'_1$ is the phase shift. Note that δ is constant for all space and time. If two such phase-shifted waves are combined, the net amplitude is $E_1(\mathbf{r}, t)(1 + e^{2\pi i\delta})$. When δ is zero, this net amplitude is just twice the individual amplitude but, when δ is one-half cycle, the net amplitude is zero because $e^{i\pi}$ is -1 . Clearly, in situations where an observable is a superposition of many waves, their relative phases are quite critical.

Geometry of an x-ray scattering experiment

Consider the geometry of the typical x-ray scattering experiment shown in Figure 13-2a. A collimated beam of x rays is allowed to impinge on a sample consisting of a

Box 13-1 RELATIONSHIP BETWEEN SINES, COSINES, AND EXPONENTIALS

It is possible to express periodically varying functions either in terms of sines and cosines or as complex exponentials. The basic relationship between these two representations is

$$e^{ix} = \cos x + i \sin x$$

One easy way to justify this relationship is to expand each of the functions in an infinite series:

$$e^{ix} = 1 + ix - x^2/2! - ix^3/3! + x^4/4! + ix^5/5! - \dots$$

$$\cos x = 1 - x^2/2! + x^4/4! - x^6/6! + \dots$$

$$i \sin x = ix - ix^3/3! + ix^5/5! - ix^7/7! + \dots$$

Because $\cos(-x) = \cos x$, and $\sin(-x) = -\sin x$, it is obvious that

$$e^{-ix} = \cos x - i \sin x$$

Therefore, we can always represent trigonometric functions in terms of complex exponentials as follows:

$$\cos x = (1/2)(e^{ix} + e^{-ix})$$

$$\sin x = (1/2i)(e^{ix} - e^{-ix})$$

single electron located at the origin of the coordinate system. A unit vector, \hat{s}_0 , describes the direction of the incoming radiation. Scattering will deflect a certain fraction of the incident x rays, and will lead to radiation propagating away from the sample in all directions. Suppose we could place an x-ray detector at some location in space and measure the amplitude and phase of radiation scattered in that direction. The position of the detector is denoted by another unit vector, \hat{s} . The scattering angle θ is defined as one-half the angle of deflection of \hat{s} relative to \hat{s}_0 (Fig. 13-2a). We are

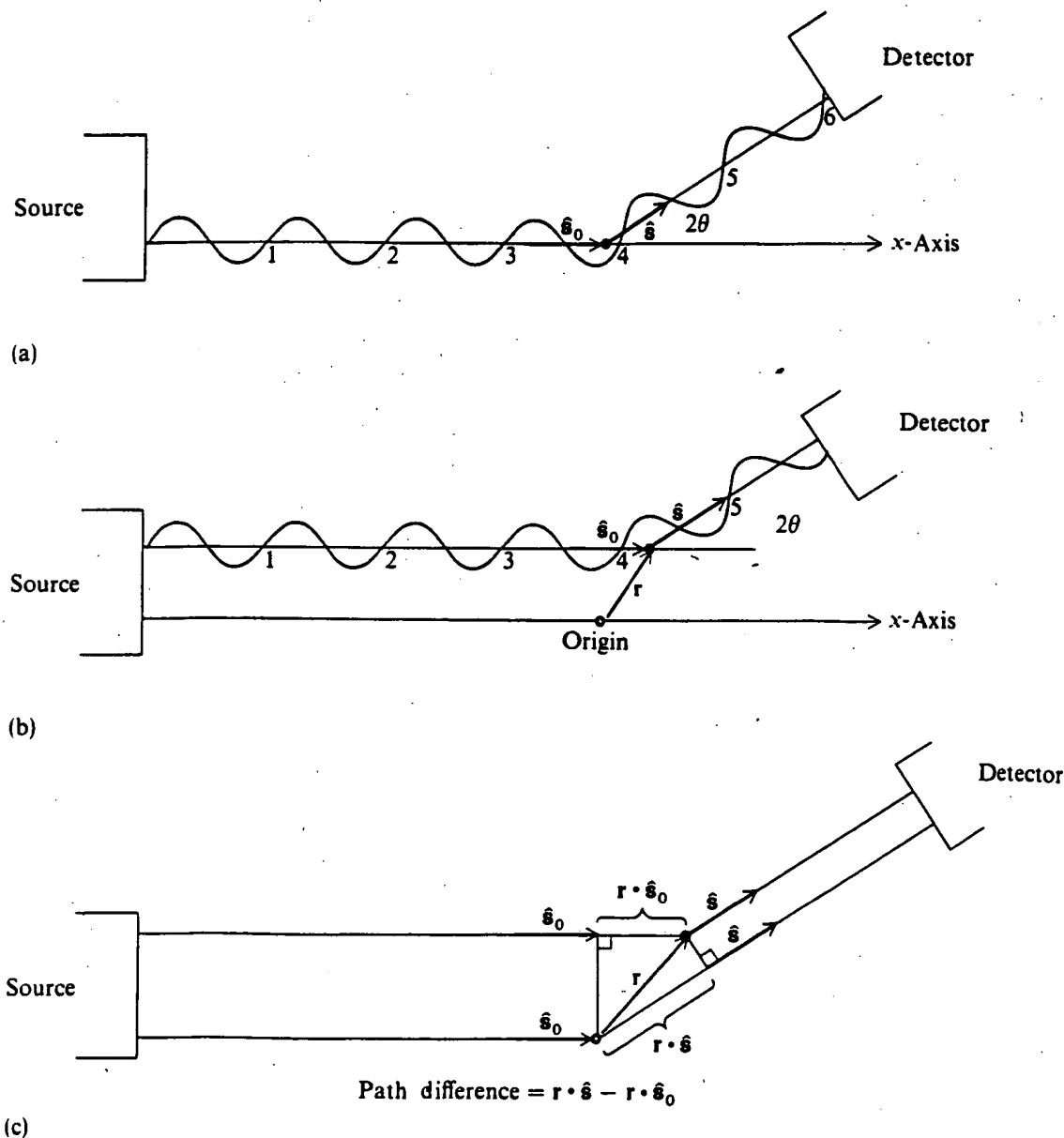


Figure 13-2

X-ray scattering by a single electron. The angle of deflection (2θ) between the source and the detector is the same in all three cases. (a) An electron at the origin. (b) An electron located at position r relative to the origin. (c) An expanded view near the origin, showing the path difference between radiation scattered by an electron at r and that scattered by an electron at the origin. The numbers shown in parts a and b measure the x-ray path in units of wavelength. The vectors \hat{s}_0 and \hat{s} are unit vectors describing the direction of incident rays and that of scattered rays seen by the detector, respectively.

concerned here only with the elastic scattering of x rays. This means that the wavelength of the incident and scattered radiation is the same.

The intensity of x-ray scattering will depend on the orientation of the sample relative to the incident and scattered rays. It is convenient mathematically and, as you will see shortly, very convenient conceptually to define a new single variable S , called the scattering vector:

$$\mathbf{S} = (\hat{\mathbf{s}}/\lambda) - (\hat{\mathbf{s}}_0/\lambda) \quad (13-3)$$

Figure 13-3a shows the meaning of S . The direction of S bisects the angle between incident and scattered radiation. The dimensions of S are inverse length, so that S measures the number of cycles of radiation per cm. The length of S is a function of the total scattering angle (Fig. 13-3b).

$$\begin{aligned} \mathbf{S} \cdot \mathbf{S} &= (\hat{\mathbf{s}}^2 + \hat{\mathbf{s}}_0^2 - 2\hat{\mathbf{s}} \cdot \hat{\mathbf{s}}_0)/\lambda^2 \\ &= 2(1 - \cos 2\theta)/\lambda^2 = (4 \sin^2 \theta)/\lambda^2 \end{aligned} \quad (13-4)$$

Therefore the length of S is

$$|\mathbf{S}| = 2|\sin \theta|/\lambda \quad (13-5)$$

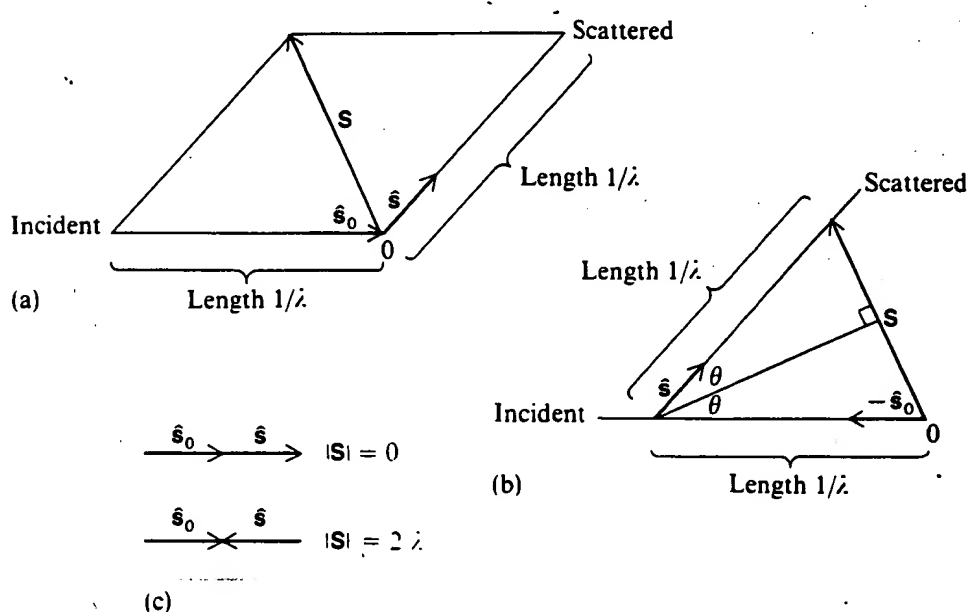


Figure 13-3

Basic geometry of an x-ray scattering experiment. The unit vectors $\hat{\mathbf{s}}_0$ and $\hat{\mathbf{s}}$ are defined in Figure 13-2. (a) The scattering vector S is defined by Equation 13-3. (b) When the unit vector $\hat{\mathbf{s}}$ describing the direction of scattered radiation is translated a distance $1/\lambda$ along the $\hat{\mathbf{s}}_0$ axis, it points directly toward the tip of the scattering vector S . (c) Arrangements of $\hat{\mathbf{s}}_0$ and $\hat{\mathbf{s}}$ that lead to maximal and minimal values of $|\mathbf{S}|$.

The value of $|\mathbf{S}|$ can vary from 0 to $2/\lambda$ (Fig. 13-3c). Thus, the vector \mathbf{S} is described in a finite coordinate system in which each axis has the dimensions of a reciprocal distance. This coordinate system is called reciprocal space. Like any other coordinate system, the space containing \mathbf{S} can be expressed by many different possible axes. We derive later a particularly convenient representation that allows \mathbf{S} to be related to the axes of a crystalline sample.

Scattering as a function of electron position

The radiation $E(\mathbf{S})$ seen by the detector (Fig. 13-2a) that results from the scattering of a single electron at the origin can be computed by a proper consideration of the quantum mechanics of photons interacting with matter.⁶ If we had more than one electron located at the origin, the scattered radiation at any angle should simply increase in amplitude in direct proportion to the number of electrons.

In crystallography, one is interested not so much in the scattering properties of individual electrons as in the effect of relative electron position on the pattern of scattering. Therefore, we can simply ask how the scattering changes as an electron is moved away from the origin. The structure factor, $F(\mathbf{S})$, is defined as the ratio of the radiation scattered by any real sample to that scattered by a single electron at the origin.

Suppose a sample contains a single electron located at position \mathbf{r} , instead of at the origin (Fig. 13-2b). The source and detector are very far away from the sample, and are large compared to \mathbf{r} . Therefore, to a very good approximation, the scattering angle, $\theta = (1/2) \cos^{-1}(\hat{\mathbf{s}} \cdot \hat{\mathbf{s}}_0)$, is the same for this sample as it is for a sample with an electron at the origin. The only difference in the two samples is the path length that x rays must travel from source to sample to detector. This path length is simply $(\hat{\mathbf{s}} - \hat{\mathbf{s}}_0) \cdot \mathbf{r}$ (Fig. 13-2c). Such a path length is equal to $(\hat{\mathbf{s}} - \hat{\mathbf{s}}_0) \cdot \mathbf{r} / \lambda = \mathbf{S} \cdot \mathbf{r}$ cycles, for x rays of wavelength λ . Therefore, if the radiation scattered by an electron at the origin is $E(\mathbf{S})$, moving the electron from the origin to a position \mathbf{r} simply causes a phase shift of $\mathbf{S} \cdot \mathbf{r}$ cycles. The scattered radiation is $E(\mathbf{S})e^{2\pi i \mathbf{S} \cdot \mathbf{r}}$, and the structure factor $F(\mathbf{S})$ is $e^{2\pi i \mathbf{S} \cdot \mathbf{r}}$.

In general, because electrons are not localized, it is better to describe an electron density $\rho(\mathbf{r})$ in a volume element $d\mathbf{r}$, located at \mathbf{r} ; the scattering then is proportional to $\rho(\mathbf{r})d\mathbf{r}$. For continuous electron density at position \mathbf{r} , the structure factor is

$$F(\mathbf{S}) = \rho(\mathbf{r})e^{2\pi i \mathbf{S} \cdot \mathbf{r}} d\mathbf{r} \quad (13-6)$$

where $\rho(\mathbf{r})d\mathbf{r}$ is the number of electrons in the volume element $d\mathbf{r}$.

A sample with many discrete scattering sites has a structure factor that is simply a sum over many terms corresponding to Equation 13-6. For a continuous electron

⁶ The result shown in Figure 13-2a contains one serious oversimplification. In actuality, all scattered radiation experiences a phase shift of one-half cycle relative to the phase of the exciting radiation. We can ignore this.

distribution, the sum is replaced by an integral:

$$F(\mathbf{S}) = \int d\mathbf{r} \rho(\mathbf{r}) e^{2\pi i \mathbf{S} \cdot \mathbf{r}} \quad (13-7)$$

The integral is taken over the entire sample. Equation 13-7 is the single fundamental equation that governs all x-ray scattering and diffraction. If the electron density distribution $\rho(\mathbf{r})$ of a sample is known, one can compute the structure factor, and from this one can compute the expected x-ray scattering for all scattering geometries.

X-ray scattering in terms of Fourier transforms

The mathematical form of Equation 13-7 is equivalent to a Fourier transform. This is an integral with very convenient properties (Box 13-2). Note that, outside the sample, $\rho(\mathbf{r})$ is zero. Therefore, the integral in Equation 13-7 can be extended over all space without changing its value. Thus, the physical meaning of Equation 13-7 is that the structure factor is a Fourier transform of the object.

Because $F(\mathbf{S})$ is the Fourier transform of $\rho(\mathbf{r})$, a second Fourier integral must exist that relates these two quantities. This is the inverse Fourier transform:

$$\rho(\mathbf{r}) = (1/V) \int d\mathbf{S} e^{-2\pi i \mathbf{S} \cdot \mathbf{r}} F(\mathbf{S}) \quad (13-8)$$

The integral is taken over all reciprocal space. V is a constant that contains $(2\pi)^3$ and other constants that compensate for the difference in the unit of volume of sample space \mathbf{r} and reciprocal space \mathbf{S} . In what follows, we sometimes ignore the constant V .

Equation 13-8 means that, if one had measured or calculated values of $F(\mathbf{S})$ extending over all reciprocal space, one could readily compute the electron density distribution of the object. Thus, Equations 13-7 and 13-8 form a relationship that lets one interconvert structure factors and electron densities freely, providing each is known over all space. It is similar in spirit to the relationship given by the Kronig-Kramers transforms in Chapter 8, which let CD and ORD data be interconverted.

An example of the properties of Fourier transforms

To illustrate the properties of Equations 13-7 and 13-8, we shall derive the latter from the former. Set up the integral $I(\mathbf{r}') = \int F(\mathbf{S}) d\mathbf{S} e^{-2\pi i \mathbf{S} \cdot \mathbf{r}'}$ in some new coordinate

system \mathbf{r}' . Substitute for $F(\mathbf{S})$ from Equation 13-7:

$$I(\mathbf{r}') = \int d\mathbf{S} e^{-2\pi i \mathbf{S} \cdot \mathbf{r}'} \int d\mathbf{r} \rho(\mathbf{r}) e^{2\pi i \mathbf{S} \cdot \mathbf{r}} \quad (13-9)$$

We can exchange the order of the two integrals to write

$$I(\mathbf{r}') = \int d\mathbf{r} \rho(\mathbf{r}) \int d\mathbf{S} e^{-2\pi i \mathbf{S} \cdot \mathbf{r}'} e^{2\pi i \mathbf{S} \cdot \mathbf{r}} = \int d\mathbf{r} \rho(\mathbf{r}) \int d\mathbf{S} e^{2\pi i \mathbf{S} \cdot (\mathbf{r} - \mathbf{r}')} \quad (13-10)$$

The integral over $d\mathbf{S}$ in the right-hand expression of Equation 13-10 has a very unusual property. As shown in Box 13-3, it is the Dirac delta function:

$$\delta(\mathbf{r} - \mathbf{r}') = \int d\mathbf{S} e^{2\pi i \mathbf{S} \cdot (\mathbf{r} - \mathbf{r}')} \quad (13-11)$$

This function has the following characteristics. If $\mathbf{r} \neq \mathbf{r}'$, then $\delta(\mathbf{r} - \mathbf{r}') = 0$. If $\mathbf{r} = \mathbf{r}'$, then $\delta(\mathbf{r} - \mathbf{r}') = \infty$. However, $\int d\mathbf{r} \delta(\mathbf{r} - \mathbf{r}') = 1$ and [for some arbitrary function $g(\mathbf{r})$] $\int d\mathbf{r} g(\mathbf{r}) \delta(\mathbf{r} - \mathbf{r}') = g(\mathbf{r}')$ if the integrals include the point $\mathbf{r} = \mathbf{r}'$. Thus, $\delta(\mathbf{r} - \mathbf{r}')$ will simply sample a function at $\mathbf{r} = \mathbf{r}'$. Equation 13-10 becomes $I(\mathbf{r}') = \rho(\mathbf{r}')$. Recognizing that \mathbf{r} and \mathbf{r}' are equivalent variables, this result is identical to Equation 13-8 except for the constant V .

Measuring the structure factor

Unfortunately for x-ray scattering studies, no way is known to measure $F(\mathbf{S})$ directly. F is a complex number that can be written as the product of two terms,

$F = |F| e^{i\phi}$

(13-12)

or as the sum of real and imaginary parts,

$$F = F_r + iF_i \quad (13-13)$$

The term $|F|$ is called the amplitude of the structure factor, and $e^{i\phi}$ is the phase. Figure 13-4 shows the relationship between the two representations of $F(\mathbf{S})$.

$$F_r = |F| \cos \phi; \quad F_i = |F| \sin \phi \quad (13-14)$$

$$|F| = (F_r^2 + F_i^2)^{1/2}; \quad \phi = \tan^{-1}(F_i/F_r) \quad (13-15)$$

Box 13-2 PROPERTIES OF FOURIER TRANSFORMS

Representing a Function by a Fourier Series

Consider a completely arbitrary function $f(\theta)$, defined in the interval $\theta = -\pi$ to $\theta = \pi$. It is possible to represent this function as an expansion in a series of functions with known properties. Only certain sets of functions are suitable for such an expansion and, in the interval $-\pi$ to π , sines and cosines together constitute such a set:

$$f(\theta) = \sum_{n=0}^{\infty} a_n \cos(n\theta) + a'_n \sin(n\theta)$$

where the index n runs through all positive integers. This expansion is called a Fourier series. The coefficients a_n and a'_n are numbers determined by the properties of $f(\theta)$.

As shown in Box 13-1, sines and cosines can be expressed in terms of complex exponentials. Therefore, the Fourier series just given can instead be written as

$$f(\theta) = \sum_{n=-\infty}^{\infty} b_n e^{in\theta}$$

where the index n now runs through both positive and negative values because these are necessary to describe sines and cosines. The coefficients b_n can be found in a simple way by making use of the following result.

For any two integers n and m ,

$$\begin{aligned} \int_{-\pi}^{\pi} e^{in\theta} e^{-im\theta} d\theta &= \int_{-\pi}^{\pi} e^{i(n-m)\theta} d\theta = [1/i(n-m)](e^{i(n-m)\pi} - e^{-i(n-m)\pi}) \\ &= [2/(n-m)] \sin(n-m)\pi = 0 \quad \text{if } n \neq m \\ &= 2\pi \quad \text{if } n = m \end{aligned}$$

where the result for $n = m$ can be proven by expanding the sine expression in a power series. Therefore, to find a particular b_m , one performs the integral

$$(1/2\pi) \int_{-\pi}^{\pi} f(\theta) e^{-im\theta} d\theta = (1/2\pi) \int_{-\pi}^{\pi} d\theta \sum_{n=-\infty}^{\infty} b_n e^{in\theta} e^{-im\theta} = b_m$$

Note that the integral is carried out over the entire range of θ over which $f(\theta)$ is defined. It often is convenient to be able to work with an arbitrary range $-L/2$ to $L/2$ rather than with $-\pi$ to π . This is accomplished by defining a new variable, $x = L\theta/2\pi$, such that when $\theta = \pi$, then $x = L/2$, and when $\theta = -\pi$, then $x = -L/2$. Incorporating this variable into the above equations, and using the fact that $dx = (L/2\pi)d\theta$, we obtain

$$f(x) = \sum_{n=-\infty}^{\infty} b_n e^{2\pi i n x / L}$$

$$b_n = (1/L) \int_{-L/2}^{L/2} e^{-2\pi i n x / L} f(x) dx$$

Fourier Transforms in One Dimension

The function $f(x)$ is defined at all x , whereas the set of coefficients b_n represents an infinite array of numbers, which must be tabulated. Therefore, it is convenient to find an analog of

the Fourier series in which the coefficients b_n are replaced by a function, and the summation is replaced by an integral. This representation is called a Fourier transform when the interval over which the function is defined extends from $-\infty$ to $+\infty$.

We define a new continuous variable, $S = 2\pi n/L$, and a new continuous function $g(S) = Lb_n$. Using these, the equation for b_n is transformed to

$$g(S) = \int_{-\infty}^{\infty} e^{-2\pi i S x} f(x) dx \quad (\text{A})$$

in the limit as $L \rightarrow \infty$. The series expansion for $f(x)$ becomes

$$f(x) = \sum_{n=-\infty}^{\infty} [g(S)/L] e^{2\pi i S x}$$

To replace the sum by an integral, note that the interval ΔS corresponds to $(2\pi/L)\Delta n$ from the definition of S . But $\Delta n = 1$ in the summation, and therefore each increment dS in an integral is equivalent to $2\pi/L$ in the sum. Thus,

$$f(x) = (L/2\pi) \int_{-\infty}^{\infty} [g(S)/L] e^{2\pi i S x} dS = (1/2\pi) \int_{-\infty}^{\infty} g(S) e^{2\pi i S x} dS \quad (\text{B})$$

Equations A and B constitute a pair of Fourier transforms that allow $f(x)$ to be calculated if $g(S)$ is known, and vice versa. They are particularly interesting because the variables x and S have opposite dimensions. For example, if x is distance, then S is reciprocal distance. The factor of $(1/2\pi)$ in equation B often is written instead as $(1/\sqrt{2\pi})$ in front of the integrals in both equations A and B.

Fourier Transforms in Three Dimensions

Suppose the function f is now defined in a Cartesian coordinate system with axes x, y, z . For fixed y and z , the function $f(x, y, z)$ can be expanded in a Fourier series in $e^{2\pi i S_x x}$, and the Fourier transform becomes (by analogy to Equation A)

$$g_{yz}(S_x) = \int_{-\infty}^{\infty} e^{-2\pi i S_x x} f(x, y, z) dx$$

This expression, in turn, can be expanded in the function $e^{2\pi i S_y y}$ for fixed z , and finally as a function of $e^{2\pi i S_z z}$. The resulting three-dimensional Fourier transform is

$$g(S_x, S_y, S_z) = \int_{-\infty}^{\infty} dz e^{-2\pi i S_z z} \int_{-\infty}^{\infty} dy e^{-2\pi i S_y y} \int_{-\infty}^{\infty} dx e^{-2\pi i S_x x} f(x, y, z)$$

If we use the vector S to represent the three variables S_x, S_y , and S_z , and we use r to represent x, y , and z , then the three-dimensional transform can be written very compactly as

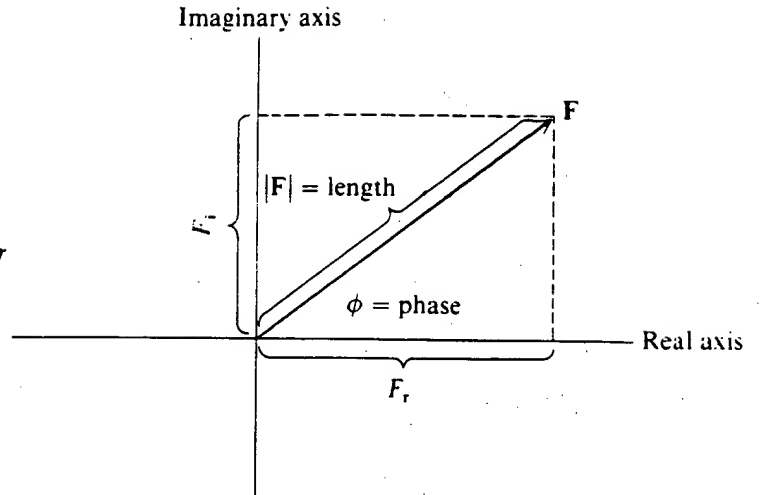
$$g(S) = \int_{-\infty}^{\infty} d\mathbf{r} e^{-2\pi i \mathbf{S} \cdot \mathbf{r}} f(\mathbf{r})$$

Similarly, the analog of Equation B becomes

$$f(\mathbf{r}) = (1/2\pi)^3 \int_{-\infty}^{\infty} d\mathbf{S} e^{2\pi i \mathbf{S} \cdot \mathbf{r}} g(\mathbf{S})$$

Figure 13-4

The structure factor plotted as a vector in the complex plane.



Box 13-3 THE DIRAC DELTA FUNCTION

We wish to demonstrate that the following integral is a representation of the one-dimensional Dirac delta function:

$$\delta(x - x') = \int_{-\infty}^{\infty} e^{2\pi i(x - x')S} dS$$

The results can easily be generalized to three dimensions. If this is the delta function, it must obey three properties.

First, if $x' = x$, then $\delta(x - x') = \infty$. It is obvious that, with $x = x'$, the exponential in the above integral is just unity; therefore, the integral is infinite.

Second, if $x' \neq x$, then $\delta(x - x') = 0$. It is not so obvious that the integral meets this requirement. The way to realize that it does is to note that the complex exponential is a periodic function that continually oscillates from -1 to 1 throughout all space. For each positive lobe there exists an adjacent (absolutely equivalent) negative lobe. The areas underneath these lobes cancel identically.

Third, if x' lies between a and b , then

$$\int_b^a dx \delta(x - x') = 1$$

Let $a = x' + \epsilon$, and $b = x' - \epsilon$. Then the area under the delta function is

$$\begin{aligned} \int_{x' - \epsilon}^{x' + \epsilon} dx \int_{-\infty}^{\infty} e^{2\pi i(x - x')S} dS &= \int_{-\infty}^{\infty} dS \int_{x' - \epsilon}^{x' + \epsilon} dx e^{2\pi i(x - x')S} \\ &= \int_{-\infty}^{\infty} e^{-2\pi i x' S} dS \int_{x' - \epsilon}^{x' + \epsilon} e^{2\pi i x S} dx \\ &= \int_{-\infty}^{\infty} e^{-2\pi i x' S} \left[\frac{1}{2\pi i S} (e^{2\pi i(x' + \epsilon)S} - e^{2\pi i(x' - \epsilon)S}) \right] dS \end{aligned}$$

Experimentally, all one can observe is the intensity of radiation scattered at an angle 2θ . If we express this intensity relative to the intensity scattered by a single electron at the origin, it is

$$I(S) = F(S)F^*(S) = |F|^2 \quad (13-16)$$

We must multiply by the complex conjugate, rather than simply by $F(S)$, because F is a complex number. The intensity is a pure observable and must be real. It is given by the square of the amplitude of the structure factor. Thus $|F|$ can be measured experimentally. The phase term ($e^{i\phi}$) of $F(S)$ is not directly measurable; this is the major obstacle in x-ray scattering and diffraction studies. In order to use Equation 13-8 to calculate $\rho(\mathbf{r})$, one first must guess, calculate, or indirectly estimate $e^{i\phi}$.

$$\begin{aligned} &= \int_{-\infty}^{\infty} e^{-2\pi i x' S} [(e^{2\pi i x' S} / 2\pi i S) 2i \sin 2\pi \epsilon S] dS \\ &= (1/\pi) \int_{-\infty}^{\infty} [(\sin 2\pi \epsilon S) / S] dS = 1 \end{aligned}$$

because

$$\int_0^{\infty} [(\sin x)/x] dx = \int_{-\infty}^0 [(\sin x)/x] dx = \pi/2$$

If x' is not between a and b , then the integral $\int_a^b dx \delta(x - x')$ is zero, because the function is everywhere zero. Thus we see that the integral originally given meets all the requirements, and is in fact the Dirac delta function.

A most important property of the delta function is the ability to shift the location of another function:

$$\int_{-\infty}^{\infty} dx f(x) \delta(x - x') = f(x')$$

We can demonstrate this by choosing a narrow interval $x' - \epsilon$ to $x' + \epsilon$ near x' and breaking up the integral into three parts:

$$\int_{-\infty}^{x' - \epsilon} dx f(x) \delta(x - x') + \int_{x' - \epsilon}^{x' + \epsilon} dx f(x) \delta(x - x') + \int_{x' + \epsilon}^{\infty} dx f(x) \delta(x - x')$$

The first and third integrals are zero for any finite-valued function $f(x)$, because everywhere within them $\delta(x - x') = 0$. The second integral can be evaluated if we choose ϵ small enough so that $f(x) = f(x')$; then it becomes

$$f(x') \int_{x' - \epsilon}^{x' + \epsilon} dx \delta(x - x') = f(x')$$

The electron density in Equations 13-7 and 13-8 is, in principle, measurable directly, and therefore it must be real. As probed by x-ray scattering experiments, $\rho(\mathbf{r})$ behaves as a real quantity so long as there is no anomalous scattering (vide infra). The reality of $\rho(\mathbf{r})$ allows a constraint on $F(\mathbf{S})$ to be developed. Because $\rho(\mathbf{r})$ is real, $\rho(\mathbf{r}) = \rho^*(\mathbf{r})$. Substituting Equation 13-13 into Equation 13-8, and taking the complex conjugate, we obtain

$$\int [F_r(\mathbf{S}) + iF_i(\mathbf{S})]e^{-2\pi i\mathbf{S} \cdot \mathbf{r}} d\mathbf{S} = \int [F_r(\mathbf{S}) - iF_i(\mathbf{S})]e^{+2\pi i\mathbf{S} \cdot \mathbf{r}} d\mathbf{S} \quad (13-17a)$$

Note that \mathbf{r} can take on any value. For Equation 13-17a to hold for any arbitrary value of \mathbf{r} , it is necessary (for every value of \mathbf{S}) that

$$F_r(\mathbf{S}) = F_r(-\mathbf{S}) \quad \text{and} \quad F_i(\mathbf{S}) = -F_i(-\mathbf{S}) \quad (13-17b)$$

In other words, the real part of the scattering function must be symmetrical about the origin of \mathbf{S} space, whereas the imaginary part is antisymmetric. When such a relationship holds, the function $F(\mathbf{S})$ is called a conjugate function.

When the results of Equation 13-17b are substituted into the definition of the intensity, an interesting result emerges:

$$I(\mathbf{S}) = |F(\mathbf{S})|^2 = F_r^2 + F_i^2 = |F(-\mathbf{S})|^2 = I(-\mathbf{S}) \quad (13-18)$$

Equation 13-18 reveals that the observed pattern of scattered intensity is symmetric about the origin of reciprocal space at $\mathbf{S} = 0$. The result, that $I(\mathbf{S})$ has a center of symmetry, is called Friedel's law. It means that one has to measure only half the scattering to obtain all the information it contains.

A requirement for heterogeneities in electron density

Suppose that an experimental sample consists of a uniform distribution of electron density, $\rho(\mathbf{r}) = \rho$. Then the expected structure factor is

$$F(\mathbf{S}) = \rho \int d\mathbf{r} e^{2\pi i\mathbf{S} \cdot \mathbf{r}} \quad (13-19)$$

But this is just the Dirac delta function $\delta(\mathbf{S} - 0)$. The only x rays that emerge from the sample are $F(0)$. From Figure 13-3, $\mathbf{S} = 0$ corresponds to scattered radiation parallel to the incident beam. In other words, a uniform sample cannot deflect x rays at all, just as a medium of constant refractive index cannot bend or focus collimated light.

A fundamental principle of scattering is the requirement for spatial (or temporal) heterogeneities. Scattering is caused by the contrast between a given region and its neighbors. We now must calculate the scattering that results from the presence of

discrete atoms, and then that resulting from arrangements of atoms found in molecules or crystal lattices.

Scattering from a single atom at the origin

Suppose the sample consists solely of a single atom located at the origin. The detailed pattern of electron density around an individual atom depends on the bonding it is involved in. However, in almost all x-ray diffraction experiments, the resolution is not high enough to detect this detailed pattern. Thus, it is a good approximation to model the electron distribution of an atom as spherically symmetric. Then $\rho(\mathbf{r})$ becomes $\rho(r)$. If we express Equation 13-7 in spherical polar coordinates (Fig. 13-5a),

$$\begin{aligned} F(\mathbf{S}) &= \int_0^{2\pi} d\phi \int_0^\pi \sin \theta d\theta \int_0^\infty dr \rho(r) r^2 e^{2\pi i \mathbf{S} \cdot \mathbf{r}} \\ &= 2\pi \int_0^\pi dr \rho(r) r^2 \int_0^\pi d\theta \sin \theta e^{2\pi i S r \cos \theta} \end{aligned} \quad (13-20)$$

where S and r are the lengths of the vectors \mathbf{S} and \mathbf{r} , respectively. By making the substitution $x = \cos \theta$, we can easily evaluate the θ integral, obtaining

$$F(\mathbf{S}) = 4\pi \int_0^\infty dr \rho(r) r^2 \left[\frac{\sin 2\pi S r}{2\pi S r} \right] \equiv f(S) \quad (13-21)$$

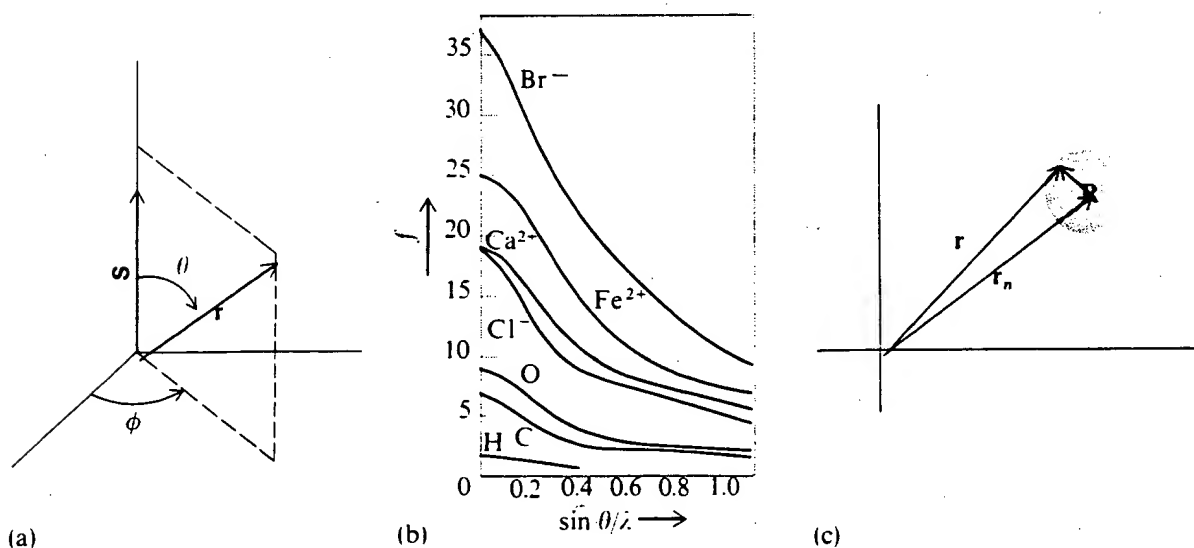


Figure 13-5

X-ray scattering from atoms. (a) Coordinate system used to evaluate Equation 13-20. (b) Atomic scattering factor for various atoms as a function of the scattering angle (2θ). [After J. P. Glusker and K. N. Trueblood, *Crystal Structure Analysis: A Primer* (London: Oxford Univ. Press, 1972).] (c) Coordinate system used to describe an atom not at the origin.

The function $f(S)$ is defined as the atomic scattering factor. It depends only on $|S|$ and thus, from Equation 13-5, it depends only on the angle between \hat{s}_0 and \hat{s} , and not on the orientation of the sample. Note that, because $\rho(r) = \rho(-r)$, the function $f(S)$ is real. Therefore, the intensity measured in a scattering experiment on a single atom, $I(S)$, can be used to compute $f(S)$ directly by Equation 13-16:

$$f(S) = \pm [I(S)]^{1/2} \quad (13-22)$$

The only ambiguity is the choice of sign; we can arbitrarily define this sign to be positive.

For real atoms, $\rho(r)$ can be crudely approximated by a Gaussian distribution of electron density: $\rho(r) = zNe^{-kr^2}$, where z is the number of electrons, N is a normalization constant, and k is related to the width of the Gaussian. Then Equation 13-21 can be integrated to yield.

$$f(S) = ze^{-(\pi^2/k)S^2} \quad (13-23)$$

This relationship shows that the atomic scattering factor has the same sign everywhere in space. The atomic scattering factor for forward-scattered radiation ($S = 0$) is simply the number of electrons. Equation 13-23 shows that spherical atoms scatter x rays most efficiently in the forward directions. The scattering factor drops fairly rapidly with increasing scattering angle (Fig. 13-5b).

Scattering from atoms not located at the origin

Next, suppose the sample is still a single spherical atom, but it now is centered at the position \mathbf{r}_n . As before, \mathbf{r} is a vector from the coordinate system origin to a point within the electron density distribution of the atom. \mathbf{R} is a vector from the atom center to the point \mathbf{r} . It is defined by $\mathbf{r} = \mathbf{R} + \mathbf{r}_n$ (Fig. 13-5c). Thus, from Equation 13-7, the x-ray scattering is

$$F(S) = \int d(\mathbf{R} + \mathbf{r}_n) \rho(\mathbf{R} + \mathbf{r}_n) e^{2\pi i \mathbf{S} \cdot (\mathbf{R} + \mathbf{r}_n)} \quad (13-24)$$

Because \mathbf{r}_n is constant, $d(\mathbf{R} + \mathbf{r}_n) = d\mathbf{R}$, and the term $e^{2\pi i \mathbf{r}_n \cdot \mathbf{S}}$ can be removed from the integral:

$$F(S) = e^{2\pi i \mathbf{S} \cdot \mathbf{r}_n} \int d\mathbf{R} \rho(\mathbf{R} + \mathbf{r}_n) e^{2\pi i \mathbf{S} \cdot \mathbf{R}} \quad (13-25)$$

The integral in Equation 13-25 is taken over all space. Because ρ is the electron density distribution around the atom, the constant vector \mathbf{r}_n specifying the original

coordinate system is irrelevant. Thus, this integral is identical to Equation 13-20. It is just the atomic scattering factor, and so Equation 13-25 becomes

$$F(\mathbf{S}) = f(\mathbf{S})e^{2\pi i \mathbf{S} \cdot \mathbf{r}_n} \quad (13-26)$$

For a set of N atoms, each located at position \mathbf{r}_n with atomic scattering factor f_n , the total structure factor expected is

$$F(\mathbf{S}) = \sum_{n=1}^N f_n(\mathbf{S})e^{2\pi i \mathbf{S} \cdot \mathbf{r}_n} \quad (13-27)$$

where f_n is the scattering factor of the n th atom. If the N atoms happen to belong to a single molecule, then Equation 13-27 is called the molecular structure factor, $F_m(\mathbf{S})$.

Consider the case of a sample with a center of symmetry. If that center is placed at the origin, then for each atom at \mathbf{r}_n contributing $f_n(\mathbf{S})e^{2\pi i \mathbf{S} \cdot \mathbf{r}_n}$ in Equation 13-27, there must be an equivalent atom at $-\mathbf{r}_n$ contributing $f_n(\mathbf{S})e^{-2\pi i \mathbf{S} \cdot \mathbf{r}_n}$. Because $e^{\pm ix} = \cos x \pm i \sin x$ (Box 13-1), the structure factor of the sample can be written as the centrosymmetric function:

$$F_{cs}(\mathbf{S}) = \sum_{n=1}^{N/2} 2f_n(\mathbf{S}) \cos(2\pi \mathbf{S} \cdot \mathbf{r}_n) \quad (13-28)$$

which is a sum over $N/2$ symmetry-related pairs of atoms. This is a real function, and therefore the problem of determining the phase of $F_{cs}(\mathbf{S})$ is dramatically simplified. From Figure 13-4, note that ϕ must be either 0 or π . Thus the term $e^{i\phi}$ must be simply +1 or -1 at each point \mathbf{S} , corresponding respectively to $\phi = 0$ or $\phi = \pi$.

13-2 X-RAY DIFFRACTION

Interference fringes from sets of atoms

In general, moving an atom to position \mathbf{r}_n (away from the origin) introduces a phase shift, $e^{2\pi i \mathbf{S} \cdot \mathbf{r}_n}$, in the x-ray scattering. Note that, for a single atom, this will lead to no observable change in scattering because the intensity is still $I(\mathbf{S}) = f^2(\mathbf{S})$. Suppose, however, a sample contains one atom at the origin and an identical atom at position \mathbf{r}_n . The total structure factor will be

$$F(\mathbf{S}) = f(\mathbf{S})(1 + e^{2\pi i \mathbf{S} \cdot \mathbf{r}_n}) \quad (13-29a)$$

The scattering intensity will be

$$I(S) = f^2(S)(1 + e^{2\pi i S \cdot r_n})(1 + e^{-2\pi i S \cdot r_n}) = 2f^2(S)[1 + \cos(2\pi S \cdot r_n)] \quad (13-29b)$$

Thus—in addition to the scattering seen from each of the atoms separately, $f^2(S)$ —there is an interference pattern generated by the $\cos 2\pi S \cdot r_n$ term (see Fig. 13-6b). This is exactly comparable to the interference fringes seen in a two-slit experiment in optical diffraction (see Box 13-4). The term $e^{2\pi i S \cdot r_n}$ in Equation 13-29 often is called a fringe function.

If it were possible to measure the scattering from a sample containing just a few atoms, the pattern of fringes would yield information on the spatial arrangement. Such measurements are impossible because the intensity of radiation scattered from just a few atoms is too small. The number of terms in the structure factor increases as the total number of atoms (N_T) increases, and therefore the observed intensities increase as N_T^2 . To increase the number of atoms without loss of information, it is necessary to work with periodic arrays of atoms, such as atoms in crystals. Here we shall demonstrate the pattern of fringes introduced by such arrays.

Calculation of x-ray diffraction from a one-dimensional array

Start with a one-dimensional row of $2N + 1$ identical atoms. Locate the central atom at the origin of the coordinate system. As shown in Figure 13-6a, the position of each atom in the array is generated from that of its neighbor by translation along a vector \mathbf{a} . The position of the n th atom in the array is $n\mathbf{a}$. The structure factor resulting from this atom is given by Equation 13-26:

$$F_n(S) = e^{2\pi i n S \cdot \mathbf{a}} f(S) \quad (13-30)$$

Thus the scattering from any of the atoms can be written in terms of the atomic scattering factor $f(S)$ for an atom at the origin. The structure factor for the whole array can be written as

$$F_{\text{Tot}}(S) = f(S) \sum_{n=-N}^N e^{2\pi i n S \cdot \mathbf{a}} \quad (13-31)$$

The sum is the fringe function resulting from the array.

We could treat a linear array of molecules in a similar way. If this array is generated by translation, the resulting scattering will be given by an equation identical to Equation 13-31, except that the molecular structure factor $F_m(S)$ will replace the atomic scattering factor $f(S)$. However, with molecules, more complex arrays

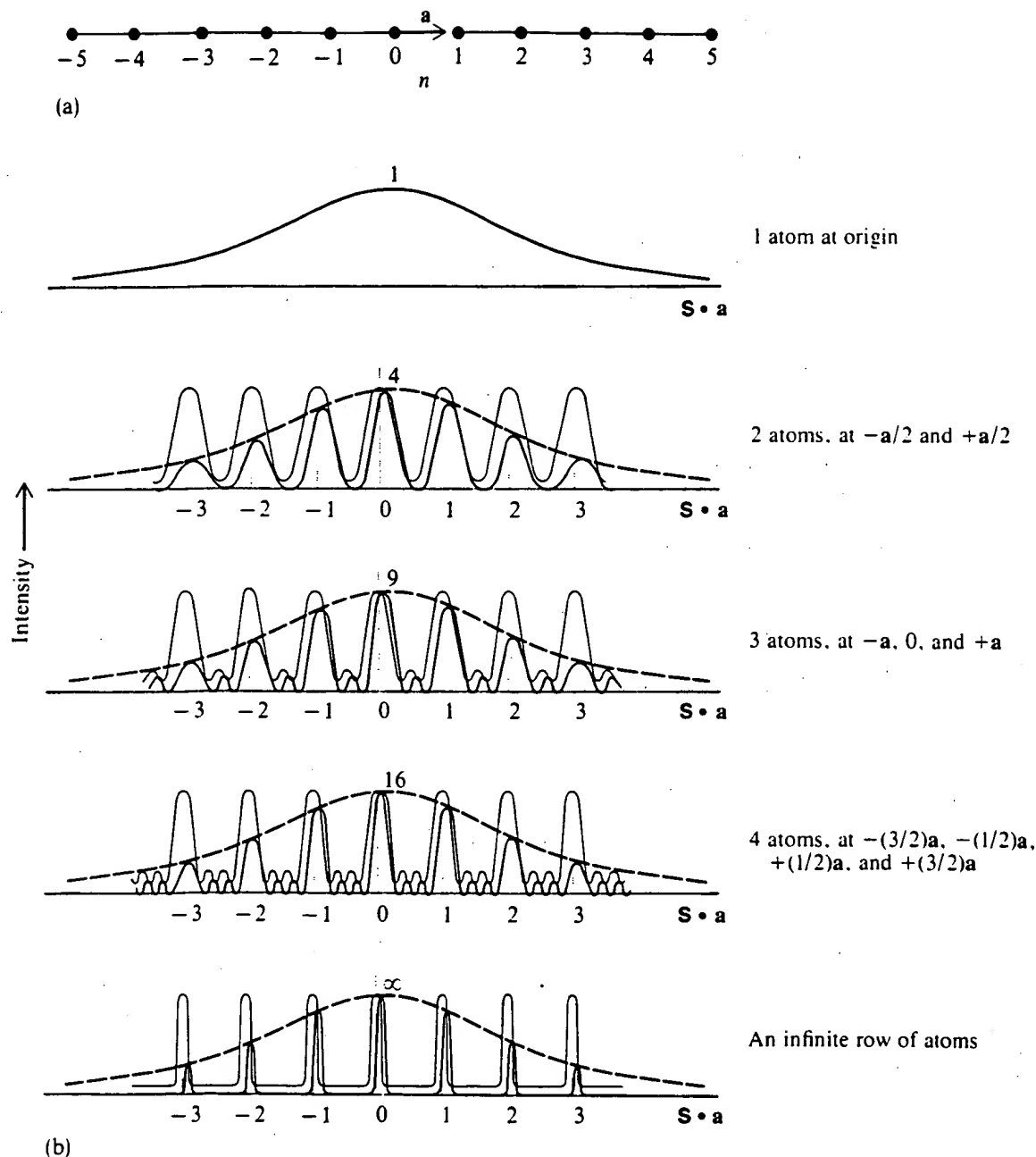


Figure 13-6

X-ray scattering from a one-dimensional array of atoms. (a) The array, as defined by the vector translation a . (b) X-ray scattering intensity as a function of the number of atoms in the array. Shown are the actual observed scattering (black line), the scattering expected for a single atom (dashed line), and the fringe function produced by the array (colored line). The observed scattering is the product of the fringe function and the single-atom scattering. Note the changes in vertical scale as the number of atoms increases. The horizontal scale is in units of $S \cdot a$ and is the same for all cases.

can be generated if there are rotations as well as translations relating adjacent molecules. These cases can be handled by simple extension of the methods used here; some examples are given in Chapter 14, where we discuss scattering from helices.

Equation 13-31 is simply a geometric series with an initial term $e^{-2\pi i N S \cdot a}$, a constant ratio $e^{2\pi i S \cdot a}$, and a final term $e^{2\pi i S \cdot a}$. The sum of a geometric series is $t(1 - r^m)/(1 - r)$, where r is the ratio between terms, m is the number of terms, and t is the first term. Using this expression, Equation 13-31 becomes

$$F_{\text{Tot}}(S) = f(S) \frac{e^{-2\pi i N S \cdot a} (1 - e^{2\pi i (2N+1) S \cdot a})}{1 - e^{2\pi i S \cdot a}} \quad (13-32)$$

Equation 13-32 can be simplified by multiplying both numerator and denominator by $e^{-\pi i S \cdot a}$. Then

$$\begin{aligned} F_{\text{Tot}}(S) &= f(S) \frac{e^{-\pi i (2N+1) S \cdot a} - e^{\pi i (2N+1) S \cdot a}}{e^{-\pi i S \cdot a} - e^{\pi i S \cdot a}} \\ &= f(S) \frac{\sin[(2N+1)\pi S \cdot a]}{\sin(\pi S \cdot a)} \end{aligned} \quad (13-33)$$

We have used the fact that $e^{\pm ix} = \cos x \pm i \sin x$ to reach the final form of Equation 13-33.

The intensity of scattering from the array will be

$$I_{\text{Tot}}(S) = |F_{\text{Tot}}(S)|^2 = [f(S)]^2 \left(\frac{\sin[(2N+1)\pi S \cdot a]}{\sin(\pi S \cdot a)} \right)^2 \quad (13-34)$$

This is shown schematically as a function of the size of the array in Figure 13-6b. You can see that, as N becomes large, the intensity tends to zero everywhere except where $S \cdot a$ is integral. The term $S \cdot a$ that appears in Equation 13-34 measures the relative orientation of the sample and the detector. Note that the scattering intensity is a maximum when $S \cdot a = 0$. This occurs when S is in a plane perpendicular to the long axis of the array.

Discontinuous diffraction pattern from a one-dimensional array

It is helpful to demonstrate explicitly the behavior of Equation 13-33 as N becomes large. For most values of $S \cdot a$, the value of $\sin(\pi S \cdot a)$ lies between 0.1 and 1.0 or between -0.1 and -1.0 . Around these values of $S \cdot a$, the value of $\sin[(2N+1)\pi S \cdot a]$ oscillates wildly between 0 and 1. Therefore, the quotient in Equation 13-33 falls in the range of about -10 to 10 , regardless of the value of N . However, what happens when $\sin(\pi S \cdot a)$ approaches zero? It is easiest to examine this behavior in the limit where $S \cdot a \rightarrow 0$. If we use the series expansion for $\sin x = x - x^3/3! + \dots$, and if

we keep only the first term as $x \rightarrow 0$, the quotient in Equation 13-33 becomes $(2N + 1)(\pi \mathbf{S} \cdot \mathbf{a}) / (\pi \mathbf{S} \cdot \mathbf{a}) = 2N + 1$.

In a crystalline array of molecules, N can be 10^6 or more. Therefore, the structure factor becomes enormous each time $\sin(\pi \mathbf{S} \cdot \mathbf{a})$ goes to zero. This occurs every time $\mathbf{S} \cdot \mathbf{a}$ approaches an integer. Compared with the sharp peak in scattering for integral $\mathbf{S} \cdot \mathbf{a}$, all other values are negligible. Therefore, the fringe function of a linear array leads to a discontinuous scattering pattern (Box 13-4 illustrates the analogous effect in optical diffraction). Only for certain orientations of sample and x-ray detector will any scattering be observed at all. This result is called a von Laue condition:

$$\mathbf{S} \cdot \mathbf{a} = h, \quad \text{where } h = 0, \pm 1, \pm 2, \dots \quad (13-35)$$

The vector \mathbf{a} is a property of the particular one-dimensional crystalline sample and its orientation in space. The vector \mathbf{S} depends on the geometry of the scattering experiment. The observed scattering depends only on $\mathbf{S} \cdot \mathbf{a}$ and is intense only when Equation 13-35 is satisfied. Figure 13-7 shows the geometrical significance of this. $\mathbf{S} \cdot \mathbf{a}$ is the projection of \mathbf{S} onto \mathbf{a} . Suppose \mathbf{a} is fixed. Then $\mathbf{S} \cdot \mathbf{a} = 0$ means that \mathbf{S} can be any vector in a plane perpendicular to \mathbf{a} and passing through the origin (Fig. 13-7a). $\mathbf{S} \cdot \mathbf{a} = 1$ means that \mathbf{S} can be any vector from the origin to a plane perpendicular to \mathbf{a} and spaced a distance $1/a$ away from the origin (Fig. 13-7b). For example, if \mathbf{S} is parallel to \mathbf{a} , then $\mathbf{S} \cdot \mathbf{a} = 1$ implies that $|\mathbf{S}| = 1/|\mathbf{a}|$.

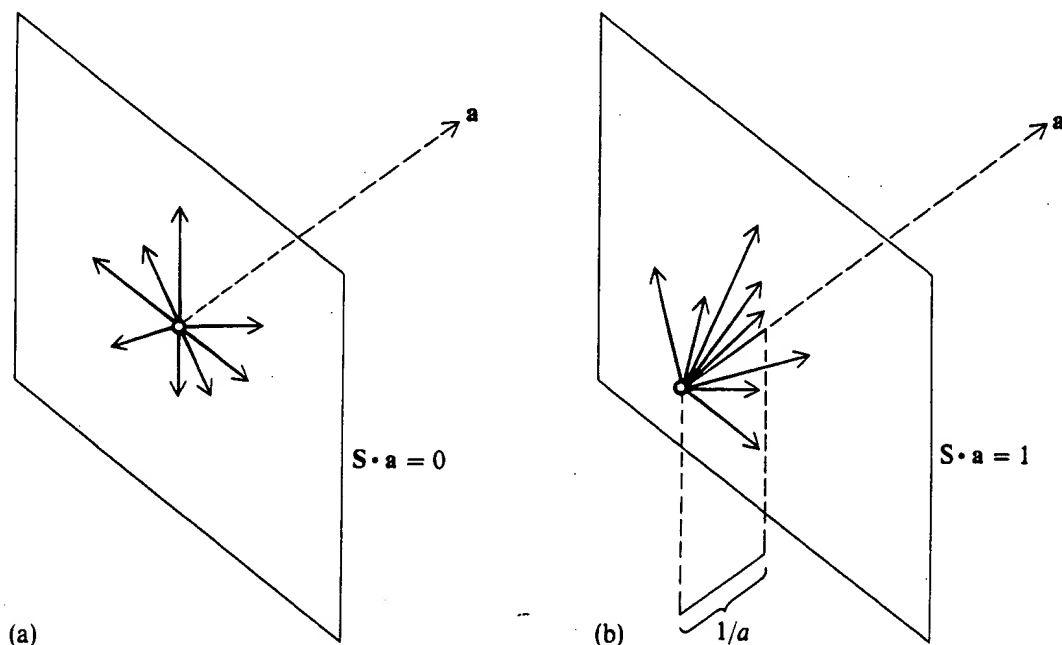
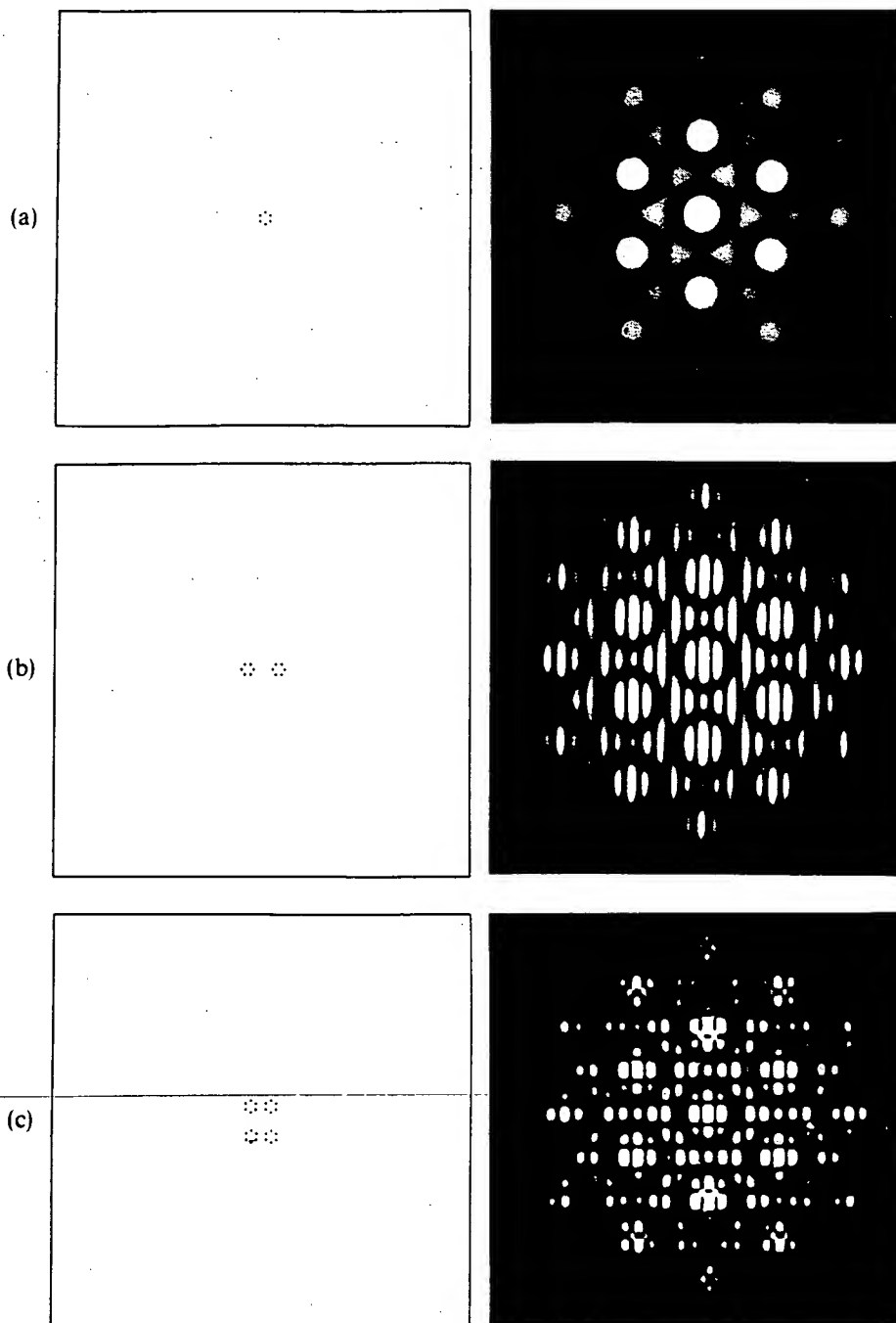


Figure 13-7

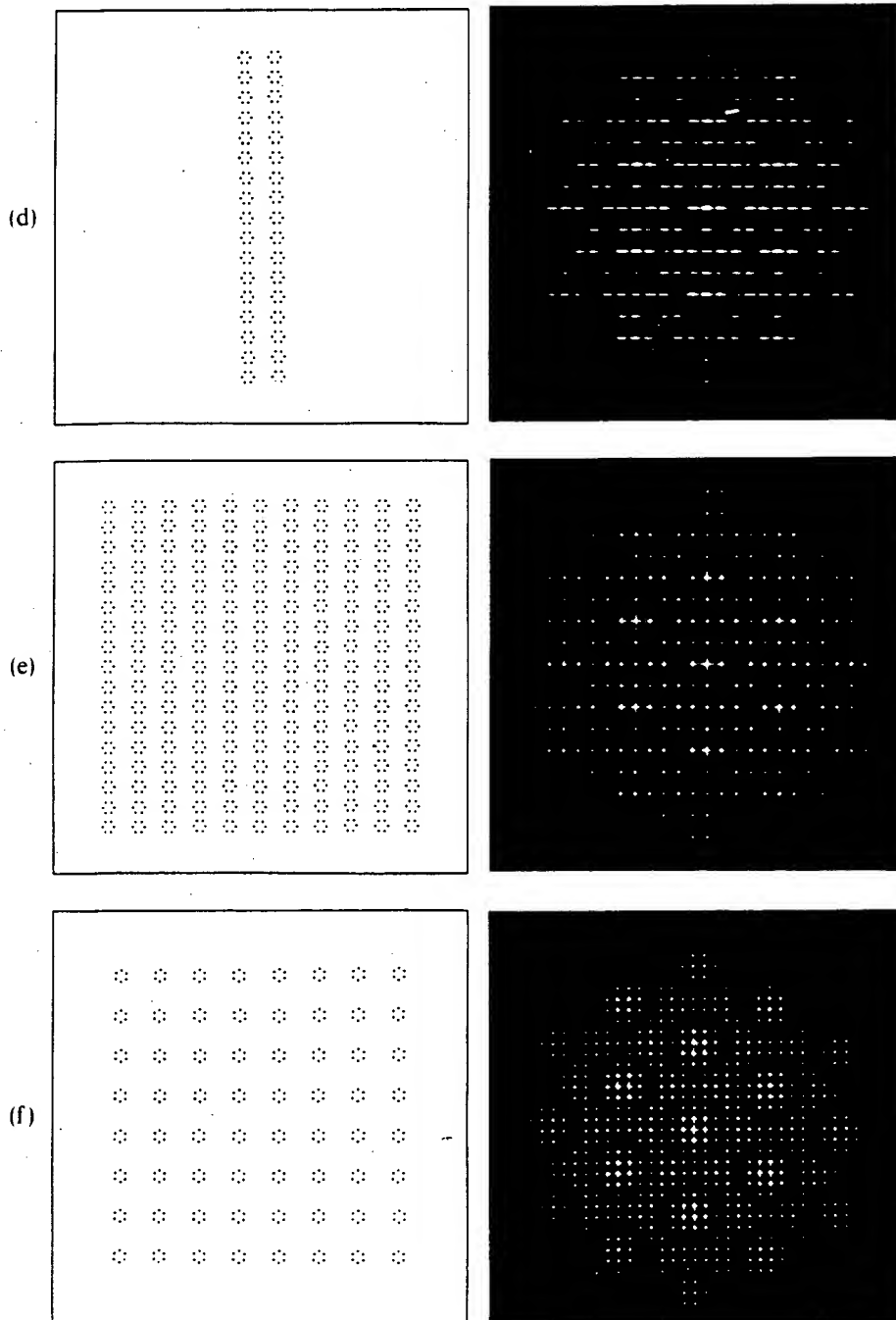
The von Laue scattering conditions for a one-dimensional array. Scattering vectors are shown as solid arrows. (a) For $\mathbf{S} \cdot \mathbf{a} = 0$. (b) For $\mathbf{S} \cdot \mathbf{a} = 1$.

Box 13-4 OPTICAL DIFFRACTION PATTERNS FROM ARRAYS

The same mathematical formalism developed in the text to calculate x-ray diffraction from molecular arrays also applies to optical diffraction from arrays of slits or pinholes. The figures show the optical diffraction pattern from a series of opaque masks containing increasingly more elaborate arrays of pinholes. Such diffraction patterns can be created by the apparatus shown in Figure 10-4a by using the mask as a sample. The figures on the left show the sample masks used; the corresponding figures on the right indicate the diffraction patterns produced by the masks.



(a) A six-atom molecule, modeled by six pinholes. (b) Two six-atom molecules in a row. Note how the presence of two atoms introduces additional vertical fringes. (c) Four six-atom molecules. The horizontal repeat in structure leads to additional horizontal fringes. (d) A vertical row of many pairs of six-atom molecules. Note how the diffraction pattern sharpens in the vertical direction but remains broad in the horizontal direction. (e) A two-dimensional crystalline array of six-atom molecules. Note that the diffraction pattern is now a set of sharp spots. (f) A different crystalline array of the same molecules. The smaller reciprocal lattice results from the larger crystal lattice. [From G. Harburn, C. A. Taylor, and T. R. Welberry, *Atlas of Optical Transforms* (Ithaca, N.Y.: Cornell Univ. Press, 1975).]



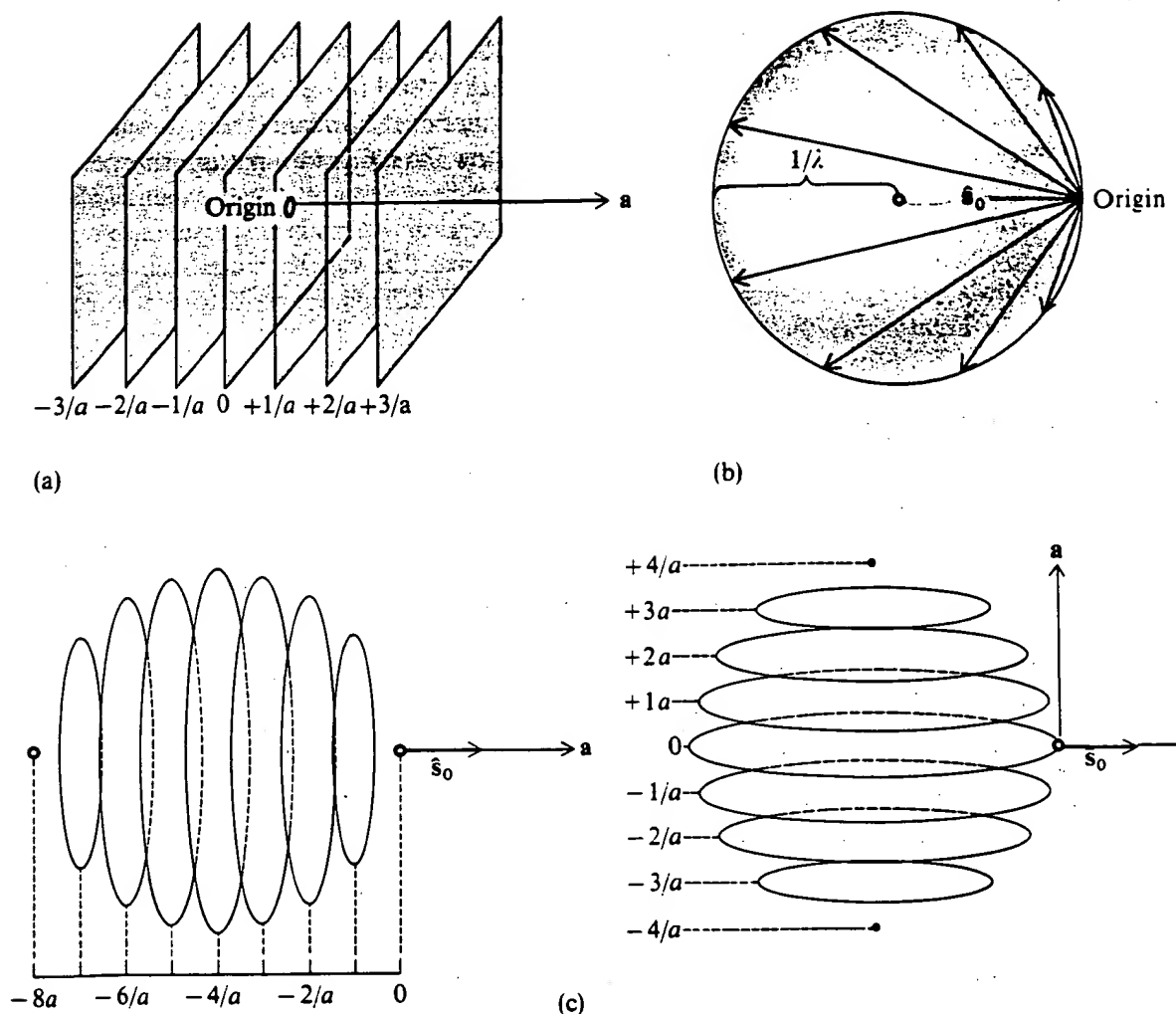


Figure 13-8

Experimental conditions for observation of scattering from the linear array of atoms shown in Figure 13-6.

(a) A set of parallel planes, representing the von Laue condition imposed by the array of atoms.

(b) For a fixed direction \hat{s}_0 of incident x rays, the possible scattering vectors (*black*) must lie on the surface of the sphere. (See Fig. 13-3a for further information.)

(c) The intersection of the two sets of conditions outlined in parts a and b is shown for two different relative geometries of a and \hat{s}_0 .

By extending this argument, it is clear that integral values of $S \cdot a$ define a set of parallel planes. The spacing between these planes is $1/a$ (Fig. 13-8a). The set of parallel planes in reciprocal space defines all those values of the scattering vector that produce measurable intensity. Further constraints are introduced if the wavelength of the incident x rays is held constant, and if their direction is fixed at \hat{s}_0 .

Once a particular \hat{s}_0 is selected, the various possible observation directions \hat{s} lead to a restricted set of possible scattering vectors S . Note from Figure 13-3b that the tip of the vector S always extends from the origin to a point at a distance $1/\lambda$ along \hat{s} . The locus of all points located $1/\lambda$ from \hat{s} will define a sphere of radius $1/\lambda$ centered at the tail of \hat{s} . Thus all possible scattering vectors S must extend from the origin to the surface of a sphere of radius $1/\lambda$ (Fig. 13-8b). This sphere is called the

sphere of reflection. It is always tangent to the plane drawn through the origin perpendicular to the direction of incident x rays, \hat{s}_0 .

The scattering of x rays will be observed only when both the von Laue conditions and the conditions of the sphere of reflection are satisfied. This means that the scattering vector must lie on points formed by the intersection of the surface of a sphere and a set of parallel planes. As shown in Figure 13-8c, this intersection is a set of parallel circles. The orientation of the circles, and the identity of the particular planes from which they originate, depend on the angle between \hat{s}_0 and \mathbf{a} .

Sampling the scattering from any atom or molecule in a periodic array

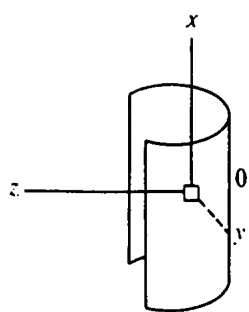
For a sample consisting of a single atom, the atomic scattering factor $f(S)$ would be measurable with a single sample orientation and \hat{s}_0 , at geometries S , anywhere on the surface of a sphere of radius $1/\lambda$. With a linear array of atoms oriented along \mathbf{a} , this atomic transform now can be measured only where this sphere is intersected by a set of parallel planes with a spacing of $1/a$ (Fig. 13-8c). One describes this by saying that the originally broad atomic or molecular structure factor now is sampled at discrete places. Figure 13-6 shows an additional example of this sampling (see also Box 13-4). The orientation and spacing of the scattering planes contain all the information about the array and no information about the atom or molecule. The actual value (amplitude and phase) of the structure factor at these sampling positions retains information about the structure of the atom or molecule.

Note that all of the conditions restricting the observation of scattering have been plotted in Figures 13-7 and 13-8 in terms of the vector S . The dimensions of S are reciprocal distance, and so the coordinate system shown in these figures is reciprocal space. Increasing the distance between atoms of an array (in real space) will result in decreasing the spacing imposed by the von Laue conditions on the parallel planes (in reciprocal space).

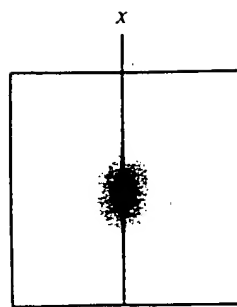
A fixed orientation of \mathbf{a} and \hat{s}_0 allows only a restricted region of reciprocal space to be sampled in an x-ray scattering experiment. This region can be enlarged by changing the angle between \mathbf{a} and \hat{s}_0 , by rotating either the sample or the angle of incidence of the x rays. The largest possible value of $|S|$ for any geometry is $2/\lambda$ (Fig. 13-3c). Therefore, the maximal region of reciprocal space that can be sampled, after all orientations of \mathbf{a} and \hat{s}_0 have been tried, is a sphere of radius $2/\lambda$ centered at the origin of reciprocal space. This sphere is called the limiting sphere (see Fig. 13-23b).

X-ray scattering actually observed in the laboratory frame

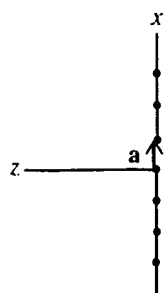
The scattering vector S is very convenient for mathematics, but it tends to obscure what is happening in an experiment. Therefore, Figure 13-9 shows the diffraction from a linear array of identical scatterers in the laboratory frame. Assume that the sample is placed at the center of a cylinder of x-ray film (Fig. 13-9a). X rays are incident along a fixed direction, and all of the scattered intensity is detected by the film. Dif-



(a)



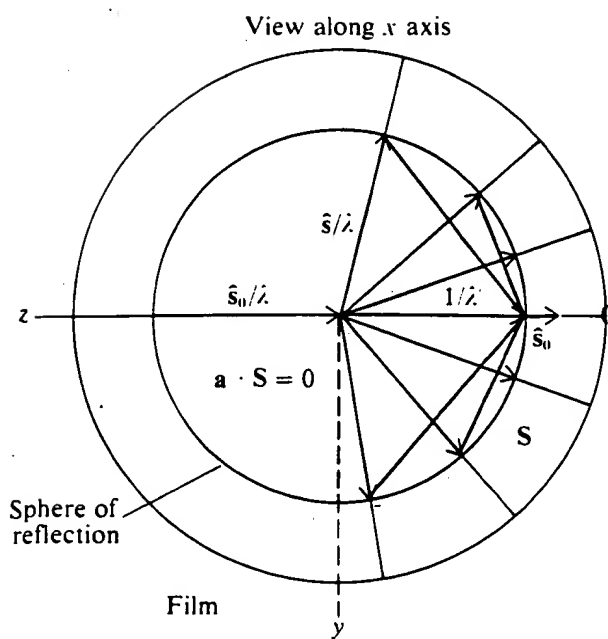
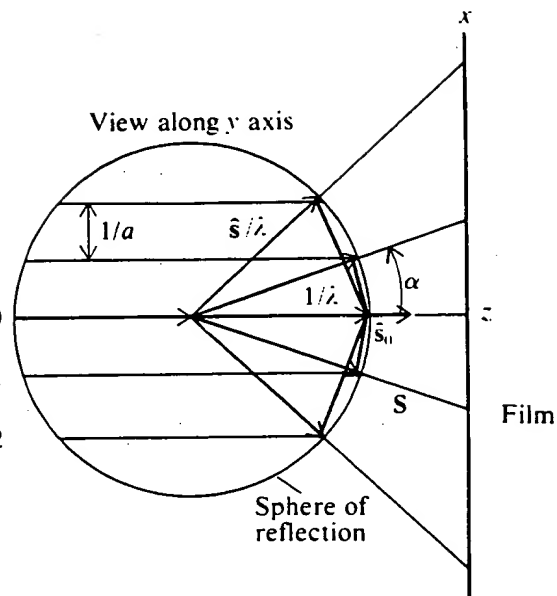
(b)



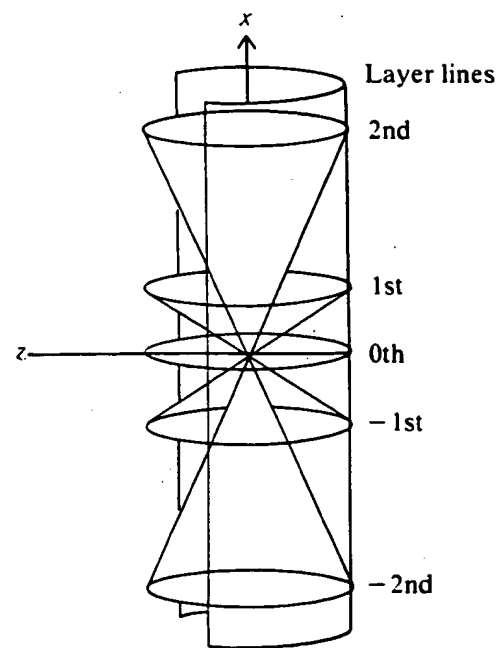
(c)

$$\begin{aligned} a \cdot S &= 2 \\ a \cdot S &= 1 \\ a \cdot S &= 0 \\ a \cdot S &= -1 \\ a \cdot S &= -2 \end{aligned}$$

(d)



(e)



(f)

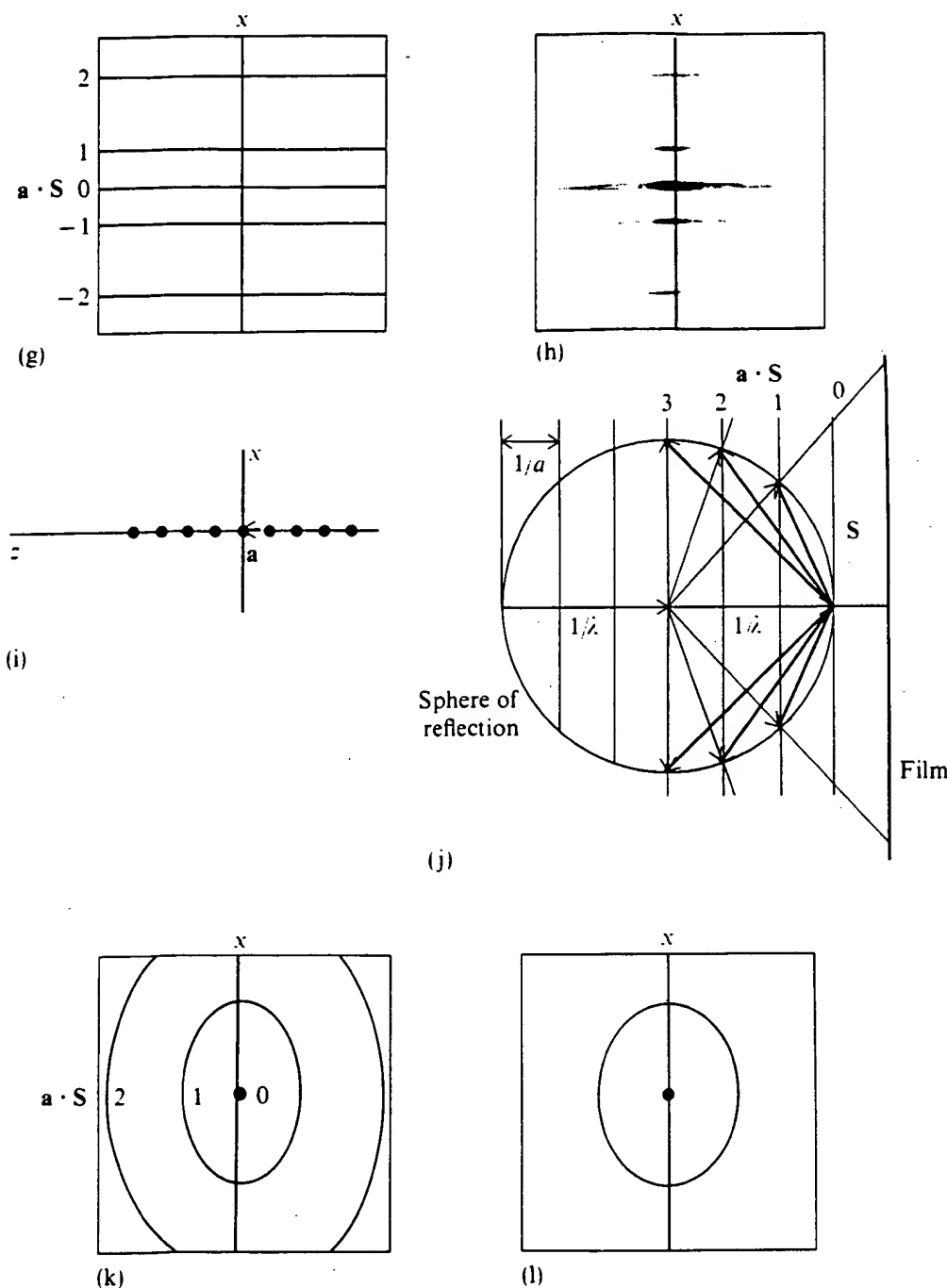


Figure 13-9

X-ray scattering from a one-dimensional array as seen in the laboratory. (a) X rays incident along the z axis strike a sample at the origin, and scattered rays are detected by a cylindrical film. (b) Scattering pattern produced by a single atom. The pattern is elliptical because of the cylindrical film; the pattern would be circular if flat film were used. (c) The linear array. (d) The scattered radiation allowed by the von Laue conditions, viewed in the x - z plane. (e) The scattered radiation allowed by the von Laue conditions, viewed in the y - z plane. (f) Cones of scattered radiation produced by the von Laue conditions, for the particular geometry shown in part a. All scattered rays will extend along the surface of one of the cones. (g) Diffraction pattern of the array, resulting from the intersection of the scattering cones with the cylindrical film. (h) The actual scattering seen is the product of the atomic scattering shown in part b with the diffraction pattern of part g. (i) An alternative scattering geometry with the array parallel to the direction of incident radiation. (j) The scattered rays allowed by the von Laue conditions in the geometry of part i. (k) The array diffraction pattern resulting from the geometry of part i. (l) The product of the diffraction pattern of part k with the atomic scattering of part b.

ferent vectors S now correspond to different scattering angles 2θ . Consider each scatterer just as a single atom. Then, if the sample had only a single atom at the origin, the scattering would be given by Equation 13-23 (Fig. 13-9b).

The effect of the linear array is to allow finite intensity only at scattering geometries corresponding to the intersection of the set of planes ($\mathbf{a} \cdot \mathbf{S} = h$, for $h = 0, \pm 1, \pm 2, \dots$) with the sphere of reflection. For each scattering vector S drawn to one of these points of intersection, there corresponds a ray of scattered radiation. From Equation 13-3, this ray propagates in the direction $\hat{s} = \lambda S + \hat{s}_0$ (Fig. 13-3).

To compute the pattern of scattered radiation, it is easiest to use the description of scattering shown in Figure 13-3b rather than the equivalent one shown in Figure 13-3a. The vector \hat{s} is placed along the \hat{s}_0 axis a distance $1/\lambda$ from the origin. In other words, \hat{s} can be shown as emanating from the center of the sphere of reflection. When drawn in this manner, \hat{s} points toward the tip of the corresponding scattering vector S (Figs. 13-3b and 13-9e).

The vectors \mathbf{a} and \hat{s}_0 are fixed by the choice of orientation of the sample and the incident beam. Because of the von Laue constraint, each scattering vector S extends from the origin to one of the planes spaced $1/a$ apart. Figure 13-9d,e shows two cross sections through the origin. In the plane defined by $\mathbf{S} \cdot \mathbf{a} = 0$, a continuous set of scattering vectors S is allowed. This leads to a continuous distribution of scattered radiation, which emanates from the sample in a circle parallel to the $\mathbf{S} \cdot \mathbf{a} = 0$ plane (Fig. 13-9f).

In the plane parallel to \mathbf{a} , only certain values of S are allowed. Thus, vectors describing scattered radiation appear only at certain deflection angles α (Figs. 13-9d). Elementary geometrical considerations indicate that $\sin \alpha = h\lambda/a$, where h is any integer such that $|h| \leq a/\lambda$. Each value of h leads to a cone of scattering (Fig. 13-9f). Where this cone intersects the cylindrical film, a ring of scattered intensity results. When the film is unrolled, this ring becomes a line, called a layer line. The various layer lines are all parallel, and their spacing increases progressively as $|h|$ increases. The lines are perpendicular to the linear array (Fig. 13-9g).

The film records scattering from the individual atom of Figure 13-9b only in the lines allowed by the array (Fig. 13-9g). This effect leads to the pattern of scattering shown in Figure 13-9h. Note that only a finite number of layer lines are seen because of the conditions imposed by the sphere of reflection. There is a maximal value of 1 for $\sin \alpha$. For the geometry shown in Figure 13-9c, this value will occur when \hat{s} is parallel to \mathbf{a} . Here the largest value of h that can be included within the sphere of reflection is $\pm |a|/\lambda$. For example, suppose $|a|$ is 5 Å, and λ is 1 Å. Then the integer h can have values only in the range $-5 \leq h \leq +5$; the diffraction pattern will have 11 layer lines.

Figure 13-9h shows that the intensities drop off as h increases. This occurs because the atomic scattering decreases as e^{-S^2} . As demonstrated in Figure 13-9d,e, large values of h tend to correspond to large values of $|S|$. The scattered intensity also drops off rapidly on each layer line as one moves from the center to the edges. This is because, along each line of scattering, larger angles inevitably correspond to longer lengths of the scattering vector, $|S|$ (see Fig. 13-9e).

The appearance of the scattering pattern depends markedly on the relative orientation of the incident beam (\hat{s}_0) and the repeating array (\mathbf{a}). For example, if the

array is rotated so that \mathbf{a} and $\hat{\mathbf{S}}_0$ are parallel (Fig. 13-9i), the scattering pattern changes from a series of lines to a series of concentric curves (Fig. 13-9k). These curves are elliptical because the intersection of a circle (the cone of scattered radiation) and a cylindrical surface with its long axis parallel to the plane of the circle (the film) is an ellipse.

X-ray scattering from a two-dimensional array of atoms

The results shown in Figures 13-8 and 13-9 are the basic ideas behind all x-ray crystallographic measurements. However, if they are to be useful in practice, one must extend them from a one-dimensional array to a three-dimensional crystal. First, consider a two-dimensional net of molecules (Fig. 13-10a). The periodicity of this net is defined by two vectors, \mathbf{a} and \mathbf{b} . In general, \mathbf{a} and \mathbf{b} are not perpendicular to one another, nor are they of the same length. The periodicity along \mathbf{a} will cause a set of scattering fringes at $\mathbf{S} \cdot \mathbf{a} = h$, exactly as for the one-dimensional array in Figure 13-8. The additional periodicity along \mathbf{b} causes a comparable set of fringes defined by $\mathbf{S} \cdot \mathbf{b} = k$, where k is any integer. By the arguments used earlier, you can see that these latter fringes are parallel planes perpendicular to the vector \mathbf{b} and spaced by equal increments $1/|\mathbf{b}|$ (Fig. 13-10b).

The x-ray scattering will have finite intensity only where both von Laue conditions ($\mathbf{S} \cdot \mathbf{a} = h$, and $\mathbf{S} \cdot \mathbf{b} = k$) are satisfied. This condition is met at the intersection of the two sets of planar fringes. That intersection is an array of parallel lines (Fig. 13-10c). The lines all are perpendicular to the plane defined by \mathbf{a} and \mathbf{b} . Experimentally,

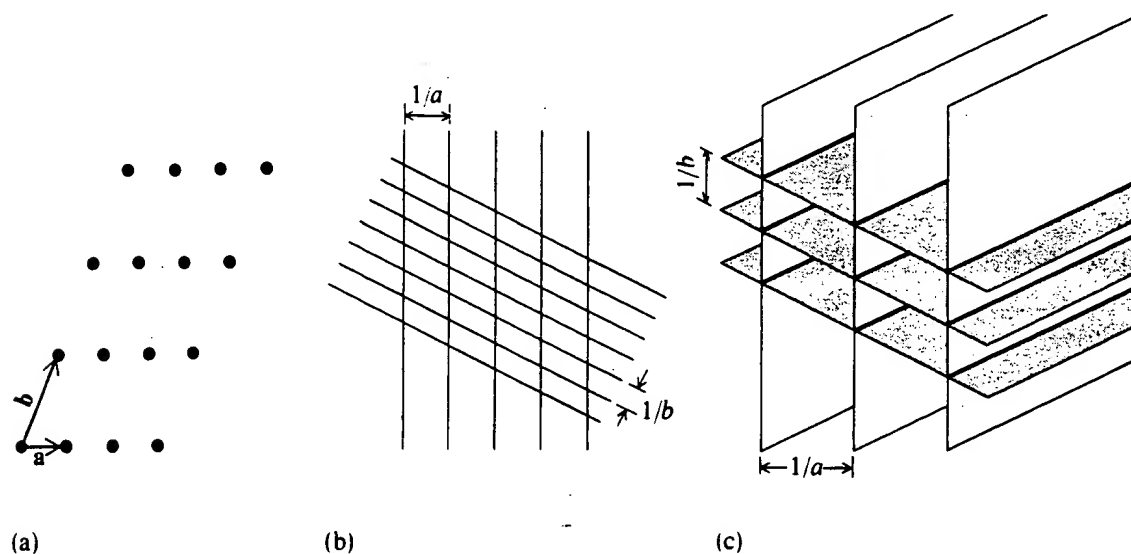


Figure 13-10

X-ray scattering from a two-dimensional array. (a) The array defined by \mathbf{a} and \mathbf{b} . (b) Parallel planes demonstrate the allowed positions of the scattering vector \mathbf{S} . Shown in cross section are planes spaced by $1/a$ perpendicular to \mathbf{a} , and planes spaced by $1/b$ perpendicular to \mathbf{b} . (c) The array of lines resulting from the intersection of the parallel planes shown in part b. Scattering vectors extending from the origin to any point along one of these lines will yield observable x-ray scattering intensity.

scattering intensity will be observed whenever the geometry of incident and diffracted radiation leads to a scattering vector that extends from the origin to a point along one of the arrays of parallel lines.

The greater restriction of scattering caused by a two-dimensional array means that more of the intensity will be concentrated at a smaller number of sets of scattering angles, 2θ . The effect of a two-dimensional array on the actual experimental scattering pattern is shown schematically in Figure 13-11. The plane of the array is perpendicular to the direction of incident x rays. If the array is considered as the effect of two perpendicular one-dimensional arrays, each alone would produce a set of scattering fringes. The x-ray diffraction pattern is the product of the two sets of fringes. In this case, the scattered radiation detected by the x-ray film consists of a series of spots, each occurring at the intersection of two fringes. (See Box 13-4 for examples of the optical diffraction of two-dimensional arrays.)

X-ray diffraction from a three-dimensional array of atoms

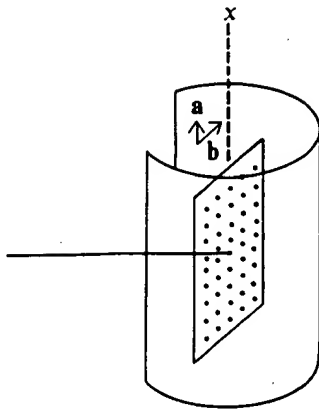
It is easy mathematically to generalize x-ray scattering to three dimensions, but it is not so easy to visualize the results. For an array such as that found in a real three-dimensional crystal, there is now a third periodicity defined by the vector \mathbf{c} (Fig. 13-12a). This leads to a third set of planar scattering fringes given by $\mathbf{S} \cdot \mathbf{c} = l$, where $l = 0, \pm 1, \pm 2, \dots$. This set of fringes intersects the parallel lines generated by $\mathbf{S} \cdot \mathbf{a} = h$ and $\mathbf{S} \cdot \mathbf{b} = k$. The result is a three-dimensional lattice of points, spaced evenly by $1/|\mathbf{a}|$ in the direction perpendicular to \mathbf{a} , by $1/|\mathbf{b}|$ perpendicular to \mathbf{b} , and by $1/|\mathbf{c}|$ perpendicular to \mathbf{c} (Fig. 13-12b). Diffracted radiation will be observed only when the scattering vector \mathbf{S} intersects one of the lattice points. It is not easy to illustrate the actual diffraction pattern from a three-dimensional crystal because it is a three-dimensional pattern.

Note that the lattice that describes allowed scattering geometries is not the same as the lattice of points that represents the positions of the atoms in the array. The position lattice has spacings \mathbf{a} , \mathbf{b} , and \mathbf{c} , whereas the spacings in the diffraction lattice, \mathbf{a}^* , \mathbf{b}^* , and \mathbf{c}^* , are related to the inverse of these. This scattering lattice is called the reciprocal lattice. The vector space it occupies is called the reciprocal space (Fig. 13-12c).

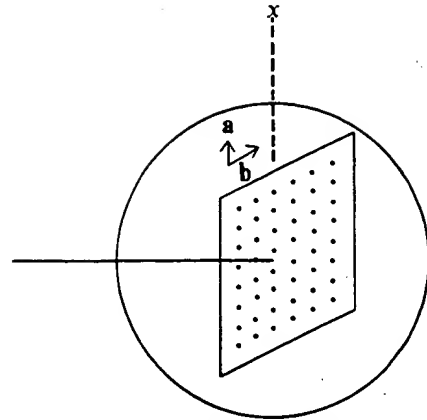
The array (crystal) we have described thus far contains only a single atom per repeating unit. The positions of the atoms define a set of cells bounded by \mathbf{a} , \mathbf{b} , and \mathbf{c}

Figure 13-11

X-ray scattering observed in the laboratory for a two-dimensional array perpendicular to the direction of incident radiation. Each part shows patterns for both cylindrical and spherical film. (a) Sample geometries. (b) Layer lines resulting from the \mathbf{a} periodicity of the array. (c) Layer lines resulting from the \mathbf{b} periodicity of the array. (d) Actual scattering observed is the product of the functions shown in parts b and c with the atomic scattering pattern shown in Figure 13-9b.

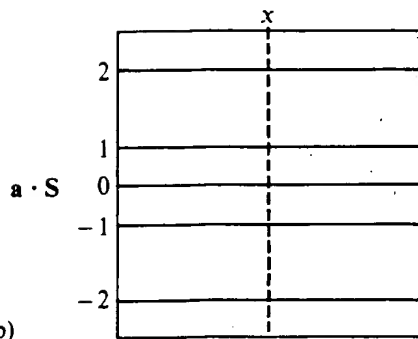


Cylindrical film

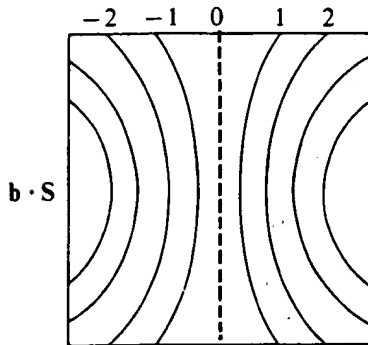


Spherical film

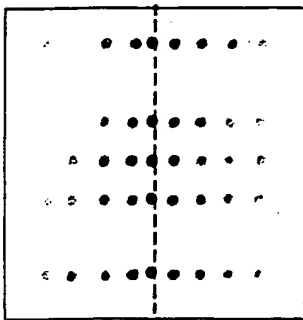
(a)



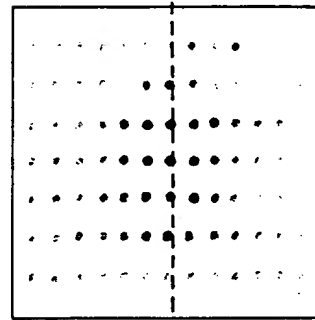
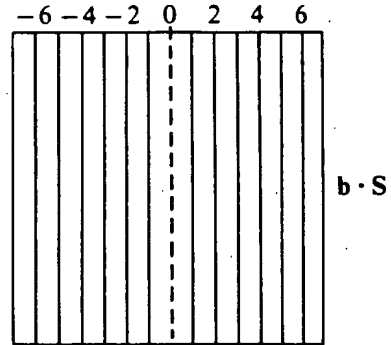
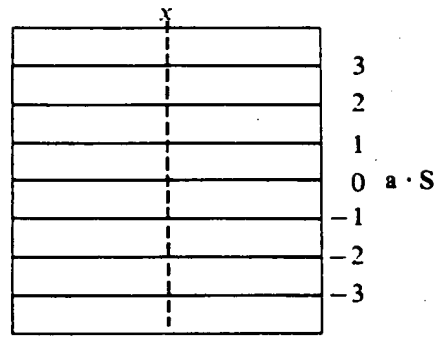
(b)



(c)

Actual
diffraction
including
 $f(s)$ 

(d)



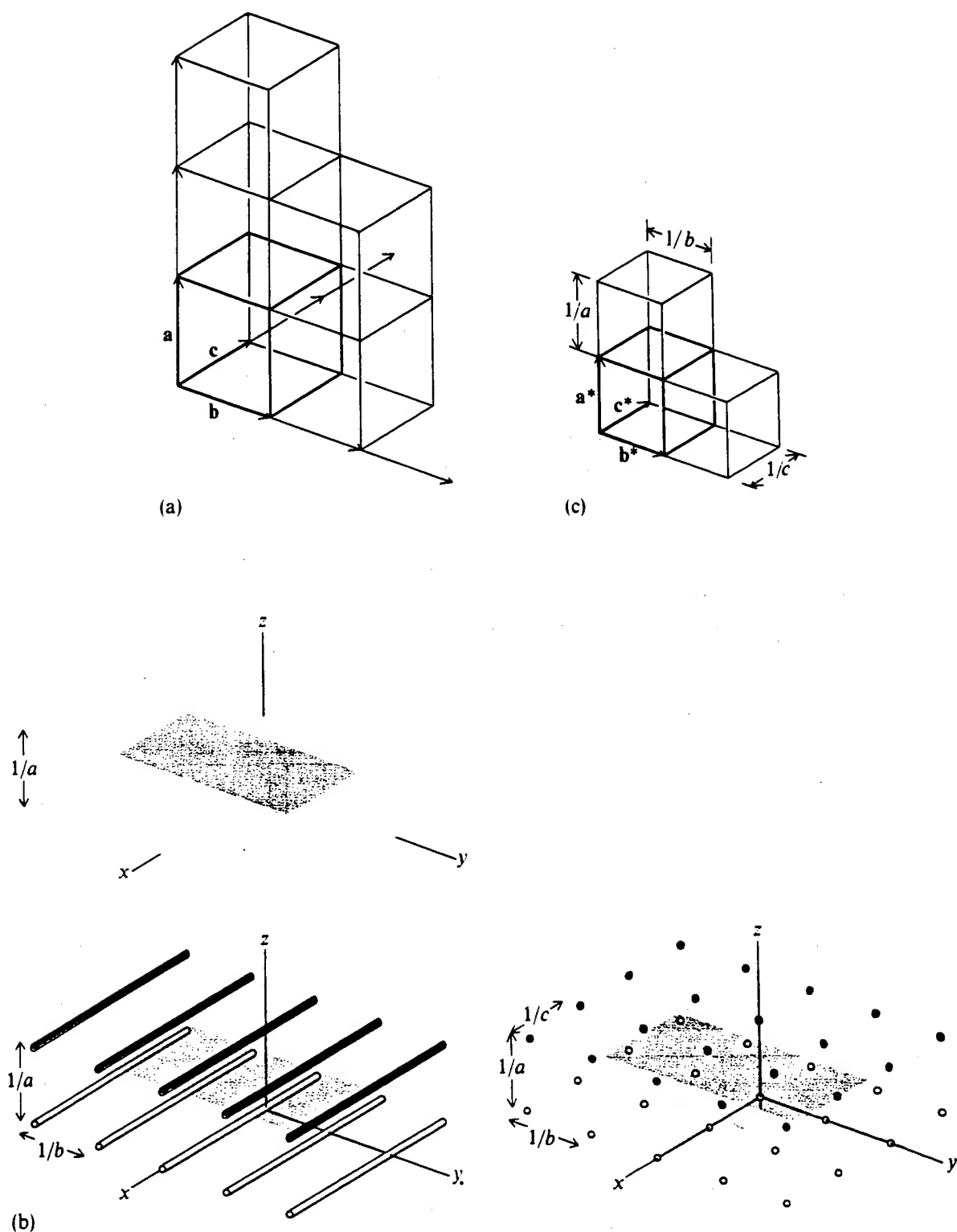


Figure 13-12

Three-dimensional arrays. (a) Vectors a , b , and c define the array. (b) Scattering planes resulting from each one-dimensional periodicity intersect to give lines for each two-dimensional periodicity and points for each three-dimensional periodicity. The array of points that results is the reciprocal lattice. (c) The reciprocal lattice is generated by the vectors a^* , b^* , and c^* . Several cells of the reciprocal lattice are shown. Scattering vectors extending from the origin to these points result in observed intensity.

(Fig. 13-12a). It is convenient to express the position of the atoms in terms of a coordinate system defined by these vectors. A vector drawn from the origin to the j th atom position is $\mathbf{r} = x\mathbf{a} + y\mathbf{b} + z\mathbf{c}$. Because the atoms lie at the corners of the cells, x , y , and z must be integers.

The vector \mathbf{r} can be used to calculate the x-ray scattering from the array. From Equation 13-27, the structure factor is a sum over all atom positions:

$$F_{\text{Tot}}(S) = \sum_x \sum_y \sum_z f(S) e^{2\pi i S \cdot (x\mathbf{a} + y\mathbf{b} + z\mathbf{c})} \quad (13-36)$$

Inserting the von Laue conditions ($\mathbf{S} \cdot \mathbf{a} = h$, etc.), we can rewrite this as

$$F_{\text{Tot}}(h, k, l) = \sum_x \sum_y \sum_z f(S) e^{2\pi i (hx + ky + lz)} \quad (13-37)$$

where h , k , and l are any integers. Every diffracted ray can be computed by choosing the appropriate integral values of h , k , and l and summing over the array. Note that, for an array of identical atoms, each exponential term in Equation 13-37 is simply unity, because h , k , l , x , y , and z are all integers. Therefore, Equation 13-37 becomes

$$F_{\text{Tot}}(h, k, l) = Nf(S) \quad (13-38)$$

where N is the number of atoms in the array, and $f(S)$ is the atomic scattering factor, now evaluated only at the particular values of S allowed by integral choices of h , k , and l . Thus the x-ray scattering is just the single-atom scattering sampled at all points in reciprocal space allowed by the von Laue conditions imposed by the lattice.

Equation 13-37 is a Fourier series rather than a Fourier transform because of the discrete nature of the diffraction pattern. However, it can be inverted in exactly the same way as a transform. By analogy to Equation 13-8, the electron density distribution of the array will be given by

$$\rho(x, y, z) = (1/NV) \sum_{h=-\infty}^{\infty} \sum_{k=-\infty}^{\infty} \sum_{l=-\infty}^{\infty} F_{\text{Tot}}(h, k, l) e^{-2\pi i (hx + ky + lz)} \quad (13-39)$$

where V is the volume of one unit cell, $V = \mathbf{a} \cdot \mathbf{b} \times \mathbf{c}$, so that NV is the volume of the entire array. The presence of the volume factor V in Equation 13-39 is easy to rationalize. $F(h, k, l)$ is proportional to the number of electrons, whereas ρ (an electron density) has units of electrons per unit volume.

X-ray diffraction from a three-dimensional molecular crystal

Although Equations 13-37, 13-38, and 13-39 were derived for an array with only one atom at the corner of each cell, it can be shown that similar equations hold for any real crystal. The repeating element of a crystal is defined as a unit cell. The crystal is a lattice of unit cells, each defined by the vectors **a**, **b**, and **c** (Fig. 13-12a). Whatever is inside each cell—whether a single atom, a molecule, or many molecules—the pattern of electron density repeats periodically throughout the crystal by translation along the vectors **a**, **b**, and **c**. Therefore, the von Laue conditions still apply and restrict the sampling of the structure factor to only those points defined by the reciprocal lattice. Now, however, what is sampled is not the atomic scattering factor. It is instead a molecular structure factor, or unit cell structure factor, given by Equation 13-27. In order to show this, it is useful to employ a mathematical device known as a convolution.

A repeating structure as a convolution

X-ray diffraction examines both the properties of the crystal lattice and the structure of individual molecules. The distribution of electron density within each unit cell is identical. The lattice describes how this distribution is replicated into a three-dimensional pattern. Such a repeating structure can be very conveniently described as a convolution.

Consider two arbitrary one-dimensional functions, $f(x)$ and $g(x)$. The functions f and g both are defined along the x axis. Their convolution product is defined as

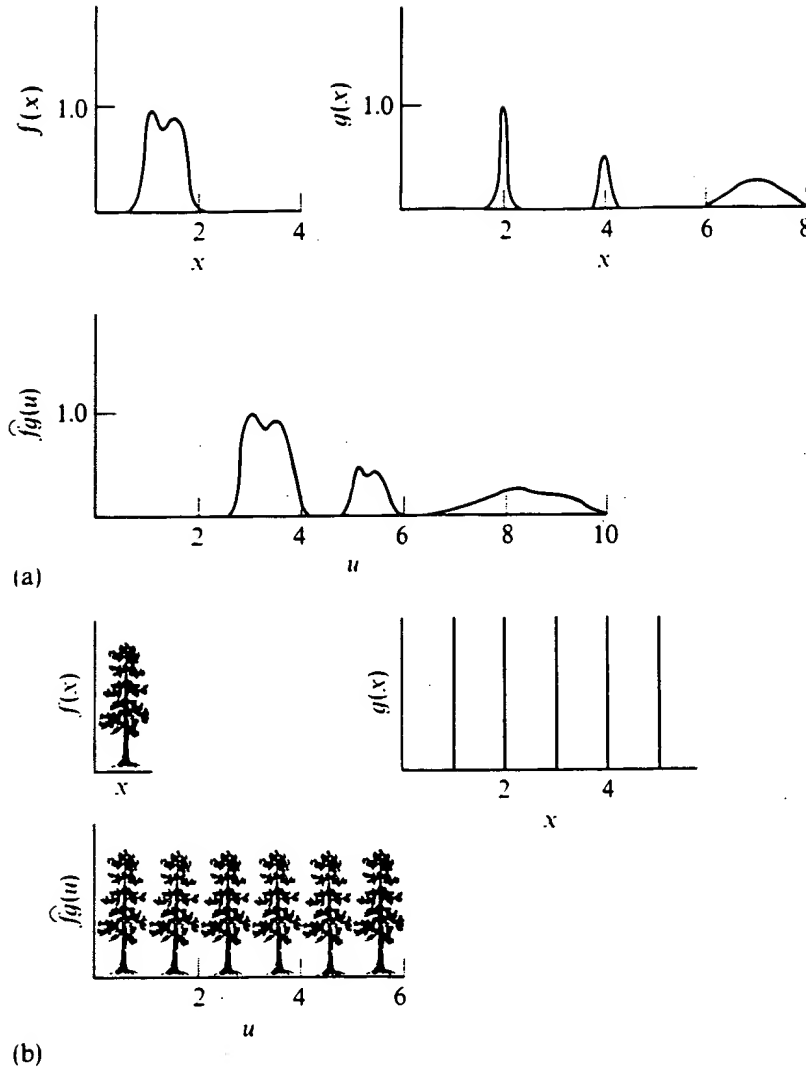
$$\hat{f}g(u) = \int_{-\infty}^{\infty} dx f(x)g(u-x) \quad (13-40)$$

where the variable u can take on any value that x can. It is equivalent to x , except that it is held constant in the integral.

We will try to develop a physical picture of the convolution product. See the example shown in Figure 13-13a. The function $g(u)$ plotted along the u axis is identical to a plot of $g(x)$ along the x axis. The function $g(u-x)$ plotted along the u axis is just the function $g(u)$ shifted in space by an amount x . Therefore, in the convolution product, the function g is placed successively at all points along the u axis, but it is multiplied by a weighting factor, $f(x)$, for each shift in position x . All the weighted values of g are added or integrated to produce the final convolution.

Physically, the convolution $\hat{f}g(u)$ means that one is laying down successive images of g weighted by f .[§] It turns out to be equivalent to say that one is laying down images of f weighted by g . To see this, let $x' = u - x$ in Equation 13-40. Then $dx' = -dx$, and

[§] If this is not absolutely clear, stop right here. Study Figure 13-13a; try calculating a convolution product for the *simple* functions of your choice.

**Figure 13-13**

Convolution integrals. (a) Two functions f and g and their convolution calculated by Equation 13-40. (b) Two functions—a tree, f , and a lattice (set of delta functions), g —and their convolution.

(taking note of the reversal of the limits of integration)

$$\widehat{fg}(u) = - \int_{+\infty}^{-\infty} dx' f(u - x') g(x') = \widehat{gf}(u) \quad (13-41)$$

because x and x' are just dummy variables.

Suppose the function g is the Dirac delta function, $\delta(x - a)$. Then the convolution

$$\widehat{f\delta}(u) = \int_{-\infty}^{\infty} dx f(x) \delta[u - (x - a)] = f(u + a) \quad (13-42)$$

just shifts the function the distance a along the u coordinate system. In three dimensions, all the same results hold. The convolution product is

$$\widehat{fg}(\mathbf{u}) = \int d\mathbf{r} f(\mathbf{r}) g(\mathbf{u} - \mathbf{r}) \quad (13-43)$$

If g is the three-dimensional delta function, $\delta(\mathbf{r} - \boldsymbol{\rho})$, the convolution integral defined in Equation 13-43 merely shifts the function $f(\mathbf{r})$ along the vector $\boldsymbol{\rho}$ in the \mathbf{u} coordinate system.

Delta functions can be used to describe a lattice. It is sufficient to define the origin of each unit cell. In one dimension, the origin can be any integral multiple of the vector \mathbf{a} . This restricts values of x that define the origin to na . A function that describes one of these values is $\delta(x - na)$. Thus, an infinite one-dimensional lattice is given by the function

$$L(x) = \sum_{n=-\infty}^{\infty} \delta(x - na) \quad (13-44)$$

This function really is just a list of all the lattice points.

Suppose that the electron density distribution within one cell of the lattice is $\rho(x)$. Then to describe the crystal, we want to replicate this electron density in each unit cell. From the properties of the convolution integral described above, this is done by

$$\text{Crystal} = \widehat{L\rho}(u) = \int_{-\infty}^{\infty} dx \rho(x) \sum_{n=-\infty}^{\infty} \delta[u - (x - na)] = \sum_{n=-\infty}^{\infty} \rho(u + na) \quad (13-45)$$

The convolution $\widehat{L\rho}$ simply lays down an image of the structure in each unit cell (Fig. 13-13b):

In three dimensions, an infinite lattice is described by

$$L(\mathbf{r}) = \sum_{n=-\infty}^{\infty} \sum_{m=-\infty}^{\infty} \sum_{p=-\infty}^{\infty} \delta(\mathbf{r} - n\mathbf{a} - m\mathbf{b} - p\mathbf{c}) \quad (13-46)$$

where n , m , and p are any integers. The electron density within one cell is $\rho(\mathbf{r})$, and the crystal is described by

$$\text{Crystal} = \widehat{L\rho}(\mathbf{u}) = \sum_{n=-\infty}^{\infty} \sum_{m=-\infty}^{\infty} \sum_{p=-\infty}^{\infty} \rho(\mathbf{u} + n\mathbf{a} + m\mathbf{b} + p\mathbf{c}) \quad (13-47)$$

Thus any crystal can be described as the convolution of the contents of one unit cell with the lattice.

The Fourier transform of a convolution

There is a property of convolutions that makes them especially useful for describing x-ray scattering. Suppose that $f(\mathbf{r})$ and $g(\mathbf{r})$ are functions that can be expressed as the Fourier transforms of the functions $F(\mathbf{S})$ and $G(\mathbf{S})$:

$$f(\mathbf{r}) = \int_{-\infty}^{\infty} d\mathbf{S} F(\mathbf{S}) e^{-2\pi i \mathbf{S} \cdot \mathbf{r}} \quad (13-48a)$$

$$g(\mathbf{r}) = \int_{-\infty}^{\infty} d\mathbf{S} G(\mathbf{S}) e^{-2\pi i \mathbf{S} \cdot \mathbf{r}} \quad (13-48b)$$

and, consequently, F and G are inverse transforms of f and g :

$$F(\mathbf{S}) = \int_{-\infty}^{\infty} d\mathbf{r} f(\mathbf{r}) e^{2\pi i \mathbf{S} \cdot \mathbf{r}} \quad (13-49a)$$

$$G(\mathbf{S}) = \int_{-\infty}^{\infty} d\mathbf{r} g(\mathbf{r}) e^{2\pi i \mathbf{S} \cdot \mathbf{r}} \quad (13-49b)$$

Then the convolution product of the two functions can be written as

$$\begin{aligned} \widehat{fg}(\mathbf{u}) &= \int_{-\infty}^{\infty} d\mathbf{r} f(\mathbf{r}) g(\mathbf{u} - \mathbf{r}) \\ &= \int_{-\infty}^{\infty} d\mathbf{r} \int_{-\infty}^{\infty} d\mathbf{S} F(\mathbf{S}) e^{-2\pi i \mathbf{S} \cdot \mathbf{r}} \int_{-\infty}^{\infty} d\mathbf{S}' G(\mathbf{S}') e^{-2\pi i \mathbf{S}' \cdot (\mathbf{u} - \mathbf{r})} \end{aligned} \quad (13-50)$$

Rearranging the order of the integrals, we obtain

$$\widehat{fg}(\mathbf{u}) = \int_{-\infty}^{\infty} d\mathbf{S} F(\mathbf{S}) \int_{-\infty}^{\infty} d\mathbf{S}' G(\mathbf{S}') e^{-2\pi i \mathbf{S}' \cdot \mathbf{u}} \int_{-\infty}^{\infty} d\mathbf{r} e^{2\pi i (\mathbf{S}' - \mathbf{S}) \cdot \mathbf{r}} \quad (13-51)$$

The third integral is just the Dirac delta function, $\delta(\mathbf{S}' - \mathbf{S})$ (see Box 13-3). Therefore, the result of the second integral is just to set $\mathbf{S}' = \mathbf{S}$, and Equation 13-51 becomes

$$\widehat{fg}(\mathbf{u}) = \int_{-\infty}^{\infty} d\mathbf{S} F(\mathbf{S}) G(\mathbf{S}) e^{-2\pi i \mathbf{S} \cdot \mathbf{u}} \quad (13-52)$$

Note that Equation 13-52 is just the Fourier transform of the product of the two functions $F(\mathbf{S})$ and $G(\mathbf{S})$.

This is an important conclusion. The Fourier transform of the product of two functions, F and G , is the convolution product of their two Fourier transforms, f and g . We can derive a second important result by Fourier-transforming Equation 13-52:

$$\int_{-\infty}^{\infty} d\mathbf{u} e^{2\pi i \mathbf{S}' \cdot \mathbf{u}} \widehat{fg}(\mathbf{u}) = \int_{-\infty}^{\infty} d\mathbf{u} \int_{-\infty}^{\infty} d\mathbf{S} F(\mathbf{S}) G(\mathbf{S}) e^{-2\pi i \mathbf{S} \cdot \mathbf{u}} e^{2\pi i \mathbf{S}' \cdot \mathbf{u}}$$

$$= \int_{-\infty}^{\infty} dS F(S) G(S) \int_{-\infty}^{\infty} d\mathbf{u} e^{2\pi i(\mathbf{S}' - \mathbf{S}) \cdot \mathbf{u}} \quad (13-53)$$

However, the second integral is just the Dirac delta function, $\delta(\mathbf{S}' - \mathbf{S})$. Thus,

$$\int_{-\infty}^{\infty} d\mathbf{u} e^{2\pi i \mathbf{S}' \cdot \mathbf{u}} \widehat{f g}(\mathbf{u}) = F(\mathbf{S}') G(\mathbf{S}') \quad (13-54)$$

The Fourier transform of a convolution product is just the product of the Fourier transforms of the two convoluted functions.

Convolutions in the computation of x-ray scattering

Consider a one-dimensional molecular crystal. Within each unit cell, the electron density distribution is $\rho_m(\mathbf{r})$. The x-ray scattering from the contents of a single cell located at the origin is given by Equation 13-7:

$$F_m(\mathbf{S}) = \int_{-\infty}^{\infty} d\mathbf{r} \rho_m(\mathbf{r}) e^{2\pi i \mathbf{S} \cdot \mathbf{r}} \quad (13-55)$$

The lattice is generated by the vector \mathbf{a} , and the lattice can be described by Equation 13-44 expressed in three dimensions:[§]

$$L(\mathbf{r}) = \sum_{n=-\infty}^{\infty} \delta(\mathbf{r} - n\mathbf{a}) \quad (13-56)$$

The crystal is generated by the convolution

$$\widehat{\rho_m L}(\mathbf{u}) = \int_{-\infty}^{\infty} d\mathbf{r} \rho_m(\mathbf{r}) \sum_{n=-\infty}^{\infty} \delta[\mathbf{u} - (\mathbf{r} - n\mathbf{a})] \quad (13-57)$$

The x-ray scattering from the crystal, using Equation 13-7, is

$$F_{\text{Tot}}(\mathbf{S}) = \int_{-\infty}^{\infty} d\mathbf{r} e^{2\pi i \mathbf{S} \cdot \mathbf{u}} \widehat{\rho_m L}(\mathbf{u}) \quad (13-58)$$

This expression can be evaluated by using Equations 13-54 and 13-49, and changing from the variable \mathbf{u} to the equivalent variable \mathbf{r} :

$$F_{\text{Tot}}(\mathbf{S}) = \left(\int_{-\infty}^{\infty} d\mathbf{r} \rho_m(\mathbf{r}) e^{2\pi i \mathbf{S} \cdot \mathbf{r}} \right) \left(\int_{-\infty}^{\infty} d\mathbf{r} \sum_{n=-\infty}^{\infty} \delta(\mathbf{r} - n\mathbf{a}) e^{2\pi i \mathbf{S} \cdot \mathbf{r}} \right) \quad (13-59)$$

[§] Even with a one-dimensional molecular crystal, one must formally consider a three-dimensional diffraction pattern, because the relative orientation of the molecule within the lattice will affect the scattering.

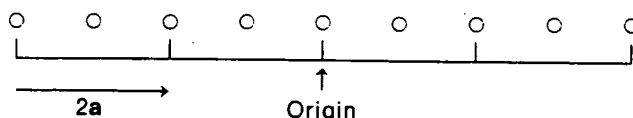
The first term is just the structure factor of a single unit cell, $F_m(S)$ (Eqn. 13-55). The second term is the sampling function generated by the lattice, $F_L(S)$. It is evaluated simply by using the properties of the delta function. The result is

$$F_{\text{Tot}}(S) = F_m(S)F_L(S) = F_m(S) \sum_{n=-\infty}^{\infty} e^{2\pi i n S \cdot a} \quad (13-60)$$

This result is identical in form with Equation 13-31. However, it is more general because it holds for molecular crystals. This example shows the correctness and simplicity of the convolution approach. However, its real advantage is the physical insight that can be gained once one is used to it.

Equations 13-59 and 13-60 mean that, to calculate x-ray scattering, one can simply multiply the scattering expected from one unit cell by the sampling function generated by the lattice.

Another example of this approach will demonstrate its usefulness. Consider an infinite one-dimensional crystal with a cell length $2a$ and two identical atoms per cell, one at the vertex and one halfway between adjacent vertices:



Let us calculate the x-ray scattering expected for such a crystal. From Equation 13-59, we evaluate the unit-cell structure factor as

$$F_m(S) = \int_{-\infty}^{\infty} d\mathbf{r} \rho_m(\mathbf{r}) e^{2\pi i \mathbf{S} \cdot \mathbf{r}} = f(S)(1 + e^{2\pi i \mathbf{S} \cdot a}) \quad (13-61)$$

where we have used the definition of the atomic scattering factor. One must consider only two atoms—one at a vertex (say, the origin), and one at the center of the cell—because the atom spaced $2a$ away from the origin will be counted as part of the next unit cell, and the atom $-a$ from the origin is counted as part of the preceding unit cell.

The lattice shown leads to a sampling function

$$F_L(S) = \int_{-\infty}^{\infty} d\mathbf{r} \sum_{n=-\infty}^{\infty} \delta(\mathbf{r} - 2n\mathbf{a}) e^{2\pi i \mathbf{S} \cdot \mathbf{r}} = \sum_{n=-\infty}^{\infty} e^{4\pi i n \mathbf{S} \cdot a} \quad (13-62)$$

Thus, the x-ray-scattering-expected for the crystal is

$$\begin{aligned} F_{\text{Tot}}(S) &= f(S)(1 + e^{2\pi i \mathbf{S} \cdot a}) \sum_{n=-\infty}^{\infty} e^{4\pi i n \mathbf{S} \cdot a} \\ &= f(S) \sum_{n=-\infty}^{\infty} (e^{4\pi i n \mathbf{S} \cdot a} + e^{4\pi i (n+1/2) \mathbf{S} \cdot a}) \end{aligned} \quad (13-63)$$

By writing out the sum in the final expression term by term, we can easily show it to be equal to

$$F_{\text{Tot}}(\mathbf{S}) = f(\mathbf{S}) \sum_{n=-\infty}^{\infty} e^{2\pi i n \mathbf{S} \cdot \mathbf{a}} \quad (13-64)$$

This is identical to Equation 13-31, illustrating the important result that the scattering calculated for a crystal does not depend on how we choose to define the unit cell.

Calculation of x-ray scattering from a molecular crystal using convolutions

To treat a real crystal, one must extend Equations 13-55 and 13-56 to three-dimensional arrays. The crystal is generated by the convolution $\rho_m L$, where $L(\mathbf{r})$ is given by Equation 13-46. Evaluating this (exactly in the way it was done in Equations 13-59 and 13-60) yields the structure factor of the crystal:

$$F_{\text{Tot}}(\mathbf{S}) = F_m(\mathbf{S}) \sum_{n=-\infty}^{\infty} \sum_{m=-\infty}^{\infty} \sum_{p=-\infty}^{\infty} e^{2\pi i (n\mathbf{S} \cdot \mathbf{a} + m\mathbf{S} \cdot \mathbf{b} + p\mathbf{S} \cdot \mathbf{c})} \quad (13-65)$$

The triple sum in Equation 13-65 is the three-dimensional sampling function generated by the lattice. It limits the detection of scattered intensity to geometries allowed by the von Laue conditions. Applying these conditions, we can evaluate $\mathbf{S} \cdot \mathbf{a} = h$, and $\mathbf{S} \cdot \mathbf{b} = k$, and $\mathbf{S} \cdot \mathbf{c} = l$ to obtain

$$F_{\text{Tot}}(h, k, l) = F_m(\mathbf{S}) \sum_{n=-\infty}^{\infty} \sum_{m=-\infty}^{\infty} \sum_{p=-\infty}^{\infty} e^{2\pi i (nh + mk + pl)} \quad (13-66)$$

Now every exponential term is simply unity, and the triple sum simplifies to

$$F_{\text{Tot}}(h, k, l) = N F_m(\mathbf{S})$$

(13-67)

where N is the number of unit cells in the crystal.

It is convenient to write out the unit-cell structure factor, $F_m(\mathbf{S})$, explicitly in terms of the positions of each atom in the unit cell, and of the corresponding atomic scattering factors. Using Equation 13-27 for the molecular structure factor, we choose a coordinate system based on the unit-cell vectors \mathbf{a} , \mathbf{b} , and \mathbf{c} . The position of the j th atom in the unit cell is then

$$\mathbf{r}_j = x_j \mathbf{a} + y_j \mathbf{b} + z_j \mathbf{c} \quad (13-68)$$

where x_j , y_j , and z_j are now *fractions* of the corresponding unit-cell dimensions. Then Equation 13-27 becomes

$$F_m(\mathbf{S}) = \sum_j f_j(\mathbf{S}) e^{2\pi i(x_j \mathbf{S} \cdot \mathbf{a} + y_j \mathbf{S} \cdot \mathbf{b} + z_j \mathbf{S} \cdot \mathbf{c})} \quad (13-69)$$

where the sum is taken over all the atoms in one unit cell. However, $F_m(\mathbf{S})$ can be sampled only at geometries allowed by the von Laue conditions. When we apply these, equation 13-69 simplifies to

$$F_m(h, k, l) = \sum_j f_j(\mathbf{S}) e^{2\pi i(hx_j + ky_j + lz_j)} \quad (13-70)$$

This equation is called the structure factor equation. It represents the unit-cell x-ray scattering sampled at the reciprocal lattice points, h , k , and l .

Equation 13-70 is one of the key results in x-ray crystallography. It provides a direct way to calculate the x-ray diffraction of a crystal, provided that the structure of one unit cell is known. Alternatively, if the structure factor $F_m(h, k, l)$ is known, the electron density distribution of the crystal can be calculated. The equation used is identical to Equation 13-39. However, instead of using Equation 13-38 to describe the unit-cell contribution, one must use Equations 13-67 and 13-70.

• Bragg's law of diffraction

Most elementary treatments of x-ray diffraction discuss the process as the reflection of x rays from certain planes in the crystal lattice. Because this is probably the formalism many readers have seen previously, it is worthwhile to show how our present treatment is equivalent. Lattice points are defined as the corners (vertices) of the unit cells. Lattice planes are a set of equidistant parallel planes constructed so that all lattice points lie on some member of the set. Clearly, the planes passing through the faces of the unit cells of the lattice are one such set of planes. Planes passing through opposite vertices of the unit cells also are a set of lattice planes (Fig. 13-14a). These cut the axes (\mathbf{a} , \mathbf{b} , and \mathbf{c}) precisely at the values corresponding to one unit translation of the lattice. However, increasingly finer-spaced lattice planes can be drawn that cut the \mathbf{a} axis at any $a/2$, $a/3$, \dots , a/h of the unit translation (Fig. 13-14b,c).

In three dimensions, lattice planes exist that cut one axis every a/h while cutting another at b/k and the third at c/l . The planes can be described by specifying the Miller indices, h , k , and l . Note that the spacing (d) between adjacent planes is inversely related to the size of the indices of the planes. Therefore, it is reasonable that the planes could bear some relationship to the reciprocal lattice.

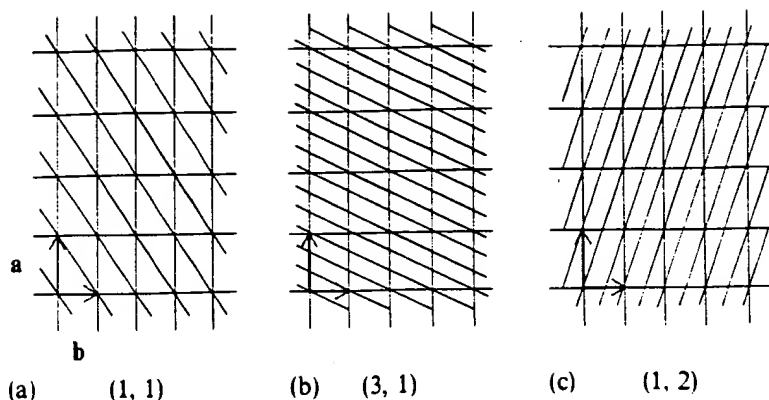


Figure 13-14

Three sets of lattice planes. Shown below each set are the Miller indices (h, k) that describe it.

In the Bragg's-law description of diffraction, an x-ray beam that impinges on a lattice plane at an angle θ is described as being reflected from that plane at an equal angle (Fig. 13-15a). This corresponds to a scattering angle 2θ . The Bragg conditions for observing diffraction require that the path difference between reflected beams from adjacent lattice planes be an integral number of wavelengths. From Figure 13-15a, we see that this condition clearly is met wherever

$$2d \sin \theta = n\lambda \quad (13-71)$$

where n is any integer, and d is the distance between two adjacent lattice planes.

To compare the Bragg treatment with our previous description, it is necessary to show how the scattering vector \mathbf{S} is related to a lattice plane. Consider a lattice plane that intersects the three axes of a unit cell at \mathbf{a}/h , \mathbf{b}/k , and \mathbf{c}/l (Fig. 13-15b). Let \mathbf{r} be a vector drawn from the origin to any point in this plane. Consider the properties of a scattering vector \mathbf{S} that happens to satisfy the equation $\mathbf{S} \cdot \mathbf{r} = 1$. For a fixed direction of \mathbf{S} , the relation $\mathbf{S} \cdot \mathbf{r} = 1$ defines a plane perpendicular to \mathbf{S} , because it simply means that the projection of \mathbf{r} on \mathbf{S} is a constant.

As we showed previously, not all values of \mathbf{S} lead to detectable scattering. Only those values that satisfy the von Laue conditions are acceptable. These conditions are $\mathbf{S} \cdot \mathbf{a} = h$, with equivalent equations for \mathbf{b} and \mathbf{c} . We can put the von Laue conditions in the form

$$\mathbf{S} \cdot \mathbf{a}/h = \mathbf{S} \cdot \mathbf{b}/k = \mathbf{S} \cdot \mathbf{c}/l = 1 \quad (13-72)$$

In other words, \mathbf{a}/h , \mathbf{b}/k , and \mathbf{c}/l are all values of \mathbf{r} that satisfy the condition $\mathbf{S} \cdot \mathbf{r} = 1$. These three values uniquely define a plane (Fig. 13-15b). This plane is a lattice plane (as described in Fig. 13-14), but it is also a plane containing values of \mathbf{S} that lead to x-ray diffraction.

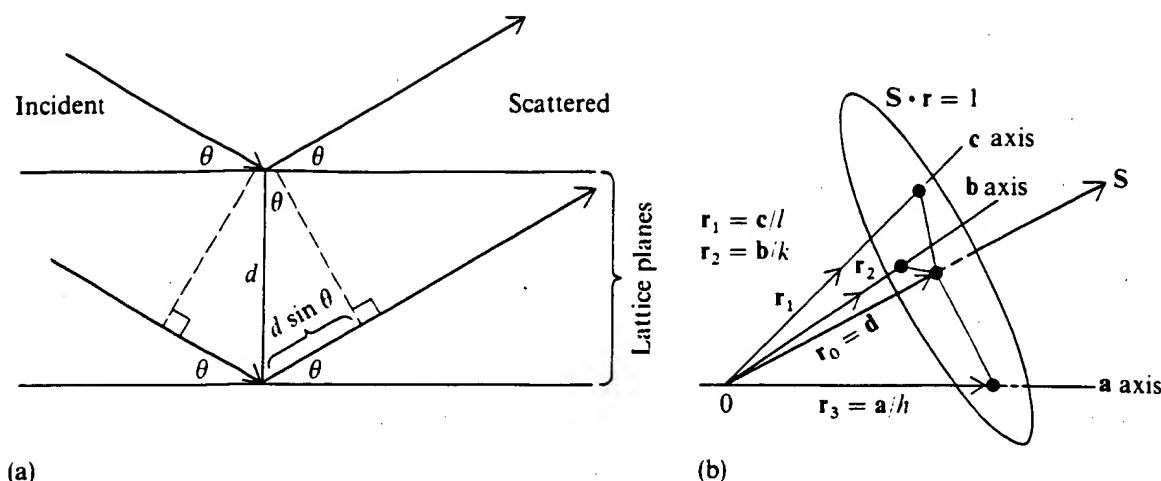


Figure 13-15

Derivation of Bragg's law. (a) Diffraction viewed as reflection of x rays from adjacent lattice planes. (b) The lattice plane (h, k, l) is a plane containing vectors that satisfy the von Laue scattering conditions.

The lattice plane adjacent to the plane defined by $\mathbf{S} \cdot \mathbf{r} = 1$ will pass through the origin. The spacing d between these two planes is the length of a vector \mathbf{r}_0 parallel to \mathbf{S} (Fig. 13-15b). The condition $\mathbf{S} \cdot \mathbf{r}_0 = 1$ means that $d = |\mathbf{r}_0| = 1/|\mathbf{S}|$. However, we showed earlier that $|\mathbf{S}| = 2|\sin \theta|/\lambda$. Therefore, the scattering angle (2θ) produced by crystal planes separated by a spacing d , is given by

$$\sin \theta = \lambda/2d \quad (13-73)$$

This is identical to Equation 13-71 with $n = 1$. Thus, the equivalence of the Bragg treatment and the von Laue conditions has been illustrated. (To derive the full Bragg equation, consider the properties of the plane defined by $\mathbf{S} \cdot \mathbf{r} = n$ where n is an integer.)

13-3 PROPERTIES OF CRYSTALS

A crystal is a three-dimensional ordered array of molecules. From the discussion of x-ray scattering in the previous section, it is clear that crystals are not a requirement for x-ray diffraction measurements. Any ordered (or partially ordered) array of molecules can, in principle, produce useful x-ray data. However, it is evident that crystals are the most favorable samples. A large ordered array leads to sharp diffraction spots, which concentrate the scattered intensity in small discrete regions of scattering angle (2θ). This greatly facilitates the acquisition of reliable intensity data.

If the sample is not a perfectly ordered crystal, intensity can reach observable levels over wider ranges of scattering angles. The diffraction pattern can smear into rings or streaks, and therefore considerable imprecision is introduced in assigning

values of θ observed. In general, only if the sample has three-dimensional order will the diffraction pattern contain all the information needed to reconstruct the three-dimensional structure. Disorder corresponds to averaging over orientations of both the lattice and the molecules it contains. The resulting data then contains only information about the averaged structure.

Restrictions on possible crystal lattices

A crystal is essentially a three-dimensional mosaic. The unit cell defined by the vectors **a**, **b**, and **c** contains the fundamental repeating unit. The crystal is generated by successive translations of the unit cell along the axes **a**, **b**, and **c**; in just the same way, a mosaic is built up by placing down multiple copies of the same unit structure. It is a fundamental consequence of geometry that three-dimensional space can be filled only by mosaics of cells of certain shapes. There are, in fact, only seven fundamental types of unit cells. Each defines a crystal system (Fig. 13-16; Table 13-1).

Each unit cell consists of a *motif* that is the actual unit repeated throughout the crystal by the lattice translations. The crystal is a convolution of the motif and the lattice (Fig. 13-17a). A motif can be a single atom or molecule, or it can contain more than one molecule.

The simplest possible crystals would have one motif positioned with the same orientation at each corner of the unit cells. There are eight corners and each is shared by eight unit cells. Therefore, there is one motif per unit cell. Such lattices are called primitive, and they are denoted by the letter *P*. It is always possible to choose a primitive triclinic cell for any lattice. This is the least-symmetric unit cell. Each dimension and each angle are different. So it takes six parameters to specify such a cell.

There are many cases in which the symmetry of the lattice can be increased if a larger unit cell containing additional lattice points located on the faces or at the center is chosen. These nonprimitive lattices have more than one copy of the motif per unit cell. By choosing a nonprimitive lattice, one often can describe the crystal with fewer parameters. There are a total of seven nonprimitive lattices (Fig. 13-16). They are designated *I* for cells having an extra lattice point at the center, *C* for cells with two extra lattice points on one pair of opposite faces, and *F* for cells with extra lattice points on all faces. You should be able to convince yourself that *C* and *I* lattices have two motifs per unit cell, whereas *F* lattices have four.

It is important to recognize that the choice of lattice is not always unique. Figure 13-18 shows a few examples of alternative choices. There are certain conventions that help to decide which lattice to use, but we need not be concerned with them here and, in any event, they are not always rigidly adhered to. For each type of lattice, there are only certain arrangements of molecules or motifs that can be inserted without reducing the lattice to one of greater symmetry or one with a smaller unit cell.

The choice of lattice can simplify the analysis of x-ray scattering data. However, it is important to reiterate the point made earlier that the x-ray scattering calculated for a crystal of known structure is independent of the choice of lattice.

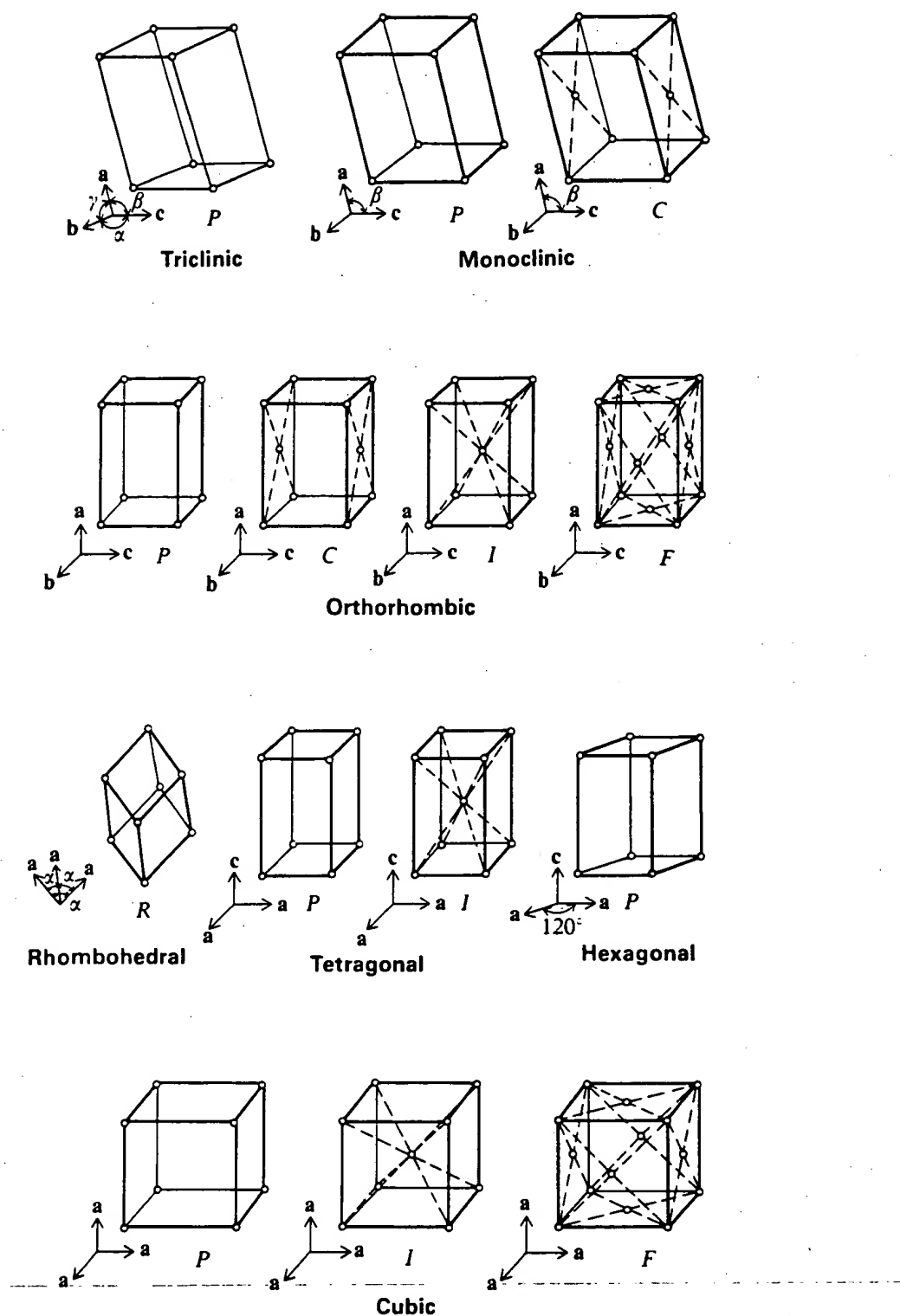


Figure 13-16

The fourteen Bravais lattices. For a list of their properties, see Table 13-1. [After G. H. Stout and L. M. Jensen, *X-Ray Structure Determination* (New York: Macmillan, 1968).]

Table 13-1

The 65 space groups allowed for molecules with no mirror or inversion symmetry

Crystal system	Number of independent parameters	Lattice	Minimum symmetry of unit cell	Unit cell edges and angles [†]	Diffraction pattern symmetry*	Space groups [‡]
Triclinic	6	<i>P</i>	None	$a \neq b \neq c$ $\alpha \neq \beta \neq \gamma$	$\bar{1}$	<i>P1</i>
Monoclinic	4	<i>P</i>	Twofold axis parallel to b	$a \neq b \neq c$ $\alpha = \gamma = 90^\circ$ $\beta \neq 90^\circ$	$2/m$	<i>P2</i> , <i>P2₁</i> <i>C2</i>
Orthorhombic	3	<i>P</i>	Three mutually perpendicular twofold axes	$a \neq b \neq c$ $\alpha = \beta = \gamma = 90^\circ$	<i>mmm</i>	<i>P222</i> , <i>P2₁2₁2₁</i> , <i>P222₁</i> , <i>P2₁2₁2₂</i> <i>C222</i> , <i>C222₁</i> [<i>I222</i> , <i>I2₁2₁2₁</i>] <i>F222</i>
		<i>C</i>				
		<i>I</i>				
		<i>F</i>				
Tetragonal	2	<i>P</i>	Fourfold axis parallel to c	$a = b \neq c$ $\alpha = \beta = \gamma = 90^\circ$	$4/m$	<i>P4</i> , (<i>P4₁</i> , <i>P4₃</i>), <i>P4₂</i> <i>I4</i> , <i>I4₁</i>
		<i>I</i>				<i>P422</i> , (<i>P4₁22</i> , <i>P4₃22</i>), <i>P4₂22</i> , <i>P42₁2</i> , (<i>P4₁2₁2</i> , <i>P4₃2₁2</i>), <i>P4₂2₁2</i> <i>I422</i> , <i>I4₁22</i>
Trigonal/ rhombohedral	2	<i>R</i> ^{§§}	Threefold axis parallel to c	$a = b = c$ $\alpha = \beta = \gamma \neq 90^\circ$	$\bar{3}$	<i>R3</i>
		<i>P</i> ^{§§}				<i>P3</i> , (<i>P3₁</i> , <i>P3₂</i>) <i>R32</i> [<i>P321</i> , <i>P312</i>], [(<i>P3₁21</i> , <i>P3₂21</i>), (<i>P3₁12</i> , <i>P3₂12</i>)]
Hexagonal	2	<i>P</i>	Sixfold axis parallel to c	$a = b \neq c$ $\alpha = \beta = 90^\circ$ $\gamma = 120^\circ$	$6/m$ $6/mmm$	<i>P6</i> , (<i>P6₁</i> , <i>P6₅</i>), <i>P6₃</i> , (<i>P6₂</i> , <i>P6₄</i>) <i>P622</i> , (<i>P6₁22</i> , <i>P6₅22</i>), <i>P6₃22</i> , (<i>P6₂22</i> , <i>P6₄22</i>)
						<i>P23</i> , <i>P2₁3</i> [<i>I23</i> , <i>I2₁3</i>] <i>F23</i>
Cubic	1	<i>P</i>	Threefold axes along cube diagonals	$a = b = c$ $\alpha = \beta = \gamma = 90^\circ$	$m\bar{3}$	<i>P432</i> , (<i>P4₁32</i> , <i>P4₃32</i>), <i>P4₂22</i>
		<i>I</i> <i>F</i>				<i>I432</i> , <i>I4₁43</i> <i>F432</i> , <i>F4₁32</i>

§ See Figure 13-16 for definitions of edge and angle symbols.

* A number with an overbar indicates a rotary inversion axis; $2/m$ = a mirror plane perpendicular to a twofold axis; $6/m$ indicates a mirror plane perpendicular to a sixfold axis.

† Pairs of space groups in parentheses differ from each other only in that they are enantiomorphs. Space groups enclosed in brackets (and also those in parentheses) cannot be distinguished from one another by systematic extinctions of reflections in the diffraction pattern. All other space groups can be assigned on the basis of the diffraction pattern.

‡ The rhombohedral system often is regarded as a subdivision of the hexagonal system, and unit cells in this system may be chosen on either hexagonal or rhombohedral axes.

SOURCE: After D. Eisenberg, in *The Enzymes*, 3d ed., vol. 1, P. D. Boyer (New York: Academic Press, 1970).

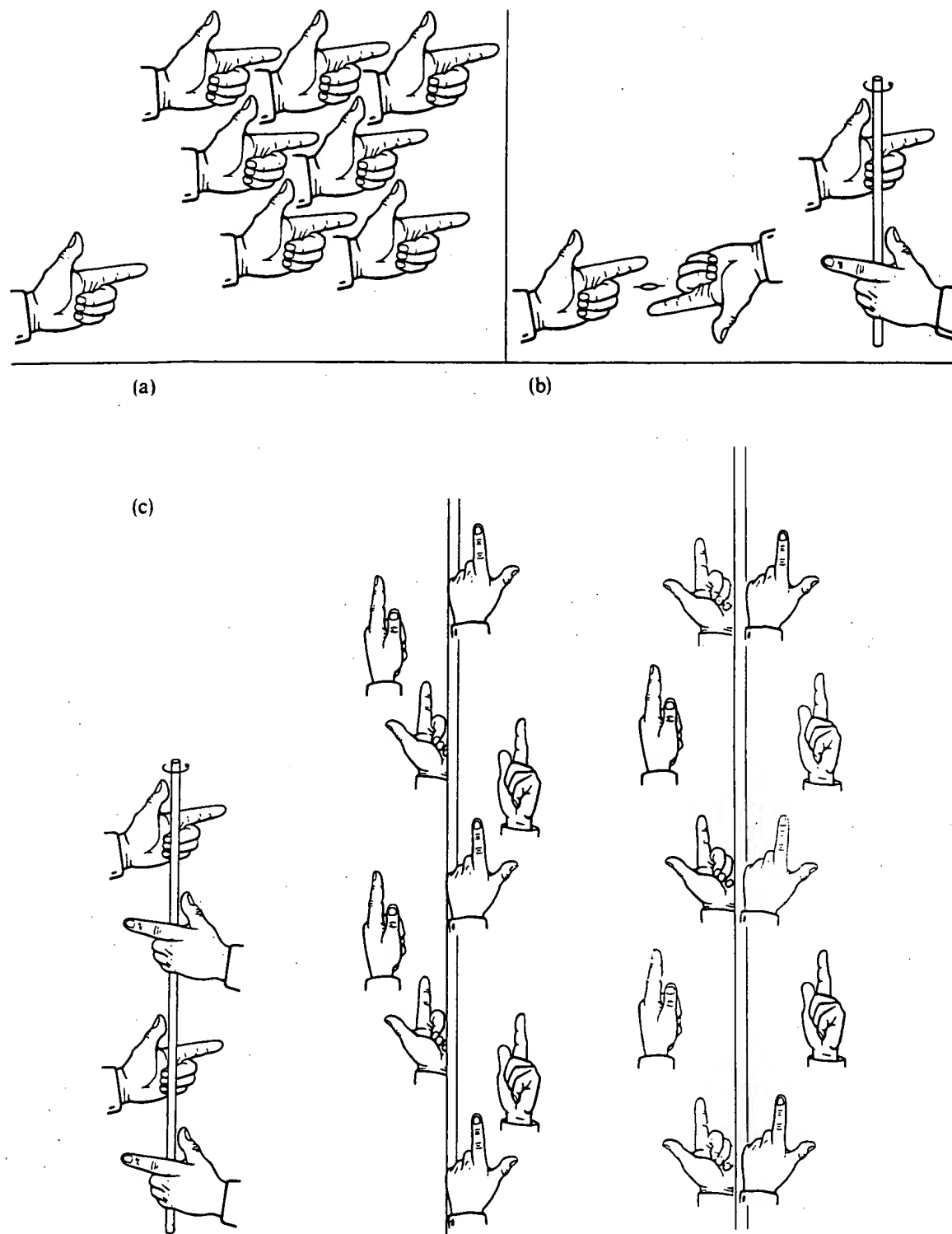


Figure 13-17

Motifs, lattices, and symmetry operations. (a) A lattice and simple motif (a single hand). The crystal is the convolution of the motif and the lattice. (b) Two motifs containing symmetry-related structures. The two hands on the left are related by a twofold rotation (C_2) axis. The two hands on the right are related by a 2_1 screw axis. In each structure, the motif consists of two hands. The asymmetric unit is just a single hand. (c) Arrays generated by screw axes. From left to right, the axes are 2_1 , 4_1 , and 4_2 ; the resulting unit cells have 2, 4, and 4 asymmetric units, respectively. [Drawings by Irving Geis.]

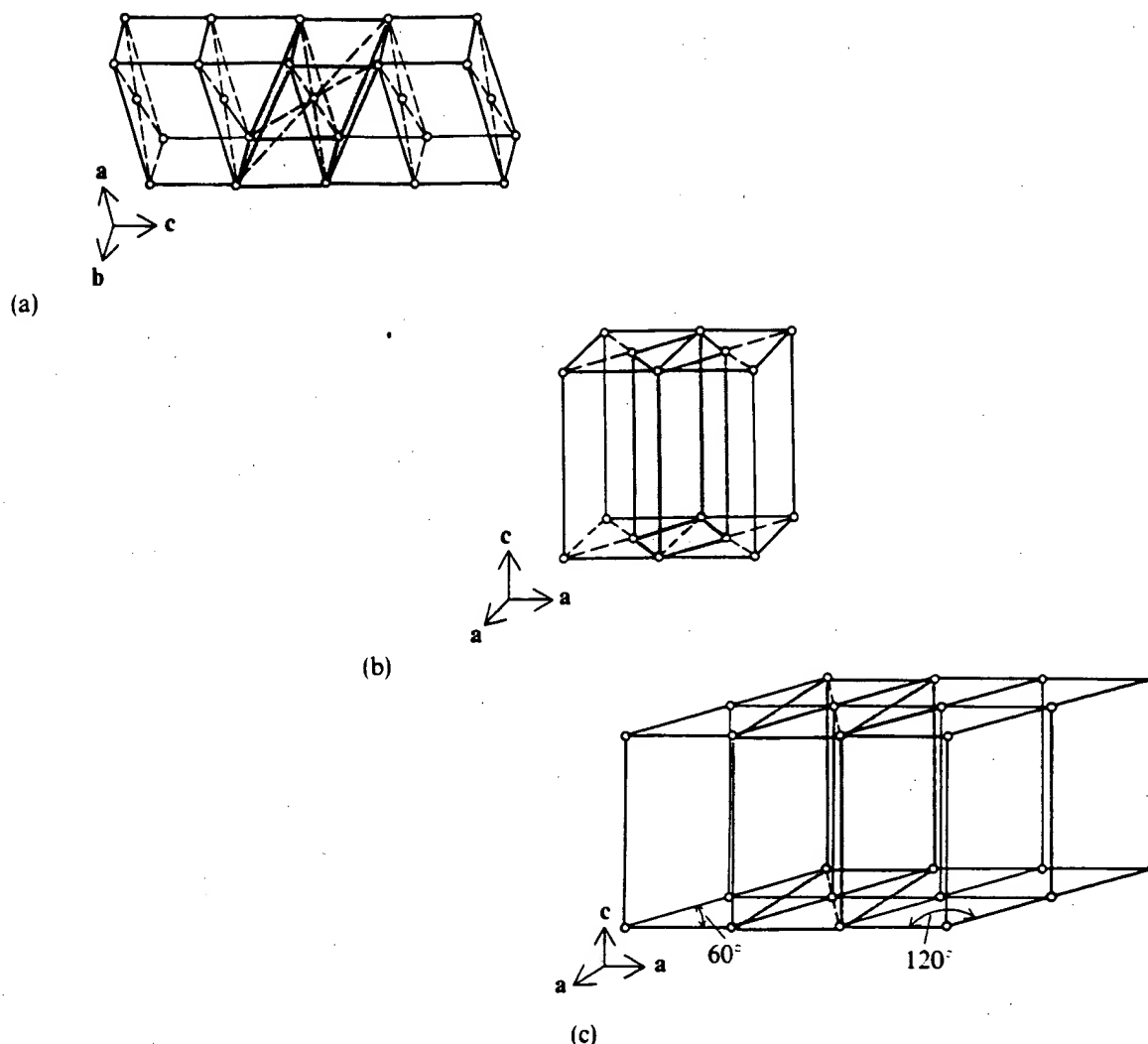


Figure 13-18

*Choosing different unit cells for the same lattice. (a) Choice of C or I unit cells in a monoclinic lattice. (b) Choice of C or P unit cells in a tetragonal lattice. (c) Choice of an orthorhombic C lattice or a hexagonal P lattice. [After G. H. Stout and L. M. Jensen, *X-Ray Structure Determination* (New York: Macmillan, 1968).]*

Symmetry properties of molecules and crystals

The overall symmetry of the crystal is called the space group. It is described by naming the type of unit cell and any symmetry relationships *within* the molecules that make up the motif. For arbitrary structures, it turns out that there are precisely 230 possible space groups. These contain two types of symmetry: point symmetry and space symmetry.

Point-symmetry operations consists of manipulations of an isolated object that

leave at least one point in space unchanged (Box 2-3). These can include

1. *rotation axes*, named by a number (2 for twofold axis, 3 for threefold axis, and so on);
2. *mirror planes*, designated by m ;
3. *rotation coupled with reflection* (for example, combining a twofold rotation axis with a mirror plane perpendicular to it, resulting in inversion of an object through an origin located at the intersection of the rotation axis and the mirror plane; this operation is designated $2/m$);
4. *rotation-inversion axes*, designated by a number with an overbar (for example, $\bar{4}$ indicates that each rotation of 90° is accompanied by inversion through the origin).

A point group is a list of all of the point-symmetry relationships possessed by an object. The object can be a molecule, a set of molecules, or an entire crystal. Several of the point groups possible for molecules consisting of multiple copies of identical subunits are illustrated in Chapter 2.

Space-symmetry operations involve translation of the object. These include *screw axes* (which are a rotation accompanied by translation) and *glide planes* (which are translations accompanied by reflection). Screw axes are called n_m , where n is the rotation axis, and m/n is the fraction of a unit cell along which the translation occurs. For example, 3_1 indicates a rotation of 120° accompanied by a translation $1/3$ of the unit-cell length. The description of glide planes is complicated, because it depends on which face or diagonal the glide is along, as well as on how far the glide occurs. Figure 13-17c shows a few examples of motif-symmetry operations.

The presence of particular symmetry elements in the motif restricts the possible type of unit cell. For example, if a twofold rotation axis is present in the space group, this axis must be perpendicular to two unit-cell vectors. Otherwise, this symmetry operation would leave the motif unaltered internally, but would change its location within the unit cell. The presence of threefold or higher rotation axes requires that the two unit-cell vectors perpendicular to the axis must be equal in length.

Space groups available to biological molecules

The allowed combinations of the point and space symmetry possessed by the motif generate the 230 space groups. It is convenient to introduce the concept of an *asymmetric unit*. This is the smallest unit from which the crystal structure can be generated by making use of the symmetry operations of the space group. The asymmetric unit can be several molecules, one molecule, or a subunit of an oligomeric molecule. The crystal is generated, first by creating the motif by the space-group symmetry operations on the asymmetric unit, and then by translation of the motif through the lattice.

The number of asymmetric units per unit cell, n' , is determined by the space group.

For biological molecules, the motifs inevitably contain asymmetric carbon atoms. Therefore, the symmetry arrangement of the molecules can never contain mirror planes, glide planes, centers of symmetry, or rotation inversion axes. Only 65 of the 230 space groups can apply to biological molecules. The biologically relevant space groups can contain 1, 2, 3, 4, 6, 8, 12, 24, 48, or 96 asymmetric units per unit cell (Table 13-1).

A practicing crystallographer presumably will learn to picture many of these space groups. However, molecules seem to prefer to crystallize in only a limited number of space groups. For example, 80% of 1,200 organic compounds surveyed fell into the triclinic, monoclinic, or orthorhombic crystal classes, and half of these occurred in just three space groups. Figure 13-19 shows a few of the most commonly found of the space groups allowable for biological molecules. Note that these different groups imply different numbers of molecules per unit cell.

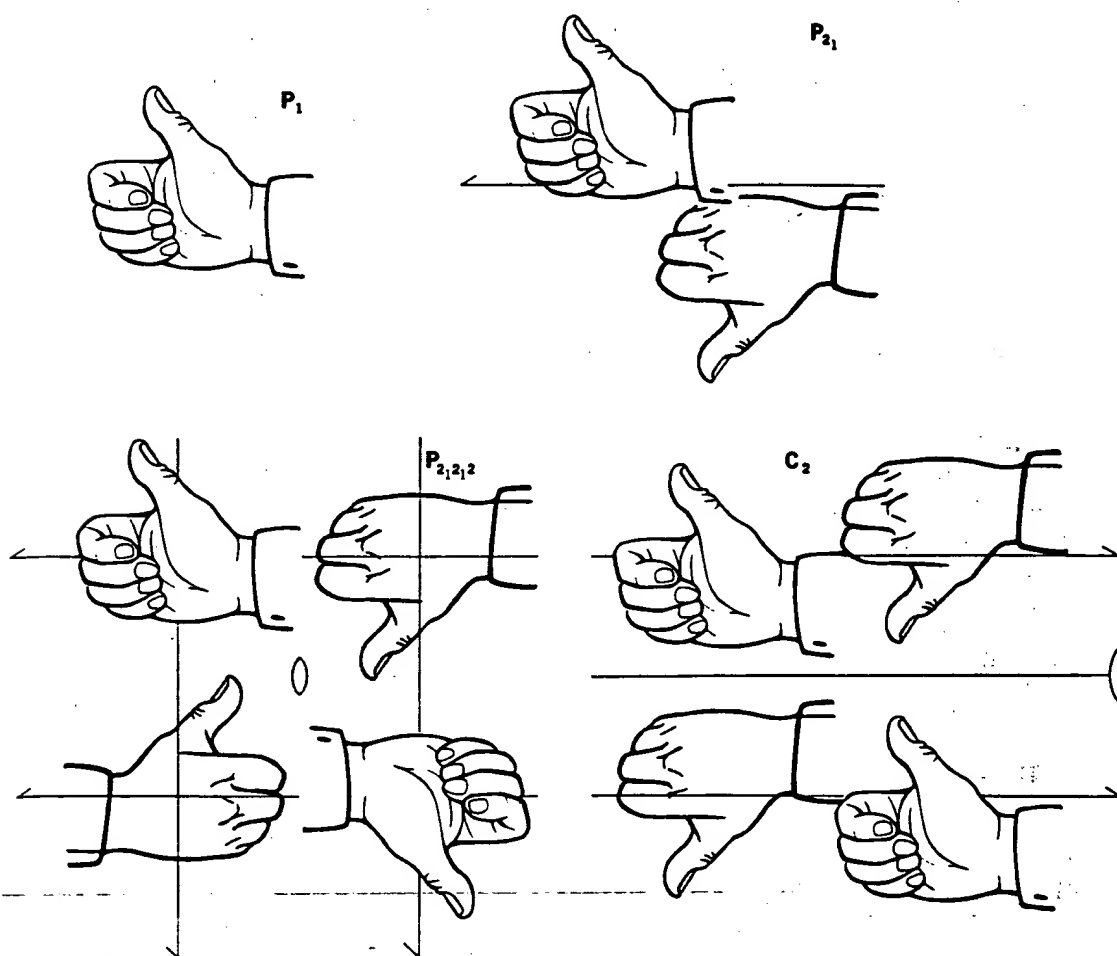


Figure 13-19

A familiar asymmetric unit as it might appear in four different space groups. P₁ has no motif symmetry; P₂₁ has a single 2₁ screw axis shown as a half-arrow; P₂₁₂₁₂ has four screw axes (each 2₁) and a C₂ axis perpendicular to the plane of the page; C₂ has two 2₁ screw axes and a C₂ rotational axis shown as the full arrow. [Drawings by Irving Geis.]

Determination of the dimensions of the crystal lattice

X-ray diffraction occurs whenever the scattering vector coincides with a reciprocal lattice point, as we have shown. That means that the resulting diffraction pattern can be used to construct an image of the reciprocal lattice. From the spacing between diffraction spots as actually observed in the laboratory and a knowledge of the geometry of the diffraction experiment, one can compute the spacing between points on the reciprocal lattice. This in turn allows the geometry of the unit cell to be calculated.

Here we shall demonstrate the determination of the spacing of a one-dimensional crystal. The crystal is placed in the center of a cylindrical film (Fig. 13-20). The von Laue conditions for the \mathbf{a} crystal axis require that $\mathbf{S} \cdot \mathbf{a} = h$. Consider the first two diffraction planes, which will occur at $h = 0$ and $h = 1$. If we make measurements with the crystal oriented so that \mathbf{S} is parallel to \mathbf{a} , then the length of the scattering vector, \mathbf{S} , is 0 for $h = 0$ and is $1/a$ for $h = 1$. The scattering angle is computed from Equation 13-5; $|\mathbf{S}| = 2|\sin \theta|/\lambda$. For $h = 0$, we have $\sin \theta = 0$ and $\theta = 0$. For $h = 1$, we have $\sin \theta = \lambda|\mathbf{S}|/2 = \lambda/2a$. Therefore, the angle between the two scattering planes is $2\theta = 2 \sin^{-1} \lambda/2a$. Thus, if θ is measured experimentally, and if λ is known, the distance a can be computed.

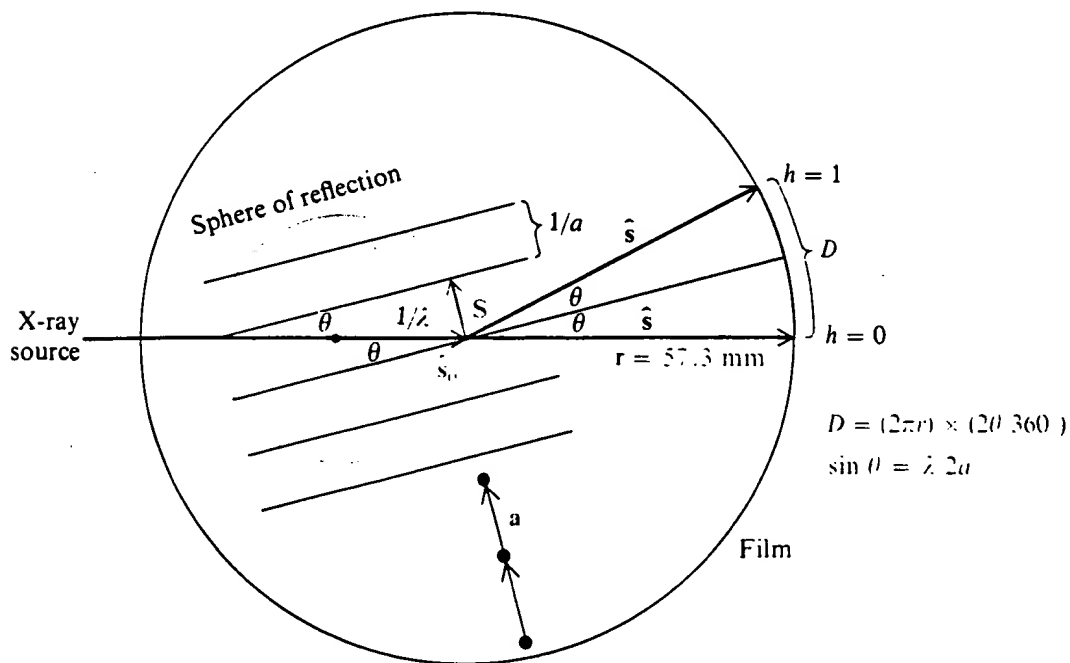


Figure 13-20

Experimental scattering geometry. Shown are a sample at the origin, a section of the reciprocal lattice, one scattering vector \mathbf{S} (and the scattered radiation associated with it), and two layer lines as they intersect the film. Below the reciprocal lattice, three atoms in the actual crystal lattice are illustrated to show the orientation of the sample. In this example, for clarity, we show values of $\lambda/2a$ and θ much larger than the values typically encountered in actual experiments.

In a typical case, λ might be 1 Å, and a might be 10 Å. Therefore, $\sin \theta$ is 1/20, or θ is about 3° . A common x-ray camera would have film arranged in a cylinder 28.65 mm in radius. Its circumference is $2\pi \times 28.65$ mm. The angle between the $h = 0$ and $h = 1$ scattering planes is 2θ . This is 6° , or $6/360$ the circumference of the film. Therefore, the distance between the two scattering planes as they intersect the film is $2\pi \times 28.65 \times 6/360 \cong 3$ mm.

Note that, although the actual crystal spacings are very small, the film is placed far away from the sample. This magnifies the diffraction pattern until planes are physically separated by a distance convenient for measuring. In an unknown case, all one has to do is work the calculation backwards to obtain a . The actual equation is $a = \lambda/2 \sin (360D/4\pi r)$, where D is the physically measured spacing on the x-ray film, and r is the radius of the camera.

The relationship between the crystal lattice and the reciprocal lattice

Real crystals are three-dimensional. The reciprocal lattice that one sees in an x-ray diffraction pattern also is three-dimensional. It is related in a simple way to the actual crystal lattice. By measuring the spatial pattern of diffracted spots, it is possible to compute the cell dimensions and shape of the reciprocal lattice. From this, the corresponding dimensions and shape of the unit cell of the actual crystal lattice can be derived.

Figure 13-21a shows that each of the vectors \mathbf{a}^* , \mathbf{b}^* , and \mathbf{c}^* defining the reciprocal cell is located along lines formed by the intersection of two planes. For example, \mathbf{c}^* is formed by the intersection of planes generated by successive values of h for the von Laue condition $\mathbf{a} \cdot \mathbf{S} = h$ (and therefore these planes are perpendicular to \mathbf{a}) and planes generated by $\mathbf{b} \cdot \mathbf{S} = k$ (and thus perpendicular to \mathbf{b}). This means that \mathbf{c}^* must be perpendicular to both \mathbf{a} and \mathbf{b} , and we can write, in general,

$$\mathbf{c}^* = r\mathbf{a} \times \mathbf{b} \quad (13-74a)$$

$$\mathbf{b}^* = q\mathbf{c} \times \mathbf{a} \quad (13-74b)$$

$$\mathbf{a}^* = p\mathbf{b} \times \mathbf{c} \quad (13-74c)$$

These constants control the magnitudes of the reciprocal-cell vectors. To determine the constants, we must use the von Laue conditions that generate the reciprocal lattice. For example, the condition $\mathbf{S} \cdot \mathbf{c} = l$ generates a set of planes spaced by $1/c$. The vector \mathbf{c}^* extends between two such planes, although it is not necessarily normal to them (Fig. 13-21b). However, the projection of \mathbf{c}^* on \mathbf{c} must be $1/c$ (Fig. 13-21b). Thus we can write

$$\mathbf{c} \cdot \mathbf{c}^* = |\mathbf{c}|(1/c) = 1 \quad (13-75)$$

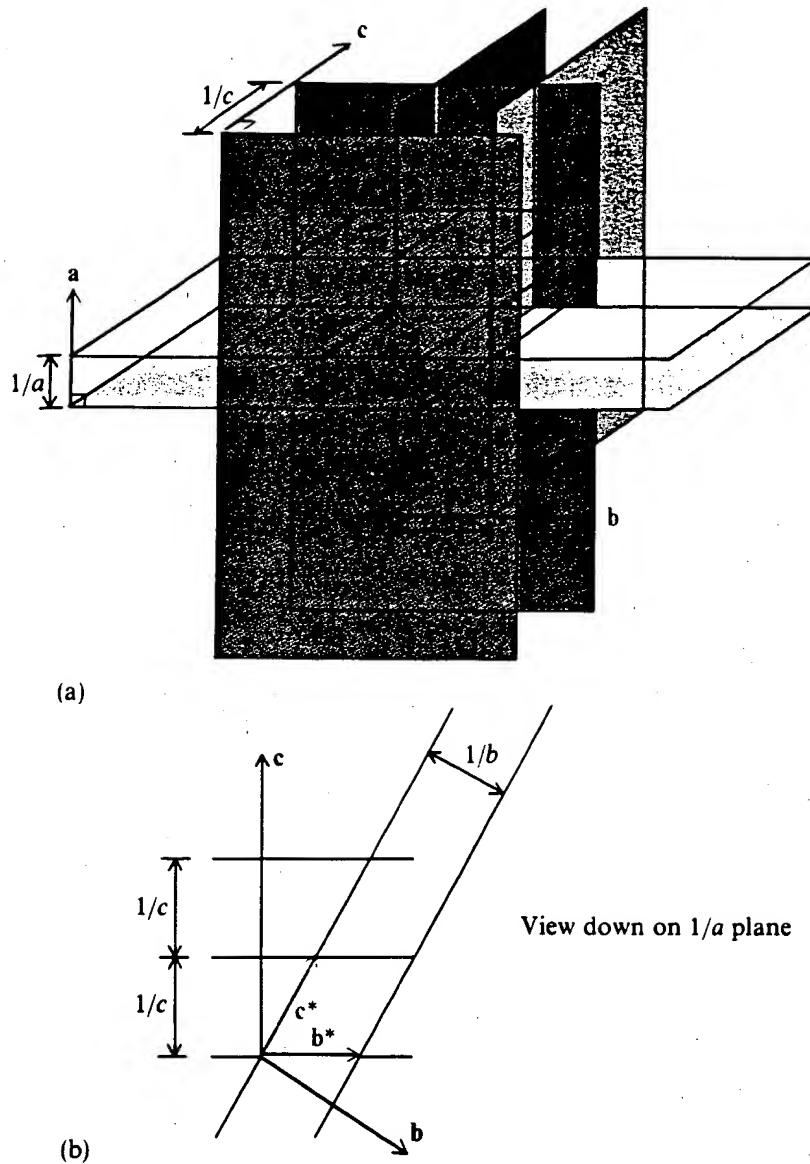


Figure 13-21

Geometrical properties of the reciprocal lattice. (a) Reciprocal-lattice vectors lie at the intersections of sets of parallel planes. For example, \mathbf{c}^* extends between two planes spaced $1/|\mathbf{c}|$ apart, but it is *formed* by the intersections of planes perpendicular to \mathbf{a} (spaced $1/|\mathbf{a}|$ apart) and planes perpendicular to \mathbf{b} (spaced $1/|\mathbf{b}|$ apart). (b) Demonstration that \mathbf{c}^* and \mathbf{c} are not necessarily parallel.

Similarly, one can show that $\mathbf{a} \cdot \mathbf{a}^* = 1$ and $\mathbf{b} \cdot \mathbf{b}^* = 1$.

When Equation 13-74 is inserted into Equation 13-75, the result is $1 = \mathbf{c} \cdot \mathbf{c}^* = r\mathbf{c} \cdot \mathbf{a} \times \mathbf{b}$, from which we can evaluate r . Carrying out equivalent manipulations for \mathbf{a}^* and \mathbf{b}^* , we obtain

$$r = 1/(\mathbf{c} \cdot \mathbf{a} \times \mathbf{b}) \quad q = 1/(\mathbf{b} \cdot \mathbf{c} \times \mathbf{a}) \quad p = 1/(\mathbf{a} \cdot \mathbf{b} \times \mathbf{c}) \quad (13-76)$$

Using the properties of the triple scalar product (see Box 8-2), each of these quantities is equal to the volume of the parallelepiped formed by the three vectors \mathbf{a} , \mathbf{b} , and \mathbf{c} . Thus, $r = q = p = 1/V$, where V is the volume of the unit cell of the crystal. Using Equations 13-74, 13-75, and 13-76, we can construct the reciprocal cell if the actual unit cell of the crystal is known. Figure 13-22 shows two examples.

In practice, observations of the geometric pattern of diffraction spots allow measurement of the reciprocal lattice vectors \mathbf{a}^* , \mathbf{b}^* , and \mathbf{c}^* . Then one must compute the unit-cell vectors. The procedures are quite similar to that just outlined. Note, for example, that \mathbf{b}^* and \mathbf{c}^* lie in a plane perpendicular to \mathbf{a} (Fig. 13-21). Therefore, $\mathbf{a} = r'\mathbf{b}^* \times \mathbf{c}^*$, and similar equations exist for \mathbf{b} and \mathbf{c} . To determine r' , one uses the constraint $\mathbf{a} \cdot \mathbf{a}^* = 1$. Then $r' = 1/(\mathbf{a}^* \cdot \mathbf{b}^* \times \mathbf{c}^*) = 1/V^*$, where V^* is the volume of the reciprocal cell. Thus, the unit cell is constructed from the measured diffraction data by

$$\mathbf{a} = (1/V^*)(\mathbf{b}^* \times \mathbf{c}^*) \quad (13-77a)$$

$$\mathbf{b} = (1/V^*)(\mathbf{c}^* \times \mathbf{a}^*) \quad (13-77b)$$

$$\mathbf{c} = (1/V^*)(\mathbf{a}^* \times \mathbf{b}^*) \quad (13-77c)$$

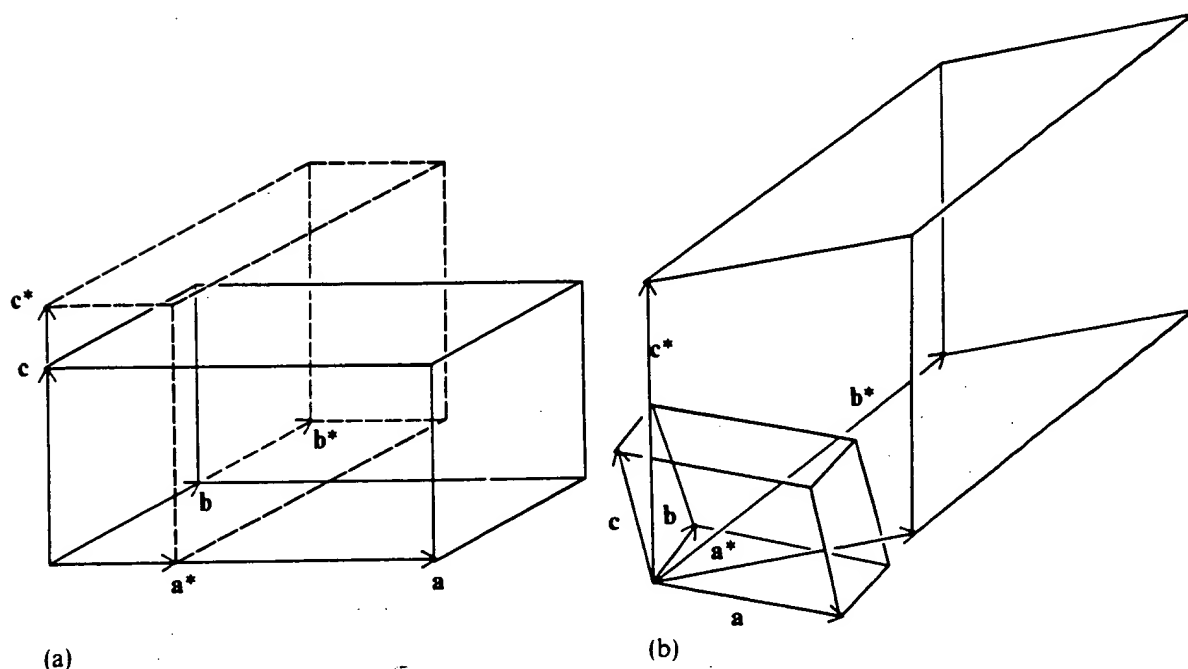


Figure 13-22

*Comparisons of direct and reciprocal unit cells. (a) For an orthorhombic crystal. (b) For a triclinic crystal. [After G. H. Stout and L. M. Jensen, *X-Ray Structure Determination* (New York: Macmillan, 1968).]*

A necessary consequence of Equations 13-74 and 13-77 is that the volumes of unit cells and reciprocal cells are inverse (see Guinier, 1963, p. 88):

$$V = 1/V^* \quad (13-78)$$

Determination of the space group

In addition to determining the unit cell, it is useful to establish the space group of the crystal. This shows if there is any internal symmetry, and whether one can use this symmetry to reduce the portion of the structure that must be solved. There is no general way to find the space group but, for many biological molecules, one can sharply narrow the possibilities by simple examination of the intensity of diffraction spots in the reciprocal lattice. Particular crystal classes show symmetries in the diffraction pattern that correspond to symmetries in the space group. For example, a twofold rotation axis in the crystal leads to a mirror plane in the diffraction pattern intensities.

Even more informative are systematic absences of intensity at certain points of the reciprocal lattice for many space groups. Consider a space group with a twofold screw axis along *c*. This axis rotates *x* to $-x$, rotates *y* to $-y$, and translates half of the unit-cell distance along *c*. Then, for each atom at $\mathbf{r} = x_j\mathbf{a} + y_j\mathbf{b} + z_j\mathbf{c}$, there must be an identical atom at $\mathbf{r}' = -x_j\mathbf{a} - y_j\mathbf{b} + (z_j + 1/2)\mathbf{c}$. In calculating the structure factor, one can group the identical atoms by pairs. From Equation 13-70,

$$F_m(h, k, l) = \sum_{j=1}^{N/2} f_j(S) (e^{2\pi i(hx_j + ky_j + z_j)} + e^{2\pi i(-hx_j - ky_j + lz_j + l/2)}) \quad (13-79)$$

When $h = k = 0$, the structure factor becomes

$$F_m(0, 0, l) = \sum_{j=1}^{N/2} f_j(S) [e^{2\pi i l z_j} (1 + e^{2\pi i l/2})] \quad (13-80)$$

Whenever *l* is odd, the exponential in the last term becomes equal to -1 , and so the scattering amplitude vanishes. Thus, there will be no diffraction in the special case $h = 0, k = 0, l = \text{odd}$. If such absences are not sufficient to uniquely determine the space group, sometimes a statistical analysis of the pattern of intensities can complete the assignment.

Crystallographic estimation of molecular weight

Once the lattice and space group are known, it frequently is possible to determine the molecular weight of the molecules that compose the crystals. The density of the

crystal, ρ_c , can be measured experimentally. Then the weight W of one unit cell can be computed as

$$W = \rho_c V \quad (13-81)$$

where V is the volume of the unit cell determined from the diffraction pattern.

In general, protein and other macromolecule crystals can be viewed as containing three components: anhydrous macromolecule (m), free solvent (s), and bound water (w). The weight of one unit cell will be the sum of the three components:

$$\rho_c V = \rho_m V_m + \rho_w V_w + \rho_s V_s \quad (13-82)$$

where V refers to the volume of each component, and ρ is its density. Usually, ρ_s is known experimentally, and ρ_w can be taken as the density of pure water.

We want to compute the weight of macromolecule per unit cell, $\rho_m V_m$. Thus, we must eliminate the unknown quantities V_w and V_s from Equation 13-82. The volume of bound water, V_w , can be written in terms of the hydration δ_1 , in grams water per gram macromolecule.

$$V_w = \delta_1 \rho_m V_m / \rho_w \quad (13-83)$$

Hydration values are known approximately for proteins and nucleic acids (Chapter 10). The total volume of the unit cell is

$$V = V_m + V_w + V_s \quad (13-84)$$

Using Equation 13-83, the volume of free solvent can be written as

$$V_s = V - V_m(1 + \delta_1 \rho_m / \rho_w) \quad (13-85)$$

Inserting Equations 13-83 and 13-85 into Equation 13-82, and solving the resulting expression for $\rho_m V_m$, we obtain

$$W_m = \rho_m V_m = \frac{V(\rho_c - \rho_s)}{1 - \rho_s/\rho_m + \delta_1(1 - \rho_s/\rho_w)} \quad (13-86)$$

Thus the weight of macromolecule per unit cell (W_m) can be calculated if the anhydrous density (ρ_m) is known. Usually it is a good approximation to equate ρ_m^{-1} with the partial specific volume (\bar{V}_m) measured for the macromolecule in solution.

If there is a single macromolecule per unit cell, then the molecular weight is just $M = N_0 W_m$ where N_0 is Avogadro's number. If the space group indicates n'

asymmetric units per unit cell, the molecular weight of an asymmetric unit is

$$M = N_0 W_m / n' \quad (13-87)$$

Alternative methods for determining the molecular weight of molecules in a crystal are discussed by B. W. Matthews (1975).

Often an estimate of the molecular weight is already available from hydrodynamic measurements or primary structure data. Then n' can be computed from a measurement of W_m . This value must always be an integer. Therefore, once an estimate of n' is available, it can be used to refine the value of the molecular weight.

Using the space group for information on macromolecule symmetry

In most cases, the number of molecules per unit cell (n) is equal to the number of asymmetric units (n'). Here we consider the special case where the macromolecule is an oligomer of identical subunits. For example, a molecule with five subunits might have C_5 symmetry. But this symmetry can never correspond to a symmetry element of the space group, because there is no space group with a C_5 rotation axis. Therefore, the asymmetric unit must contain all five subunits.

On the other hand, in many cases, a molecule with C_2 or C_3 rotational symmetry crystallizes so that its axis is also a symmetry axis of the motif. Then it is possible that the number of asymmetric units per cell will be an integral multiple of the number of subunits per unit cell, rather than a multiple of the number of molecules. This relationship permits one to infer the presence of rotational axes of symmetry in the macromolecule. Note, however, that it is not necessary for all rotation axes of a molecule simultaneously to be rotation axes of the crystal. Therefore, the estimate of symmetry is a minimal estimate.

An example is aspartate transcarbamoylase, which was treated in Chapter 2. In one crystal form, this enzyme crystallizes in a space group with eight asymmetric units per cell, but there are only four molecules per cell. This indicates the presence of a twofold rotation axis. In a second crystal form, the space group has six asymmetric units per cell, but the cell dimensions allow for only two molecules per cell. Thus, a threefold rotation axis exists in the molecule. Because each subunit must be an asymmetric object, the only way that both of these axes can exist simultaneously is for the molecule to have six (or some integral multiple of six) subunits of each type. For aspartate transcarbamoylase, the subunit structure is c_6r_6 , and a model of the symmetric arrangement is shown in Figure 2-49.

Varying scattering geometry to measure diffraction pattern

Reciprocal lattice points are precisely those locations in space that satisfy the von Laue conditions for scattering. Whenever the crystal and incident beam (\hat{s}_0) are

oriented so that the scattering vector \mathbf{S} contacts a reciprocal lattice point, diffracted intensity is observed along the vector $\hat{\mathbf{s}} = \lambda \mathbf{S} + \hat{\mathbf{s}}_0$. In making measurements, one has the choice of varying the orientations of the crystal, the detector, or the incident beam. Usually it is the crystal that is allowed to move. The reciprocal lattice is fixed in space for a fixed crystal orientation. If the crystal is rotated through an angle about an axis, the reciprocal lattice will rotate the same angle about the same laboratory axis.

For given x-ray wavelength, crystal orientation, and incident x-ray beam, all possible scattering vectors extend from the origin to the surface of the sphere of reflection (Fig. 13-23a). The sphere can be generated from Figure 13-3a by allowing all possible orientations of \mathbf{S} . It has a diameter of $2/\lambda$ because this is the largest possible value of $|\mathbf{S}|$, occurring at $\theta = 90^\circ$. The surface of the sphere passes through the origin of the reciprocal lattice. Here, $h = k = l = 0$, the scattering vector \mathbf{S} has length zero, and $\theta = 0^\circ$; all radiation is forward scattered.

The sphere of reflection will enclose a set of reciprocal lattice points. However, diffraction will be observed only when these points intersect the surface of the sphere. Clearly, if the reciprocal lattice is literally composed of points, the probability of this occurring is infinitesimal. Fortunately, the actual radiation used in diffraction experiments is a distribution of wavelengths. This means that a spherical zone of \mathbf{S} applies, rather than just a surface. Furthermore, in an actual crystal, zones of unit cells differ very slightly in orientation. This effect, called mosaicism, means that the reciprocal lattice points will be of a finite size. Nevertheless, not many lattice points will intersect the surface of the scattering sphere simultaneously (Fig. 13-23a).

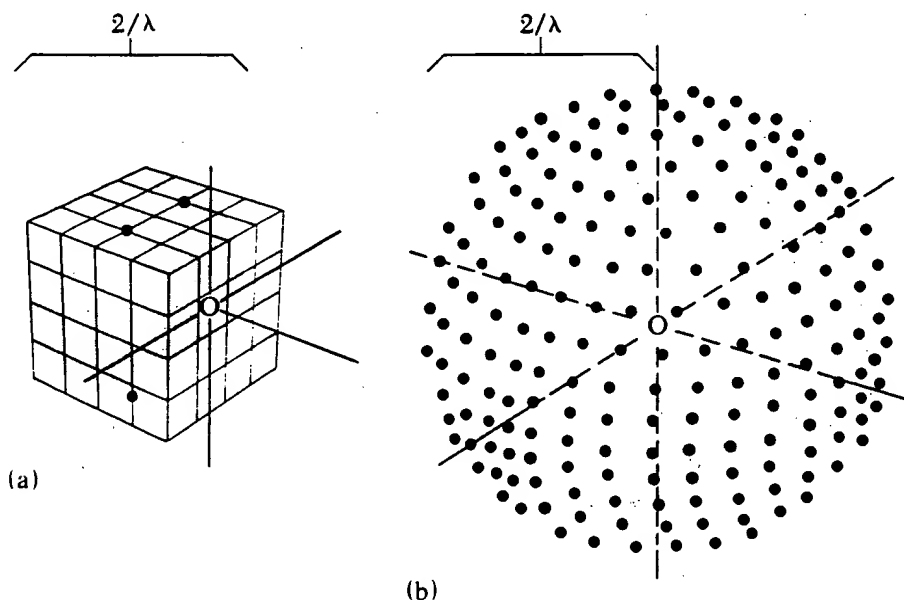


Figure 13-23

Experimental restrictions on the observation of x-ray diffraction. (a) For a fixed geometry and x-ray wavelength, scattering will be observed only when the surface of the sphere of reflection intersects reciprocal-lattice points. (b) Even if all possible geometries are sampled, only that portion of the reciprocal lattice that lies within a sphere of radius $2/\lambda$ (the limiting sphere) can be examined.

To collect sufficient diffraction data to solve a crystal structure, one must measure as many diffracted rays as possible. Therefore, what is usually done is to rotate or oscillate the crystal in a systematic way. This causes successive lattice points to intersect the scattering sphere and permits the resulting diffraction to be measured (Fig. 13-24). Note that it is the discontinuous nature of the reciprocal lattice that makes it difficult to collect diffraction data for a three-dimensional crystal. In a two-dimensional sample, the reciprocal lattice is a set of lines (Fig. 13-12). Most of these will intersect the sphere of reflection somewhere, and so a single sample geometry can yield many diffraction spots (Fig. 13-11).

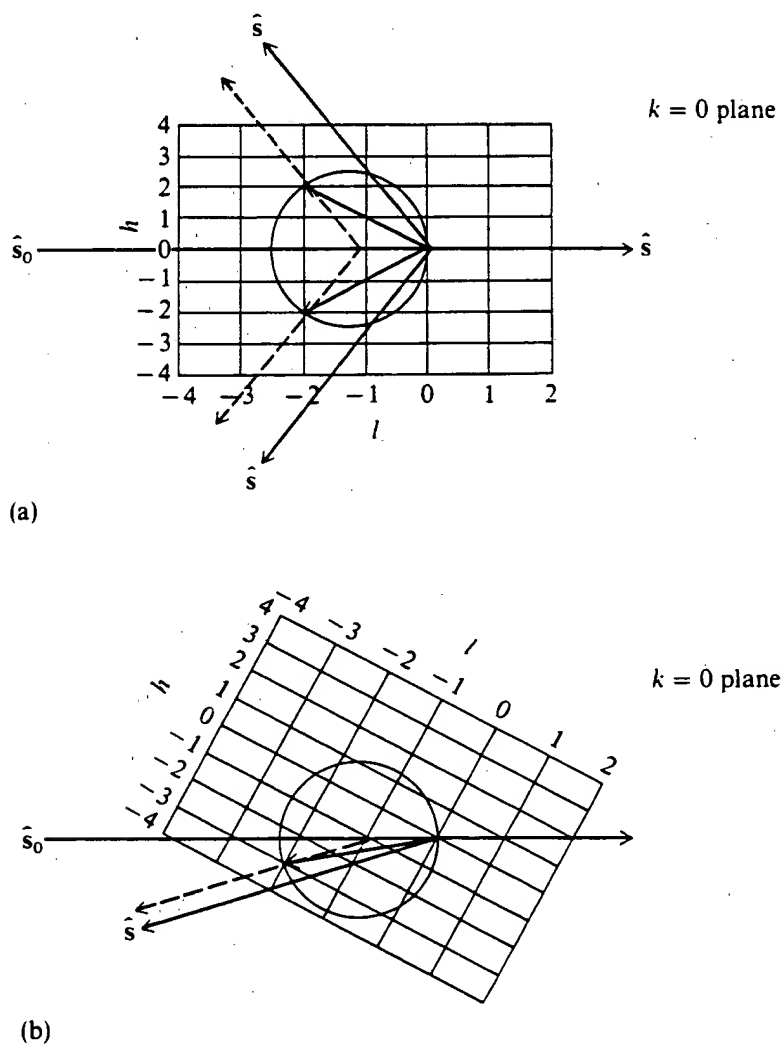


Figure 13-24

The effect on observed diffraction of rotating the sample. (a) One sample orientation where a pair of scattering vectors (black arrows) intersect the reciprocal lattice. Note that, if the scattered radiation (colored arrows) is viewed as originating from the center of the sphere of reflection, \hat{s} intersects the same reciprocal-lattice point as does \hat{S} . (b) An alternative geometry, in which only a single reciprocal-lattice point is sampled.

Several methods for collecting scattering data

The spatial pattern of diffracted rays that emerges as one rotates a crystal is not necessarily a simple one. However, proper choices of rotation axes can lead to fairly regular patterns of diffracted spots. For example, suppose that the incident beam is perpendicular to axis \mathbf{b} , and the crystal is rotated about this axis. In a rotation camera, a cylinder of film surrounds the sample (Fig. 13-25a). Diffracted rays passing through a given k level of the reciprocal lattice (say, $h, 0, l$) will all fall on the same line of the film. However, the order of spots, as a function of h and l values, is not regular, and the overall pattern is quite compressed. A rotation photograph projects a whole layer of the reciprocal lattice onto a single line. A typical example is shown in Figure 13-25b.

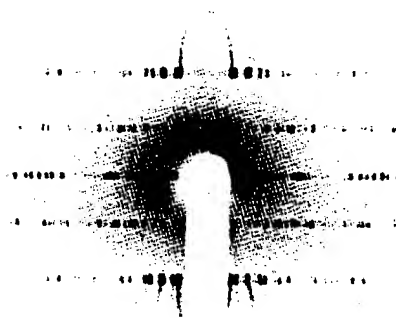
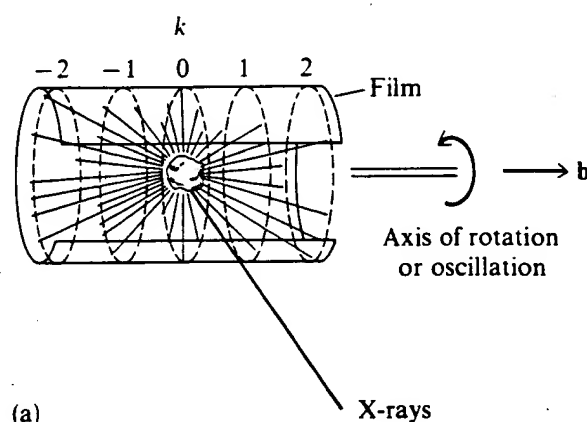


Figure 13-25

*The rotation camera. This camera projects a plane of the reciprocal lattice onto a line of the film. (a) Schematic diagram of a rotation camera. (b) Example of a rotation photograph. [From G. H. Stout and L. M. Jensen, *X-Ray Structure Determination* (New York: Macmillan, 1968).]*

Clearly, what one would like to have is a way of collecting diffraction data organized just like the reciprocal lattice. One way to do this is the precession camera. In essence, this camera rotates the sample and the film in such a coupled way that diffraction spots from all individual lines of the reciprocal lattice appear as properly spaced lines on the photographic film. The details of operation of such a camera are complex, and the interested reader can find them elsewhere. The results are photographs that each show one whole plane of reciprocal space. A set of such photographs permits one to reconstruct all accessible data about the diffraction pattern. Figure 13-26 shows an example. Two-dimensional scanning film densitometers are used to convert the x-ray photograph into a series of indexed integrated scattering intensities.

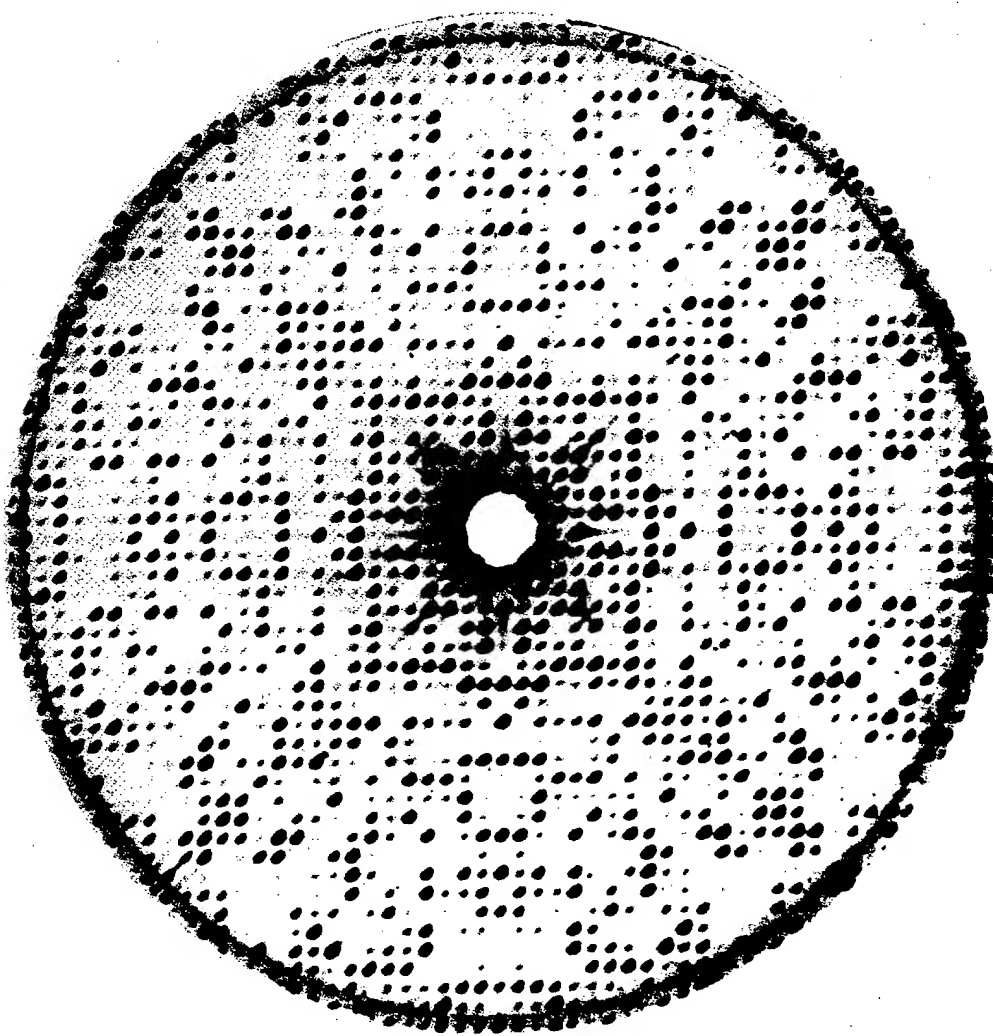


Figure 13-26

A precession photograph. An entire plane of the reciprocal lattice is displayed without distortion. The sample is a tetragonal crystal of lysozyme. Note the presence of a fourfold rotation axis and various mirror-symmetry planes in the diffraction pattern. [Courtesy of C. C. F. Blake.]

An alternative to the precession camera, now in much more common use, is the automated diffractometer. Once the crystal class and unit cell of the sample are known, its absolute orientation in space can be determined. Then, it is possible to predict the sample and detector geometry needed to produce a spot with particular indices h, k, l . This information is given to a computer, which finds the spot, measures the intensity, rotates the sample and detector to where the next spot should be, and so on. The x-ray intensity can be measured directly by solid scintillation detectors.

The limiting sphere of the reciprocal lattice

The reciprocal lattice, in principle, is infinite. Each of the indices h, k, l varies from $-\infty$ to $+\infty$. The Fourier inversion needed to calculate the electron density distribution from x-ray structure factors is an infinite sum over all three indices (Eqn. 13-39). It would not be practical to collect data over an infinite reciprocal lattice. More significantly, it is not even possible, because the finite wavelength of the x rays used limits the largest values of the indices h, k, l that yield diffraction intensity.

Return to Figure 13-23a and note the position of the sphere of reflection. Rotation of the crystal about any of the three laboratory axes will bring reciprocal lattice points into contact with the spherical surface, but cannot possibly reach any reciprocal lattice points that lie a distance farther from the origin than the sphere surface. The longest possible scattering vector has a length $2/\lambda$. Thus, even if all possible geometries are tried, no reciprocal lattice points farther from the origin than $2/\lambda$ can be sampled.

This limitation defines a sphere of radius $2/\lambda$, centered at the origin (Fig. 13-23b). The sphere is precisely twice the diameter of the sphere of reflection. It is called the limiting sphere. All reciprocal lattice points contained within the limiting sphere are measurable by a proper choice of experimental geometry. But no points outside of the limiting sphere can be detected. The only recourse would be to decrease the wavelength of the x rays and thus increase the diameter of the limiting sphere.

Limitations on the resolution of structures calculated from x-ray diffraction data

What is the result of our inability to measure scattering throughout the whole reciprocal space? Larger distances in reciprocal space correspond to smaller distances within the real crystal lattice. Therefore, with only a finite set of diffraction data, the ability to discriminate fine details of the electron density distribution is lost. In short, the resolution of the structure determination is decreased. It is useful to examine this statement more quantitatively.

What fraction of the data within the limiting sphere must be collected in order to produce a final structure determined to a given resolution? A vector \mathbf{S} in reciprocal space is $h\mathbf{a}^* + k\mathbf{b}^* + l\mathbf{c}^*$. Its length is $|\mathbf{S}|$; the dimensions are \AA^{-1} . Therefore, $|\mathbf{S}|$

corresponds to a distance $d = 1/|S|$. One can estimate[§] that a collection of all diffraction data up to a value of $|S|$ ought to contain the information needed to determine a structure with a resolution of around $1/|S|$ Å.

The implications of limited resolution are best seen by a purely theoretical example. Figure 13-27a shows a section of β sheet. For simplicity, we shall view this as projected into the \mathbf{a} - \mathbf{b} plane. (See Box 13-5 for a discussion of how a projection is carried out mathematically.) The unit cell illustrated in Figure 13-27a repeats to form an infinite two-dimensional lattice. The structure factor produced by x-ray scattering from this array can be calculated exactly using the two-dimensional analog of Equation 13-70:

$$F_m(h, k) = \sum_j f_j(S) e^{2\pi i(hx_j + ky_j)} \quad (13-88)$$

The indices h and k can be evaluated for any integral values we want, from $-\infty$ to $+\infty$.

Figure 13-27b shows part of the resulting set of structure factor data. Note that this plot illustrates both the phase and the amplitude of the structure factor. Because the two-stranded β sheet projected into two dimensions has a center of symmetry, the structure factor is real rather than complex, and the phase term reduces to just a sign (+ or -) as described earlier in the chapter.

Given a set of x-ray scattering data such as that shown in Figure 13-27b, we can calculate the structure that produced it by using Equation 13-39. In two dimensions, the result is

$$\rho(x, y) = (1/A) \sum_{h=-\infty}^{\infty} \sum_{k=-\infty}^{\infty} F_m(h, k) e^{-2\pi i(hx + ky)} \quad (13-89)$$

where A is the area of one unit cell. However, in practice, we cannot measure values of $F_m(h, k)$ with h and k extending all the way out to $\pm\infty$. Suppose that $|S|$ could be measured only out to $1/4$ Å⁻¹. This restricts h and k to values that fall within a circle of radius $|S| = |h\mathbf{a}^* + k\mathbf{b}^*|$ drawn about the origin. (This is the innermost circle drawn in Fig. 13-27b.) It restricts h and k to values of -1, 0, and 1. If Equation 13-89 is used with just these terms, it produces an image of the structure at about 4 Å resolution. The result (Fig. 13-27c) suggests two strands of peptide, but obscures all molecular details.

Extending the data set used to larger values of $|S|$ produces higher-resolution images (Fig. 13-27d,e). Note that in these images some regions of negative electron density (dashed contours) are included. These occur because the data set used is still finite. A perfect image of the structure can be obtained only when an infinite data set is available. Because such a set cannot be obtained in practice, corrections are used to compensate for the truncation of the series in Equation 13-89.

[§] From the theory of image formation, if all scattered waves are measured with wavelengths of d Å or more, one should be able to resolve structural features separated by $\geq 0.6d$ Å. In reality, x-ray data are not perfect, and a more realistic estimate is d Å.

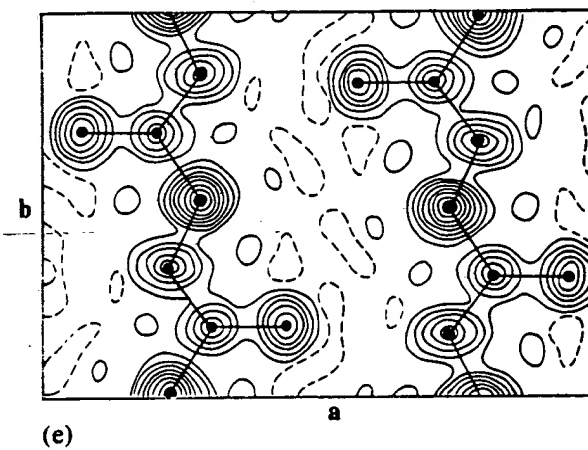
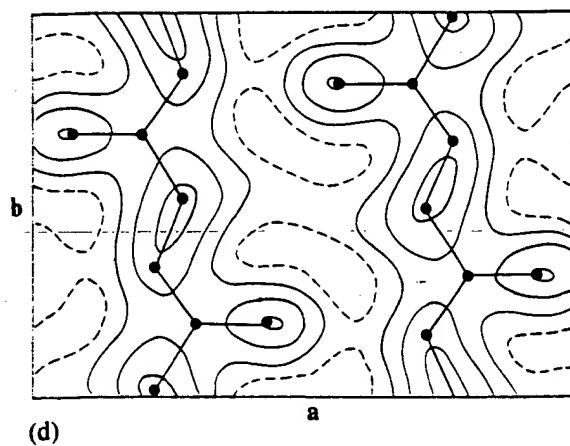
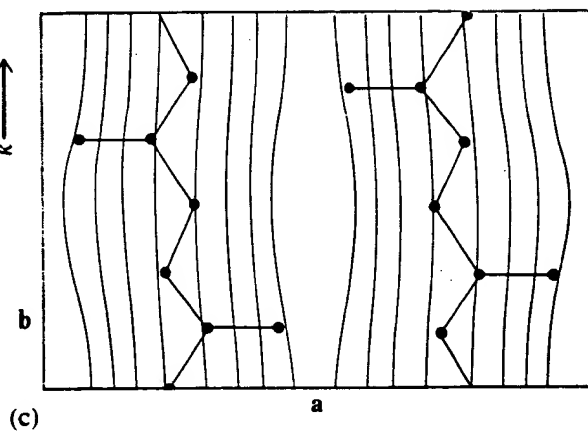
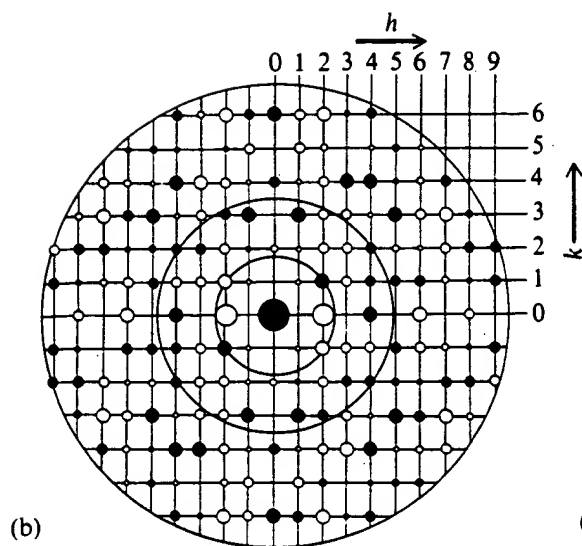
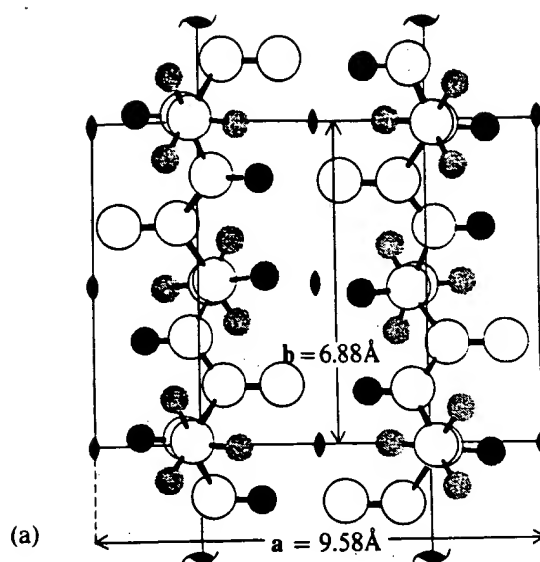


Figure 13-27

Electron density maps as a function of resolution. (a) Two strands of poly-L-alanine antiparallel β sheet within a two-dimensional unit cell. C_2 and 2_1 symmetry axes of a planar projection of the structure are indicated. (b) Calculated structure factor data for a two-dimensional crystal, formed by projecting the structure shown in part a onto the a - b plane. The circles show the data that would be sampled for analysis at resolutions of 4 Å, 2 Å, and 1 Å (indicated by increasingly large circles). The filled dots indicate $F(h, k) > 0$; the open dots indicate $F(h, k) < 0$. The size of each dot is proportional to $|F(h, k)|$. (c) An electron density map at 4 Å resolution, calculated from part b. (d) An electron density map at 2 Å resolution, calculated from part b. (e) An electron density map at 1 Å resolution, calculated from part b. [After R. D. B. Fraser and T. P. McRae, in *Physical Principles and Techniques of Protein Chemistry*, part A, ed. S. J. Leach (New York: Academic Press, 1969).]

Experimental limitations on resolution

The example just discussed illustrates the limitations of reconstructing a structure even if perfect data were available. Experimentally, the wavelength of radiation used limits sampling of the reciprocal lattice to values of $|\mathbf{S}| \leq 2/\lambda$.

Why not always collect data sufficient for structure determination at the highest resolution allowed by this limiting sphere? There are three practical considerations. A given crystal will always have some disorder; thus, the x-ray data corresponding to short distances may be nonexistent. The amount of computation needed to compute the structure rises sharply with the number of data points. And the number of diffraction spots that is equal to the number of reciprocal lattice points contained within a sphere of radius $|\mathbf{S}|$ grows as the volume of the sphere.

The number of reciprocal lattice points within a sphere of radius $|\mathbf{S}|$ is approximately equal to the number n of reciprocal cells contained within the sphere. If V^* is the volume of one reciprocal lattice cell, and $(4/3)\pi|\mathbf{S}|^3$ is the volume of the sphere, then

$$n = (4/3)\pi|\mathbf{S}|^3/V^* = V(4/3)\pi/d^3 \quad (13-90)$$

where V is the volume of the real unit cell, and $d = |\mathbf{S}|^{-1}$ is the resolution. Therefore, the number of diffraction spots that must be measured increases as the cube of the desired resolution.

Two factors decrease the minimal number of diffraction spots or reciprocal lattice points needed to contain all structural information for a certain resolution. As shown in Equation 13-18, the fact that the electron density is real results in a center of symmetry for the diffraction pattern: $F(h, k, l) = F^*(-h, -k, -l)$, where the asterisk indicates the complex conjugate. Thus only one hemisphere of the limiting sphere must be measured. Furthermore, in most crystal classes, there is additional symmetry in the diffraction pattern when plotted in reciprocal space (Table 13-1).

A tetragonal crystal will have a fourfold rotation axis. The diffraction pattern of such a crystal is completely defined by only one octant of reciprocal space. Consider a crystal of cytochrome *c* in the tetragonal class. The unit-cell dimensions are

$a = b = 58.5 \text{ \AA}$ and $c = 42.3 \text{ \AA}$. The unit-cell volume is $abc = 144,700 \text{ \AA}^3$. Equation 13-90 indicates that, for a limiting sphere sufficient to resolve structure to $d \text{ \AA}$, the number of reflections contained is $n = 606,400/d^3$. Because of the tetragonal class, the number of unique diffraction spots is only one-eighth of this: $75,800/d^3$. In

Box 13-5 PROJECTIONS OF ELECTRON DENSITY DISTRIBUTION

Many times it is convenient to work with a projection of the electron density in a plane rather than with the entire three-dimensional electron density distribution. Suppose we choose a plane perpendicular to an arbitrary direction \mathbf{q} . Any vector \mathbf{r} to a given position in the crystal can be expressed as the sum of a component along \mathbf{q} and a component \mathbf{d} perpendicular to \mathbf{q} :

$$\mathbf{r} = \mathbf{d} + q\hat{\mathbf{q}}$$

where $\hat{\mathbf{q}}$ is a unit vector, and q is the magnitude of the projection along \mathbf{q} .

The electron density distribution of the crystal is

$$\rho(\mathbf{r}) = \int_{-\infty}^{\infty} dS F(\mathbf{S}) e^{-2\pi i \mathbf{S} \cdot \mathbf{r}} = \int_{-\infty}^{\infty} dS F(\mathbf{S}) e^{-2\pi i \mathbf{S} \cdot \mathbf{d}} e^{-2\pi i q \mathbf{S} \cdot \hat{\mathbf{q}}}$$

Its projection onto a plane perpendicular to \mathbf{q} is simply the integral of $\rho(\mathbf{r})$ over all q :

$$\rho_q(\mathbf{d}) = \int_{-\infty}^{\infty} dq \int_{-\infty}^{\infty} dS F(\mathbf{S}) e^{-2\pi i \mathbf{S} \cdot \mathbf{d}} e^{-2\pi i q \mathbf{S} \cdot \hat{\mathbf{q}}} = \int_{-\infty}^{\infty} dS F(\mathbf{S}) e^{-2\pi i \mathbf{S} \cdot \mathbf{d}} \int_{-\infty}^{\infty} dq e^{-2\pi i q \mathbf{S} \cdot \hat{\mathbf{q}}}$$

The second integral is just the Dirac delta function, $\delta(\mathbf{S} \cdot \hat{\mathbf{q}})$. Therefore, it vanishes unless $\mathbf{S} \cdot \hat{\mathbf{q}} = 0$ or, in other words, unless \mathbf{S} is in a plane perpendicular to $\hat{\mathbf{q}}$, whereupon the second integral is unity. So, if S_q represents all scattering vectors perpendicular to $\hat{\mathbf{q}}$, then

$$\rho_q(\mathbf{d}) = \int_{-\infty}^{\infty} dS_q F(S_q) e^{-2\pi i S_q \cdot \mathbf{d}} \quad (\text{A})$$

The projection integral is carried out only in a plane of reciprocal space perpendicular to the projection axis. If an inverse Fourier transform is performed,

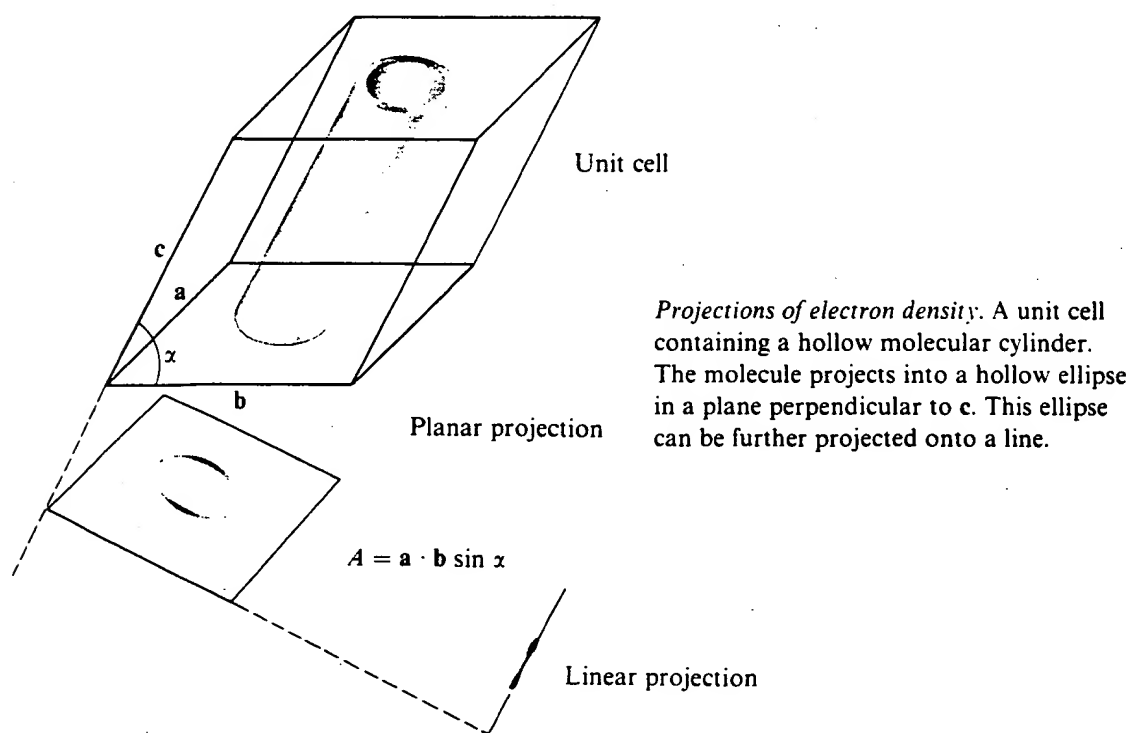
$$F(S_q) = \int_{-\infty}^{\infty} d\mathbf{d} \rho_q(\mathbf{d}) e^{2\pi i S_q \cdot \mathbf{d}} \quad (\text{B})$$

Equations A and B are quite useful. They imply that, if one measures the x-ray scattering in a plane of reciprocal space, $F(S_q)$, the electron density of a projection of the structure onto that plane can be computed. Alternatively, any plane in reciprocal space will contain information only about the electron density of the molecule projected onto a plane. It is common to choose a projection along crystal axes. For example, suppose we choose \mathbf{q} to be the c axis. Then, after inserting the von Laue conditions, Equation A becomes

$$\rho(x, y) = (1/A) \sum_{h=-\infty}^{\infty} \sum_{k=-\infty}^{\infty} F(h, k, 0) e^{-2\pi i(hx + ky)}$$

practice, this implies that, for 4 Å resolution, about 1,200 diffraction spots must be measured. This number increases to 9,500 for 2 Å resolution, and to 75,800 for 1 Å resolution. Clearly, for large unit cells such as those found in macromolecular crystals, the amount of work needed to improve resolution can be quite formidable.

Note that this is the projection of the electron density onto a plane perpendicular to the *c* axis. That plane is not necessarily the *a*–*b* plane unless the crystal symmetry is such that *a* and *b* are perpendicular to *c*. *A* is the area of the projection of the *a*–*b* face of the unit cell perpendicular to the *c* axis, as shown in the figure.



With many molecules, properly chosen projections may have an apparent symmetry not visible in the structure of the whole. Examination of the x-ray diffraction corresponding to such projections often can help simplify the determination of the structure. When crystallographers show diffraction patterns, they virtually always display data for one plane through the reciprocal lattice. Usually, this is a plane in which the index of one reciprocal-cell direction is zero—that is, *h*, *k*, 0 or *h*, 0, *l* or 0, *k*, *l*.

In a comparable way, a row of points of the reciprocal lattice will contain the data needed to calculate the projection of the electron density onto a line. That line will be the intersection of the planes perpendicular to the two projection directions, as shown in the figure. For example, where *a*, *b*, and *c* are all mutually perpendicular, the zero layer line (*h*, 0, 0) describes the projection of the electron density along the *a* axis.

13-4 DETERMINATION OF MOLECULAR STRUCTURE BY X-RAY CRYSTALLOGRAPHY

The phase problem

We have seen that it is relatively easy to determine the properties of a crystal lattice from its measured diffraction pattern. However, the central problem in x-ray crystallography is to determine $\rho(\mathbf{r})$, the electron density distribution within the unit cell. In principle, we solved this problem with Equation 13-39:

$$\rho(x, y, z) = (1/NV) \sum_{h=-\infty}^{\infty} \sum_{k=-\infty}^{\infty} \sum_{l=-\infty}^{\infty} F(h, k, l) e^{-2\pi i(hx + ky + lz)} \quad (13-39)$$

However, an enormous practical deterrent exists. As mentioned earlier (Eqn. 13-12), each $F(h, k, l)$ structure factor is a complex number $|F|e^{i\phi}$, consisting of an amplitude $|F|$ and a phase term $e^{i\phi}$. Only the square of the amplitude, $|F|^2$, can be observed experimentally. The phase angle ϕ can have any value between 0 and 2π .

In the special case of a crystal with a center of symmetry, the phase is much more restricted. For such a crystal $\rho(\mathbf{r}) = \rho(-\mathbf{r})$. As shown earlier, $F(h, k, l)$ is real; the phase can be either 0 or π , and $e^{i\phi}$ is ± 1 . This means that only the sign of each term in the Fourier synthesis of the electron density is unknown. However, even in these cases, there are 2^n possible choices of phase for a set of n diffraction spots.

For biological samples, the inability to measure phases experimentally poses a truly serious problem. Not only is the number of diffraction spots large, but also such crystals cannot have centers of symmetry because they contain asymmetric carbon atoms. Certain techniques we shall describe can help to infer partial phase information. Sometimes chemical insight or other previously known information about the molecule must be included in order to assist the structure determination. The methods usually are sufficient to permit phase estimates accurate enough to compute a three-dimensional structure. It must be borne in mind that occasionally the methods described below can converge on an incorrect structure.

Phases are more important than amplitudes

Because one has measured amplitudes but not phases, it is of interest to ask which of these two factors is most crucial in establishing the correct structure. This can be determined by taking a known structure and calculating the correct structure factors $|F|e^{i\phi}$. If these are then inserted back into Equation 13-90, naturally an accurate image of the electron density distribution appears. This is shown for a two-dimensional projection of a portion of β sheet in Figure 13-27e.

Suppose instead that all the correct amplitudes are used, but each phase ϕ is arbitrarily assigned at the same value, 0° . The resulting Fourier synthesis (Fig. 13-28a) bears no resemblance to a β sheet. Next, suppose all amplitudes are set at the same

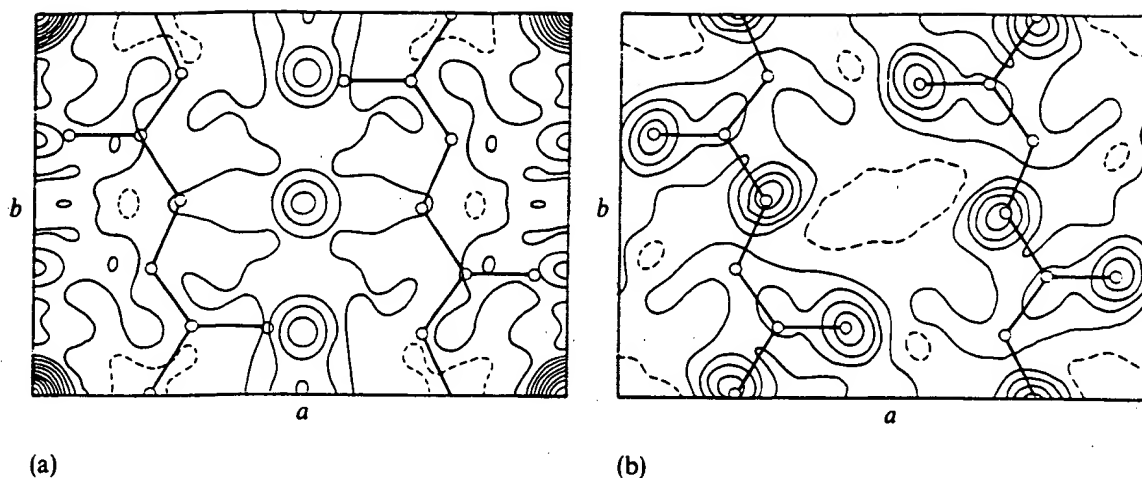


Figure 13-28

*Relative importance of intensities and phases in computing an electron density map from diffraction data. The sample and data are the same as those shown in Figure 13-27. (a) Correct amplitudes were used in this Fourier synthesis, but all phases were set equal to zero. (b) Correct phases were used in this Fourier synthesis, but all amplitudes were set equal to the same average value. [After R. D. B. Fraser and T. P. MacRae, in *Physical Principles and Techniques of Protein Chemistry*, part A, ed. S. J. Leach (New York: Academic Press, 1969).]*

equal value, $|F| = (\sum_k |F_k|^2)^{1/2}$, where the sum is taken over all the square of all of the amplitudes of the diffraction pattern. This corresponds to an average over all measured intensities. If these are combined with the correct phases in a Fourier synthesis, the result (Fig. 13-28b) clearly has substantial resemblance to a β sheet. Thus, we have the unfortunate situation that the unmeasurable quantities are actually more useful than those that can be obtained experimentally.

General considerations in solving a crystal structure

The problem of solving a structure starts with an enormous number of unknowns: the location of each atom in the unit cell, the type of the atom and therefore the expected atomic scattering factor, and the phase associated with each diffraction spot. There is also a considerable amount of available data: the diffraction intensities, the space group and unit cell of the crystal, and usually a significant amount of information about the molecule being examined (for example, partial or complete chemical structure, and perhaps even some conformational data).

The most general goal is to find a structure for the molecule that represents a best fit to the available diffraction data and does not violate, without due cause, our chemical intuition and the set of available structural data. Putting it this way makes it clear that x-ray structure determination is not in practice an absolute technique. In most macromolecular structure cases, one must rely on other information besides diffraction data. That is, there are not enough pure x-ray data available to establish

a unique location and identity for each atom in the structure. Even if all the phases of the scattering factors were experimentally measurable, there might not be enough information. One must marvel, then, at the courage of the first scientists to tackle macromolecular crystal structures.

Steps in determining the structure of a small molecule

Here we illustrate some of the procedures used to determine the structure of a small molecule. These are not necessarily the most powerful methods currently available, but they provide a useful comparison with our later listing of the techniques used on large molecules.

1. One attempts to prepare suitable crystals, and then determines the space group and the unit-cell dimensions, and collects a set of amplitude data $|F_0(h, k, l)|$.
2. One attempts to find the locations of a few of the atoms. This can be done by direct methods (see Blundell and Johnson, 1976), or by a search for a few heavy atoms using the Patterson function discussed later.
3. Once the position of a few atoms is known, the contribution F_H that these atoms make to the total scattering can be calculated by using Equation 13-70:

$$F_H(h, k, l) = \sum_j f_j(s) e^{2\pi i(hx_j + ky_j + lz_j)} \quad (13-91)$$

where the index j runs over all atoms of known position. Note, however, that the structure factor observed experimentally (F_0) is the sum of contributions from the known atoms and from all atoms yet to be found (F_u):

$$F_0(h, k, l) = F_H(h, k, l) + F_u(h, k, l) \quad (13-92)$$

What is crucial, however, is that, because we calculated it, $F_H(h, k, l)$ contains phase as well as amplitude data.

4. The phase of $F_H(h, k, l)$ can be used in several ways to estimate the phase associated with $F_0(h, k, l)$. Then a Fourier synthesis can be performed to compute an estimate of the electron density distribution from the known heavy atom positions:

$$\rho(x, y, z) = \sum_{h=-\infty}^{\infty} \sum_{k=-\infty}^{\infty} \sum_{l=-\infty}^{\infty} |F_0(h, k, l)| e^{i\phi_{hkl}} e^{-2\pi i(hx + ky + lz)} \quad (13-93)$$

Here, the structure factor has been explicitly divided into amplitude and phase terms. Note that it is essential to use *measured* amplitudes. If both calculated phases and amplitudes are used in Equation 13-93 (that is, if Eqn. 13-91 is simply inserted into Eqn. 13-93), all that can come out for $\rho(x, y, z)$ is precisely the known atom positions that were originally put into Equation 13-91 to compute $F_H(h, k, l)$.

5. The electron density distribution calculated by Equation 13-93 with even partial phase information will show some definite maxima corresponding to the locations of new atoms or groups of atoms. These in turn can be used in Equation 13-91 to compute more accurate phases, which then are used in Equation 13-93 to compute a new electron density map. This process, called a Fourier refinement, continues alternately until all atoms consistent with one's original or revised expectations have been found.
6. The structure at this point is still a very approximate one. The original subset of atoms used to start the bootstrap process rolling probably are not placed all that precisely. The electron density distribution that finally results is not always all that sharp. It usually is impossible to assign precise coordinates to all atoms. Furthermore, experimental errors in observed $F(h, k, l)$ affect the data, and these must be dealt with in a systematic way. Thus, the sixth and final phase of x-ray structure determination is to allow the molecular structure to vary somewhat in an attempt to maximize the agreement between the computed structure and the observed data. One way of doing this, called a least-squares refinement, is illustrated later.

In computing $\rho(x, y, z)$ from Equation 13-93 in practice, only a finite set of values of x , y , and z can be used. It is common to compute ρ for planar sections through the crystal (that is, to vary x and y , but leave z constant). Even then, only discrete values of x and y are used. From the resulting pattern of density for each plane, smooth contours are drawn representing areas of equal density. Usually, one interpolates available data to bring this about. Individual two-dimensional sections are produced by a computer. These can be drawn on transparent sheets and stacked up to give a three-dimensional image of the structure. Figure 13-29 shows an example. Alternatively, computer-generated displays can be viewed on a cathode ray tube from any desired perspective.

Calculating the Patterson function from measured scattering

The scattering intensities actually measured in an x-ray diffraction experiment are given by

$$I(\mathbf{S}) = |F(\mathbf{S})|^2 = F(\mathbf{S})F^*(\mathbf{S}) \quad (13-94)$$

where the asterisk indicates the complex conjugate. If we knew $F(\mathbf{S})$, we could

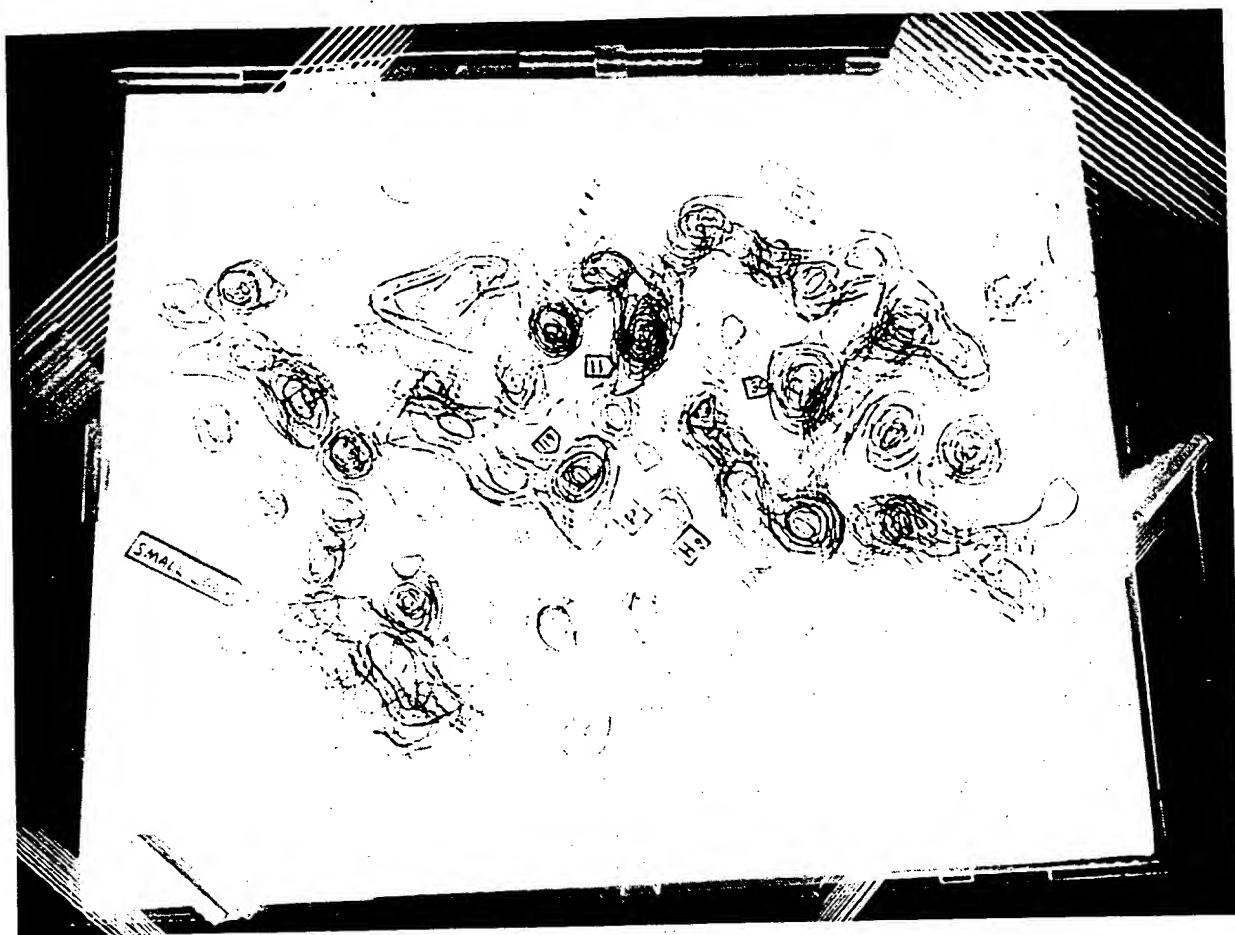


Figure 13-29

A three-dimensional electron density map of ribonuclease S, constructed by plotting density contours on lucite sheets and then stacking the sheets. [Provided by Frederick Richards.]

Fourier-transform it to obtain the electron density distribution of the entire crystal. If instead we Fourier-transform $I(S)$ directly, the result is called the Patterson function:

$$P = \int_{-\infty}^{\infty} I(S) e^{-2\pi i S \cdot r} dS = \int_{-\infty}^{\infty} dS F(S) F^*(S) e^{-2\pi i S \cdot r} \quad (13-95)$$

This equation is the Fourier transform of the product of two functions, $F(S)$ and $F^*(S)$. Therefore (by Eqn. 13-52) it is equal to the convolution of the Fourier transforms of $F(S)$ and $F^*(S)$.

The Fourier transform of $F(S)$ is

$$\int_{-\infty}^{\infty} dS e^{-2\pi i S \cdot r} F(S) = \rho(r) \quad (13-96)$$

(as in Eqn. 13-8). What is the Fourier transform of $F^*(S)$? Because $\rho(r)$ is real, $F^*(S)$ is just (from Eqn. 13-7)

$$F^*(S) = \left(\int_{-\infty}^{\infty} d\mathbf{r} e^{2\pi i \mathbf{S} \cdot \mathbf{r}} \rho(\mathbf{r}) \right)^* = \int_{-\infty}^{\infty} d\mathbf{r} e^{-2\pi i \mathbf{S} \cdot \mathbf{r}} \rho(\mathbf{r}) = \int_{-\infty}^{\infty} d\mathbf{r} e^{2\pi i \mathbf{S} \cdot \mathbf{r}} \rho(-\mathbf{r}) \quad (13-97)$$

Therefore, the Fourier transform of $F^*(S)$, by analogy to what is shown in Equations 13-9 through 13-11, is just $\rho(-\mathbf{r})$. This is the electron density inverted through the origin. Thus

$$P = \widehat{\rho(\mathbf{r})\rho(-\mathbf{r})} = \int_{-\infty}^{\infty} d\mathbf{r} \rho(\mathbf{r}) \rho(\mathbf{u} + \mathbf{r}) \quad (13-98)$$

The physical idea behind the convolution integral helps generate some feeling for the properties of the Patterson function. Figure 13-30 shows a simple case. It is a

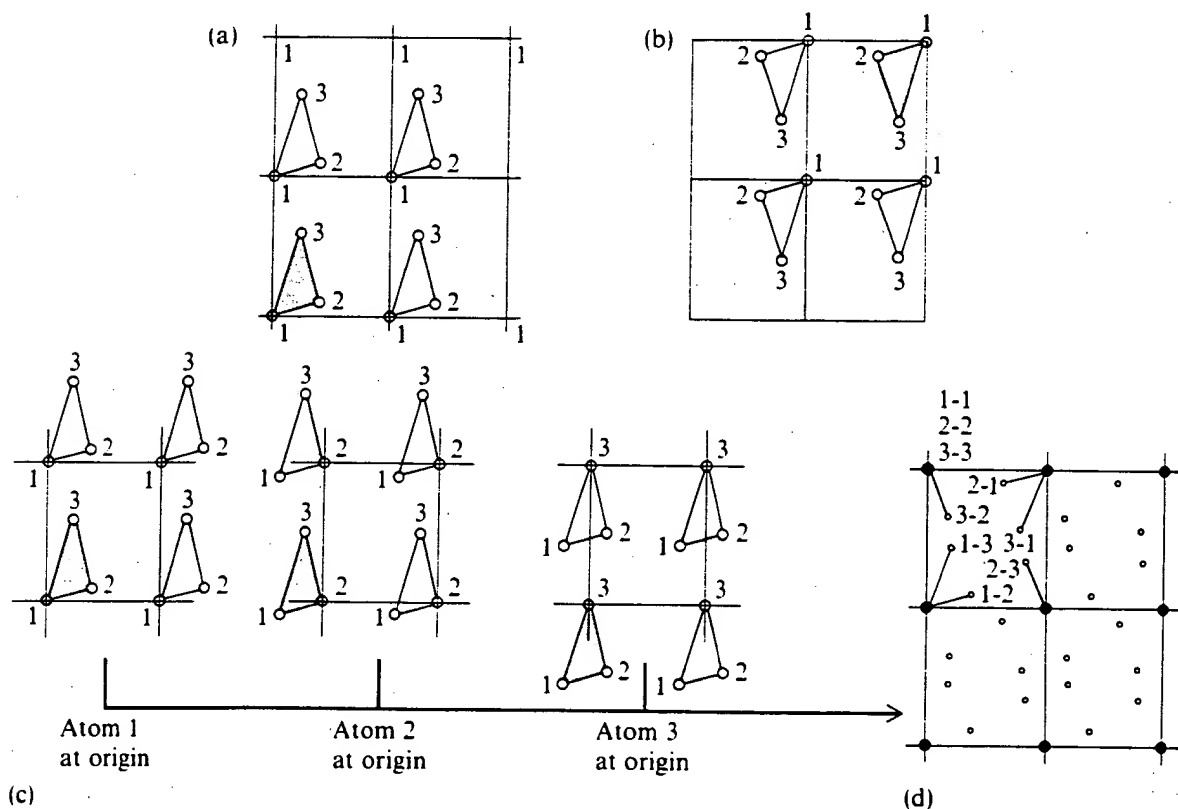


Figure 13-30

The Patterson function for a three-atom structure. (a) Four unit cells of the lattice: the molecule at the origin is shaded.—(b) The same four unit cells, inverted through the origin.—(c) Construction of the convolution of the arrays shown in parts a and b. The position of each atom in part b is used as the origin to lay down an image of the structure in part a. For example, note that, when atom 2 in part b is the origin, atom 1 in part a is displaced from the origin, but atom 2 in part a winds up at the origin. Therefore, an equivalent description of the convolution is simply to lay down successive images of part a with each atom in turn at the origin. (d) The overall convolution, adding the various contributions shown separately in part c. The numbers by each point indicate the way in which that point arose. For example, 1-2 means that an image of atom 2 resulted when the structure was laid down with atom 1 at the origin. [After J. P. Glusker and K. N. Trueblood, *Crystal Structure Analysis: A Primer* (London: Oxford Univ. Press, 1972).]

two-dimensional crystal containing one three-atom molecule per unit cell. Figure 13-30a shows the structure of the crystal, and Figure 13-30b shows the crystal inverted through the origin. We want the convolution of these two structures. First, consider just a single unit cell of the crystal and a single unit cell of the inverted structure. The convolution is formed by choosing each atom in the inverted structure one at a time. Lay down an image of the structure of the original unit cell, by superimposing the origin (lower left corner) of the cell on top of this atom, and weight this image by the electron density of the chosen atom.

Note that, when the origin of the original cell is superimposed on an atom in the inverted structure at $-\mathbf{r}$, the corresponding atom at \mathbf{r} in the original structure now is located at the origin of the inverted cell. Therefore, the convolution can be constructed by ignoring the inverted structure, shifting the contents of a cell to place each atom in turn at the origin, and adding up weighted images of the structure (Fig. 13-30c).

There are three atoms in the structure. The image with each atom at the origin has three atoms. So, a total of nine atom images will appear in each unit cell of the convolution; three fall right at the origin (Fig. 13-30d). In general, for a molecule with N atoms in the unit cell, the Patterson function will have N^2 peaks in its unit cell. N of these peaks will occur at the origin, and the remaining $N(N - 1)$ somewhere within the unit cell. It is clear that the Patterson function will be increasingly cumbersome to use or interpret as N grows.

Periodic repetition of Patterson functions

The convolution described by Equation 13-98 actually is operated over the whole crystal and not over just one unit cell. This fact has a simple consequence. Consider a lattice with only a single atom at each unit cell vertex. If one particular atom is used to superimpose an image of the whole crystal, the result is to place an atom at every vertex of every unit cell. Choosing any other atom results in exactly the same image.

The same argument applies in a molecular crystal. Choose one atom in a particular cell to lay down an image. Choose the corresponding atom in a different unit cell to lay down an image. The resulting images are coincident, except that the crystal is displaced in space by an integral number of unit cells. Thus, like the electron density, the Patterson function repeats periodically throughout the crystal. All the information of interest can be obtained by concentrating on a single unit cell. With actual data, the intensity $I(\mathbf{S})$ is not a continuous function, but is sampled only at the reciprocal lattice points. Thus, by analogy with Equation 13-39, the integral in Equation 13-95 is replaced by a sum:

$$P(x, y, z) = \sum_{h=-\infty}^{\infty} \sum_{k=-\infty}^{\infty} \sum_{l=-\infty}^{\infty} |F(h, k, l)|^2 e^{-2\pi i(hx + ky + lz)} \quad (13-99)$$

Correspondence of peaks in Patterson function and vectors between atoms

An alternative description of the Patterson function helps give a feeling for the structural information it contains. Note first that, if we change the origins used for the unit cells, the resulting Patterson function remains unaltered. That function still is constructed by placing each atom in turn at the origin of a cell. Hence, all of the peaks in the Patterson function must represent internal structural aspects of the unit cell.

Suppose the unit cell has three atoms, located at \mathbf{r}_1 , \mathbf{r}_2 , and \mathbf{r}_3 . When an image is laid down by shifting the atom at \mathbf{r}_1 to the origin, the peaks in the image are placed at $\mathbf{r}_1 - \mathbf{r}_1$, at $\mathbf{r}_2 - \mathbf{r}_1$, and at $\mathbf{r}_3 - \mathbf{r}_1$. Therefore, these peaks in the Patterson function are simply the vectors from each atom in the structure to atom \mathbf{r}_1 . When \mathbf{r}_2 is used as the origin, we get peaks for vectors from all atoms to \mathbf{r}_2 , and so on. So the Patterson function is simply the set of all vectors between pairs of atoms in the structure. It is clear why this set does not depend on the choice of an origin. Using this physical description, the Patterson function can be rewritten as

$$P = \sum_j \sum_k \rho_j \rho_k (\mathbf{r}_j - \mathbf{r}_k) \quad (13-100)$$

where each index j and k is summed over all atoms in the unit cell with electron density ρ .

The Patterson map contains more than enough information to determine the structure. The problem is that there is no efficient or easy strategy to use this information. Unfortunately, the peaks in the Patterson function are not labeled. There is no simple way of deciding which pair of atoms a given vector in the map represents. One must find a way to deconvolute the Patterson function to extract the structure. If just a few atoms are involved, this can easily be done by brute force. Alternatively, if the positions of a few atoms are already known, superposition techniques can be used to deconvolute the Patterson function (see Blundell and Johnson, 1976; Stout and Jensen, 1968).

Using Patterson maps to locate heavy atoms in small molecules

For complex molecules, the difficulty in interpreting the Patterson map is a direct consequence of the large number of interatom vectors. Suppose, however, that the structure contains two or more heavy atoms per unit cell. The atomic scattering factor is proportional to the number z of electrons (Eqn. 13-23). Thus observed intensities, and the resulting Patterson peaks, from atoms i and j are proportional to $z_i z_j$ (corresponding to the $\rho_i \rho_j$ terms in Eqn. 13-100). This means that vectors between

pairs of heavy atoms are the most dominant feature of a Patterson map. With a limited number of heavy atoms, it usually is possible to find out enough about their locations to proceed with further refinement and structural analysis.

Most space groups contain molecules related by symmetry operations within the unit cell. If each molecule has a heavy atom, the Patterson vector between two symmetry-related atoms will fall in an easily identifiable region of the Patterson map. Consider the example shown in Figure 13-31. This is a monoclinic crystal in space

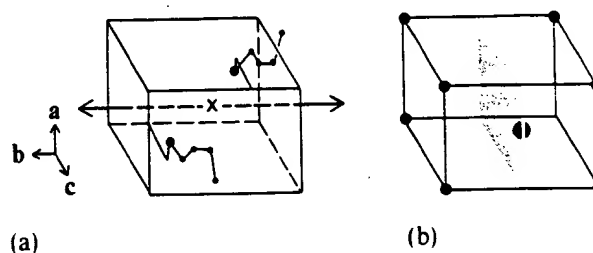


Figure 13-31

Locating heavy atoms. (a) A unit cell of a crystal in space group $P2_1$. There are two molecules per unit cell, with each molecule containing one heavy atom. (b) Patterson function calculated for the sample shown in part a. Only the heavy atom-heavy atom vectors are shown. The Harker section is colored.

group $P2_1$ with two molecules per unit cell. There is a twofold screw axis parallel to direction **b**. If there is a heavy atom at position $x'a + y'b + z'c$, then the other heavy atom must be located at $-x'a + (y' + 1/2)b - z'c$. The heavy atom-heavy atom vector must be located at the position $2x'a + (1/2)b + 2z'c$ in the Patterson map. Thus x' and z' can be determined by looking for a peak in the plane of the Patterson map at $(1/2)b$.

This procedure still leaves y' undetermined. However, for the $P2_1$ space group, the problem is not serious. There is no unique origin along the **b** axis, and therefore y' can be chosen to have any arbitrary value.

Planes or lines where symmetry-related Patterson vectors appear are called Harker sections. If one or more Patterson vectors can be assigned by examining these, it sometimes is possible to use superposition methods to find others. Each Harker section will contain not just the heavy atom-heavy atom vectors, but also all the other vectors related by the same symmetry operation. It will not contain any light atom-heavy atom vectors except for coincidences. The contrast afforded by the heavy-atom pair will be z_h^2 versus z_l^2 for each light-atom pair. This raises the question of how heavy an atom is needed. A general rule of thumb is that $z_h^2 \geq \sum_i z_l^2$, where the sum is taken over all light atoms. For a typical light atom, z_l is 7. Thus a single heavy atom such as mercury with $z_h = 80$ could be found in a structure as large as 130 light atoms. It could not be found in a Patterson map of a typical protein with 1,000 to 10,000 atoms.

Testing agreement between calculated structure and observed data

How can one tell if a calculated structure is in good agreement with the measured x-ray diffraction? The most common measure of the agreement is the residual index R :

$$R = \frac{\sum ||F_o| - |F_{calc}||}{\sum |F_o|} \quad (13-101)$$

where $|F_{calc}|$ represents structure factors computed from the model of the total structure by Equation 13-70. Thus the factor R essentially measures how the observed experimental data $|F_o|$ compare with the data that would be expected for the calculated structure, $|F_{calc}|$.

If the structure is very approximate, it may be simply a random arrangement of atoms of the correct numbers, types, and symmetry within the unit cell. In this case, it has been shown that R will be 0.59 for a space group without a center of symmetry, and 0.83 if a center is present. A very rough rule suggests that $R \cong 0.45$ means that the trial structure is not completely useless; $R \cong 0.35$ means definite convergence on the right track; and $R \cong 0.25$ means that most atoms are correctly placed to within the order of 0.1 Å. Small organic structures often can be refined to $R < 0.05$. Protein R values usually are large at early stages in the structure determination. This is because solvent and thermal motion effects usually are not taken into account until later stages.

Note that an R value of 0.25 actually implies a degree of disagreement between observed and calculated amplitudes that would be considered intolerable in most techniques. It probably is fair to say that the quantity of x-ray data makes up for the lack of quality of individual data points.

13-5 DETERMINING THE STRUCTURE OF A MACROMOLECULE

The method of multiple isomorphous replacements

The methods described earlier for small molecules are not successful with proteins or nucleic acids. These large molecules generally do not contain conveniently placed heavy atoms. Even where such atoms do occur naturally, the complexity of the structure demands different approaches. The steps in a typical macromolecular crystallographic study are the following.

1. One attempts to prepare suitable crystals of the native macromolecule. (This is the most difficult and time-consuming stage in protein or nucleic acid crystallography. In many cases, macromolecular crystals form that appear beautiful morphologically, but they have so much disorder that high-resolution diffraction data are unobtainable.) Using the crystals, one determines the space group and unit-cell dimensions, and then collects a set of scattering amplitude data.

2. One attempts to prepare several different heavy-atom isomorphous derivatives. These are crystals with the same unit cell, space group, and macromolecular structure as the parent crystal, except that one or more heavy atoms have been introduced at specific loci. For each derivative, one collects a new set of scattering amplitude data.
3. One attempts to find the locations of the heavy atoms in the crystal. A popular way to do this is the difference isomorphous Patterson synthesis we shall discuss.
4. One attempts to refine the positions assigned to heavy atoms, either by use of difference Fourier refinement techniques somewhat like those described for small molecules, or by more elaborate methods.
5. By comparing the structure factor data of the parent crystal with the corresponding data of one or more heavy-atom isomorphous derivatives, it is possible to estimate the phases of each $F(h, k, l)$ of the *parent* crystal. In general, the more heavy-atom derivatives available, the more accurate the phase estimates will be.
6. By using the phases estimated for the parent crystal, it often is possible to refine the positions of the heavy atoms further using least-square or difference Fourier techniques. This procedure in turn leads to better estimates for the phases of the parent crystal.
7. Using the estimated phases and observed amplitudes of each $F(h, k, l)$, one calculates an electron density map using Equation 13-93.
8. A model is built of the electron density map. Usually at this state, only low-resolution data (typically 5.5 to 7 Å) have been used, and so the map does not show well-resolved structural details. Then steps 4 through 8 are repeated with data at higher resolution (2.5 to 3 Å) until it is possible to construct a *molecular* model.
9. Sometimes, one attempts to refine the structure. For example, one can calculate phases from the atom positions in the molecular model by Equation 13-70 and use them instead of the phases determined in stages 5 and 6. The refinement can involve Fourier or least-squares techniques, and can treat just the x-ray data or can also include information about known energetics of protein conformation.

----- Most of these stages are discussed in more detail in the following subsections.

Preparation and properties of macromolecular crystals

For crystallographic studies on a macromolecule of 50,000 mol wt, one needs crystals about 0.3 mm in each dimension. To form these, one generally must prepare a super-

saturated solution of the macromolecule and control the rate at which crystal nucleation and growth occur. Solubility can be altered by varying the pH, salt concentration, types of salts present, and temperature of the solution—or by adding organic solvents.

One convenient way to control the rate of change of many of these parameters is dialysis. Another is vapor diffusion. Here a droplet of macromolecular solution is allowed to equilibrate through the vapor phase with a reservoir of solution. If, for example, the reservoir has a higher salt concentration than the sample, the result will be a gradual removal of solvent from the sample. Further details about these and other techniques are given by T. L. Blundell and L. N. Johnson (1976).

Protein and nucleic acid crystals differ from small-molecule crystals in one important aspect. They contain a considerably quantity (typically 50%) of liquid solvent. Cases are known in which protein or nucleic acid crystals are more than two-thirds solvent by weight. A typical crystal has much less solvent than this, but it usually still resembles a two-phase system. A solid phase is composed of individual macromolecules that usually are touching each other in only a few places. In between is a series of open channels filled with solvent. Figure 13-32 shows an example.

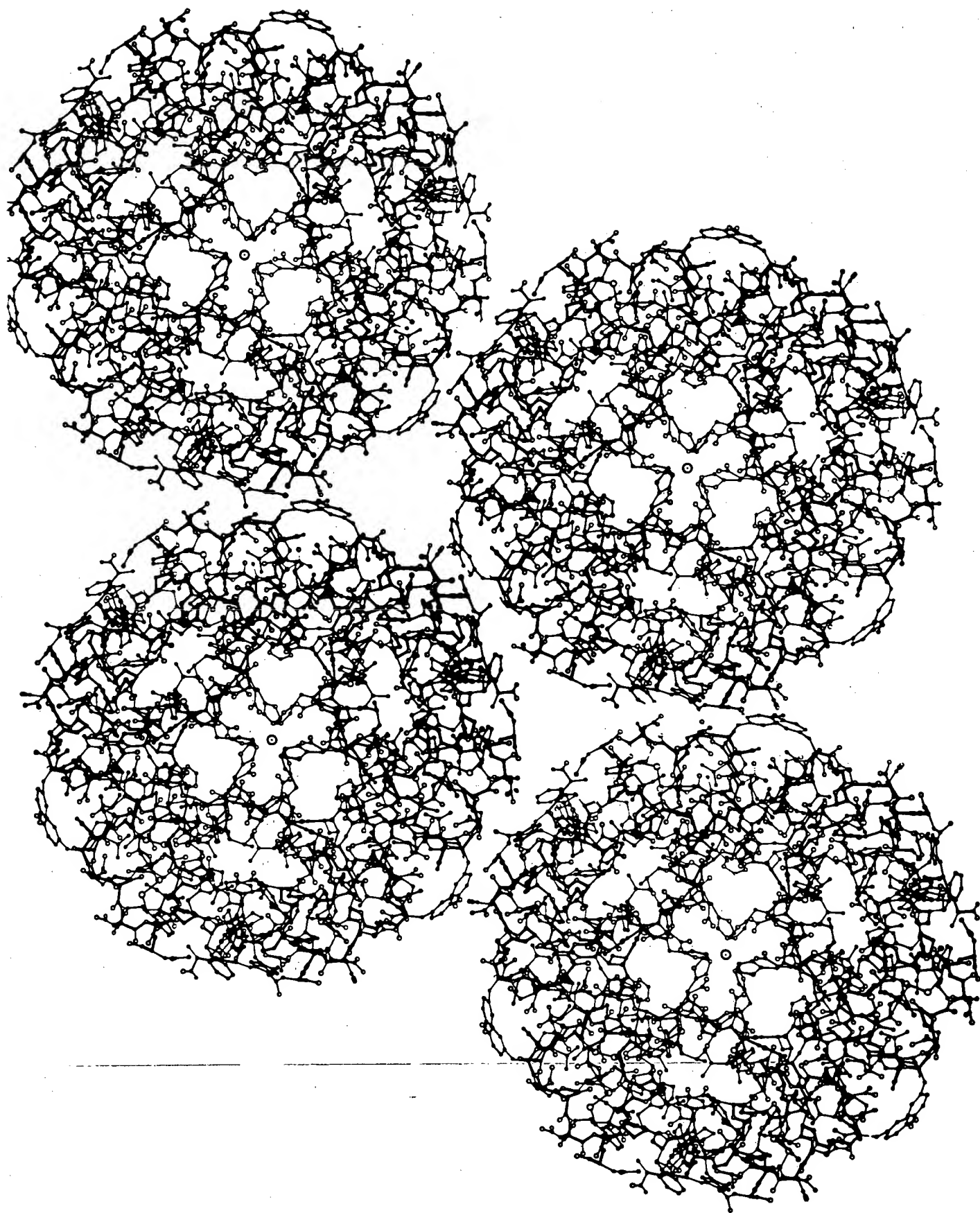
The larger amount of solvent in crystals offers several advantages. It permits small molecules to be diffused into the crystals. As we shall see, this facilitates the incorporation of heavy atoms. It allows substrates or ligands to be introduced into a preformed crystal and thus makes possible the study of the structure of macromolecule–ligand complexes. Indeed, some enzymes actually are quite active in the crystalline state. Finally, the large amount of solvent present makes it likely that the structure determined for the crystalline molecule will closely resemble its structure when free in solution.

One disadvantage arises from the large solvent content. Some of the solvent quite close to the macromolecule is well-ordered. It contributes to the observed x-ray scattering, and it must be taken into account in solving the structure. On the other hand, once this is accomplished, it provides important clues to how macromolecules interact with solvent.

Preparation of isomorphous heavy-atom derivatives

The multiple isomorphous replacement technique has been used to solve almost all protein and nucleic acid structures known to date. It requires a set of three or more crystals of the sample: the parent crystal, and at least two other crystals identical in space group and molecular structure except for the presence of one or more heavy atoms. In general, the heavy atoms either can replace atoms normally present in the structure, or can be additions to the structure. We shall restrict our attention to the latter case because it is somewhat easier to treat mathematically, but ultimately both cases are fairly equivalent.

One approach to preparing an isomorphous derivative would be to attach covalently a heavy metal to the macromolecule in solution, and then to subject it to crystallization conditions. In practice, this approach is not necessarily effective. The factors that promote formation of good crystals are so fickle that frequently even a



small chemical alteration of the structure will either block crystallization or lead to a crystal that no longer is isomorphous. Therefore, almost always one starts with a preformed crystal of nonmodified macromolecule. Reagents containing heavy atoms then are allowed to diffuse in the crystal. This technique provides fair assurance that crystal packing and molecular structure remain largely unaltered. Table 13-2 lists some of the types of reagents used, and Table 13-3 summarizes the results.

Table 13-2
Representative heavy-atom labeling reagents

Reagent	Binding sites
AgNO_3	SH groups
Xe	Noncovalent
$\text{KI} + \text{I}_2$	Tyrosines
PCMB: $\text{Cl}-\text{Hg}-\text{C}_6\text{H}_4-\text{COO}^-$	SH groups
Na_2PtCl_4	Methionines, histidines, and others
$\text{Cl}-\text{Hg}-\text{C}_6\text{H}_4-\text{SO}_2\text{F}$	Active-site serines
$\text{Hg}(\text{Ac})_2$	SH groups, histidines
$\text{UO}_2(\text{NO}_3)_2$ or $\text{UO}_2(\text{Ac})_2$	Carboxyls
Mersalyl: $\text{HO}-\text{Hg}-\text{CH}_2\text{CH}(\text{CH}_3\text{O})-\text{CH}_2-\text{NH}-\text{CO}-\text{C}_6\text{H}_4-\text{O}-\text{CH}_2-\text{COONa}$	Histidines, SH groups

SOURCE: After D. Eisenberg, in *The Enzymes*, 3d ed., vol. 1, ed. P. D. Boyer (New York: Academic Press, 1970).

Figure 13-32

A section through a crystal of insulin. Each wedge-shaped unit is one monomer. These monomers associate into dimers, which in turn aggregate into hexamers. The hexamers pack into the crystal. Note the large solvent channels and the relatively few direct contacts between hexamers. All atoms except hydrogen are shown. [From T. L. Blundell, D. C. Hodgkin, G. G. Dodson, and D. A. Mercola, *Adv. Protein Chem.* 26:279 (1972).]

Table 13-3

Representative protein crystal structures determined with heavy-atom isomorphous derivatives

Protein	Molecular weight	Number of subunits	Space group	Molecules per asymmetric unit	Number of heavy atoms used	Resolution
Metmyoglobin, sperm whale	17,800	1	$P2_1$	1	8	1.4 Å
Oxyhemoglobin, horse	64,500	4	$C2$	1/2	7	2.8 Å
Ferricytochrome <i>c</i> , horse heart	12,400	1	$P4_3$	1	2	2.8 Å
Carboxypeptidase A, beef	34,600	1	$P2_1$	1	5	2.0 Å
α -Chymotrypsin, beef	25,000	1	$P2_1$	2	6	2.0 Å
Papain	23,000	1	$P2_12_12_1$	1	7	2.8 Å
Nuclease, <i>S. aureus</i>	16,800	1	$P4_1$	1	3	2.8 Å
Lactate dehydrogenase, dogfish	135,000	4	$I422$	1/4	5	2.0 Å
Lysozyme, hen egg	14,600	1	$P4_32_12$	1	8	2.0 Å

SOURCE: After D. Eisenberg, in *The Enzymes*, 3d ed., vol. 1, ed. P. D. Boyer (New York: Academic Press, 1970).

Once an isomorphous derivative is available, diffraction data are collected from it and compared with those from the unmodified crystal. The reciprocal lattice dimensions and symmetry should be unaltered, but the observed intensities of some of the reflections can change markedly (Fig. 13-33). These differences can make it possible to estimate the phases of the observed structure factors. However, it first is necessary to locate the heavy atoms; the next few subsections describe this process.

Structure factors for heavy-atom isomorphous derivatives

The electron density distribution of the heavy-atom isomorphous derivative is just the sum of the electron densities of the parent crystal and of the heavy-atom substitutions. Thus the structure factor F_{PH} of the heavy-atom isomorphous derivative must be related to the structure factor F_P of the parent crystal and the structure factor F_H of the heavy atoms along simply by

$$F_{PH}(h, k, l) = F_P(h, k, l) + F_H(h, k, l) \quad (13-102)$$

because the additional scattering in the derivative is due simply to the presence of the heavy atoms.

Note, however, that all three quantities in Equation 13-102 are complex numbers. The significance of this equation can best be seen by expressing each number as a vector in the complex plane as described in Figure 13-4. To add two complex numbers,

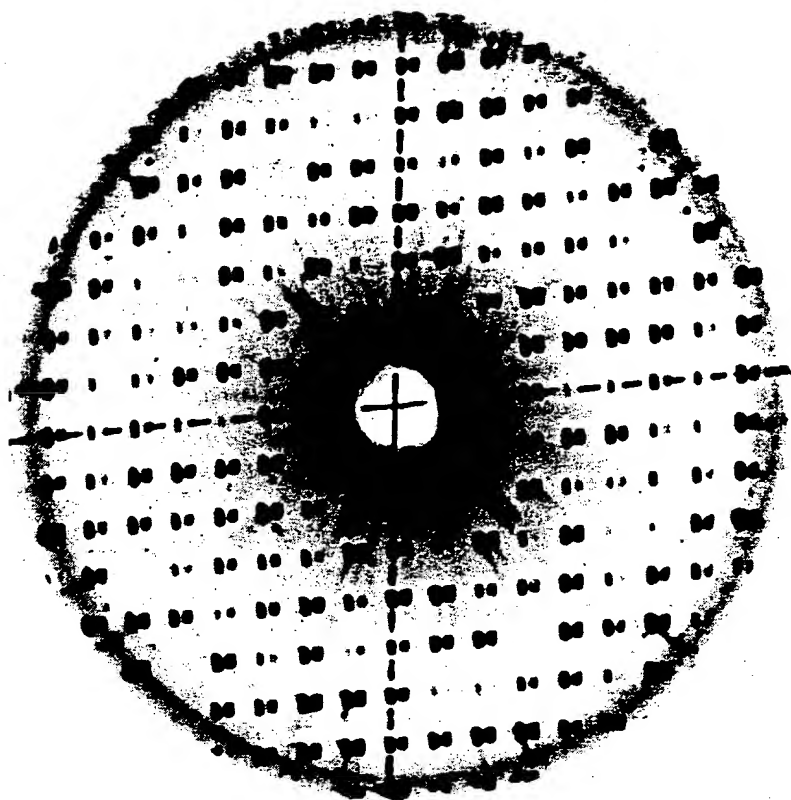


Figure 13-33

Isomorphous replacement. Two precession photographs of triclinic lysozyme crystals are superimposed, slightly out of horizontal register. The left spot of each pair is from a native lysozyme crystal; the right spot is from a crystal after diffusion of HgBr_2 . This is a photograph of the $(0, k, l)$ plane of the reciprocal lattice. Note the differences in intensities. [From R. Dickerson, in *The Proteins*, 2d ed., vol. 2, ed. H. Neurath (New York: Academic Press, 1964).]

one simply adds the real and imaginary components separately. Therefore, represented as vectors, two complex numbers combine just as vectors do, component by component. The result is still a vector in the complex plane, as illustrated in Figure 13-34. One such vector equation holds for each value h, k, l of the structure factors.

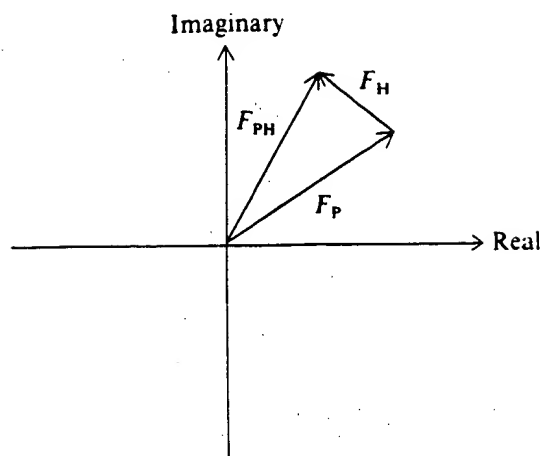
If any two of the vectors shown in Figure 13-34 are known, the third can be calculated unambiguously. The principle obstacle in macromolecular crystallography is that only the *lengths* of two of the vectors, $|F_P|$ and $|F_{PH}|$, are directly measureable experimentally.

Location of heavy atoms by a difference Patterson map

An ordinary Patterson map (Eqn. 13-95) cannot be used to locate the heavy atoms in a macromolecular crystal. We showed earlier that the contrast between heavy

Figure 13-34

Structure factors plotted in the complex plane, for a parent-crystal diffraction spot, a heavy-atom isomorphous addition, and the expected derivative diffraction spot.



atom-heavy atom vectors and other vectors will be insufficient. However, when both an isomorphous heavy-atom derivative and a parent crystal are available, it is possible to calculate a difference isomorphous Patterson map between them, using the measured structure factor amplitudes $|F_{PH}(h, k, l)|$ and $|F_P(h, k, l)|$.

A true Patterson map of just heavy-atom vectors would be given by Equation 13-95 as

$$P_H = (1/V) \sum_{h=-\infty}^{\infty} \sum_{k=-\infty}^{\infty} \sum_{l=-\infty}^{\infty} |F_H(h, k, l)|^2 e^{-2\pi i(hx + ky + lz)} \quad (13-103)$$

we cannot calculate this map directly because $|F_H(h, k, l)|$ is not experimentally measurable. However, it turns out that $|F_H|$ often can be approximated fairly well by

$$|F_H| = ||F_{PH}| - |F_P|| \quad (13-104)$$

Thus we can calculate an estimate of $|F_H|$ from the measured amplitudes of the crystal and a heavy-atom isomorphous derivative. Then an isomorphous difference Patterson function ΔP is calculated:

$$\Delta P = (1/V) \sum_{h=-\infty}^{\infty} \sum_{k=-\infty}^{\infty} \sum_{l=-\infty}^{\infty} ||F_{PH}| - |F_P||^2 e^{-2\pi i(hx + ky + lz)} \quad (13-105)$$

In an ideal case, it can be shown that this function will display the heavy atom-heavy atom vector at one-half the expected intensity plus some contaminating noise due to light atom-light atom vectors (see Blundell and Johnson, 1976).

The accuracy and usefulness of Equation 13-105 depend on the validity of Equation 13-104. This in turn depends on relative phases and amplitudes of the three structure factors involved. We discuss a particular simplified case in the following subsection. Here, note the following observation. When the two vectors F_{PH} and F_P

in Equation 13-102 are parallel, then the phases cancel, and Equation 13-104 is exact. As long as the three vectors are near-parallel, Equation 13-104 should be an excellent approximation. The largest values of $||F_{PH}| - |F_P||$ will tend to be those that arise when F_{PH} and F_P are parallel. Thus, conveniently, the largest terms that enter Equation 13-104 will be those most likely to contain good estimates of $|F_H|$. By selectively including only the large terms in Equation 13-105, we often can produce an improved heavy-atom difference Patterson map. From the heavy atom-heavy atom vectors, we can attempt to find the actual heavy-atom locations by the methods described in Box 13-6.

If Equation 13-104 is to be useful, the presence of the heavy atom in the isomorphous derivative must cause a change in scattering intensity sufficient to yield measurable differences between $|F_{PH}|$ and $|F_P|$. For example, a single mercury atom with 80 electrons will produce an average change of 30% between $|F_P|$ and $|F_{PH}|$ in a 40,000 d protein. Thus, it is more than sufficient for the calculation of a difference Patterson map.

Using centrosymmetric projections to locate heavy atoms

A crystal of biological material cannot contain a center of symmetry because the molecules contain asymmetric carbon atoms. However, it frequently is possible to calculate a centrosymmetric projection (Box 13-5). For example, if a structure has a twofold screw or rotation axis, projection onto a plane perpendicular to this axis will result in a center of symmetry. In this two-dimensional projection, the phases of the structure factor must be either 0 or π , so that all structure factors are either parallel or antiparallel vectors. This greatly simplifies the use of Equation 13-102.

In a centrosymmetric projection, the structure factors for the parent crystal, heavy-atom isomorphous derivatives, and heavy atoms must be related by one of the arrangements shown in Figure 13-35. So long as F_{PH} and F_P point in the same direction, it is apparent that $|F_H| = ||F_{PH}| - |F_P||$, which allows $|F_H|$ to be calculated directly from experimental data. Only in those cases where $|F_H|$ is much larger than $|F_P|$ does Equation 13-104 become incorrect. These cases, which are called *crossovers*, are very rare and do not seriously compromise most heavy-atom isomorphous difference Patterson projections.

Figure 13-36 shows an example of three difference Patterson projections obtained for heavy-atom derivatives of cytochrome *c*. These were obtained by using Equation 13-105. The two relatively simple maps (Fig. 13-36a,b) result from a Pt and a Hg derivative. The more complex map (Fig. 13-36c) was obtained from a crystal into which both metals had been substituted. This map shows Hg-Pt vectors as well as Hg-Hg and Pt-Pt vectors. From these maps, estimates of both the Pt and Hg coordinates can be obtained (see Box 13-6).

In some cases, the heavy-atom positions found from a difference Patterson map are used directly to determine preliminary protein phases, as shown in the next subsection. In most cases, they must be refined first. (Refinement techniques are discussed in subsequent subsections.)

Structure factors	Signs		Measured amplitude change
	F_P	F_H	$\Delta F = F_{PH} - F_P $
	+	+	+
	+	-	-
	+	-	-
	+	-	+
	-	-	+
	-	+	-
	-	+	-
	-	+	+

Figure 13-35

Structure factors in a centrosymmetric projection. Shown as vectors are all of the possible arrangements of parent (P), heavy atom alone (H), and isomorphous derivative (PH) structure factors. A vector pointing from left to right is assigned a positive sign (zero phase angle).

Using heavy-atom positions to estimate phases of the structure factor

From the coordinates and identity of each known heavy atom, we can compute both the phase and amplitude of its contribution to the structure factor, using Equation 13-70. This computation yields F_H . The structure factor of a heavy-atom isomorphous derivative, F_{PH} , must be related to that of the parent crystal, F_P , and to F_H simply by Equation 13-102.

Once the heavy atom is found, F_H is known completely. However, only the amplitudes $|F_{PH}|$ and $|F_P|$ can be measured. Using all three quantities, it is possible to restrict the phase of F_P to only two possibilities (Fig. 13-37a). The possible values of F_P lie on a circle of radius $|F_P|$ centered at the origin. Possible values for F_{PH} will lie on a circle of radius $|F_{PH}|$ but, to satisfy Equation 13-102, the center of this circle must be displaced from the origin by the known vector F_H . Then the two circles intersect at two points. At each intersection, corresponding to phases of ϕ_a and ϕ_b , the conditions prescribed by Equation 13-102 are met.

The most common resolution of the remaining uncertainty in phase is to use a second isomorphous heavy-atom derivative. One estimates the position of the heavy

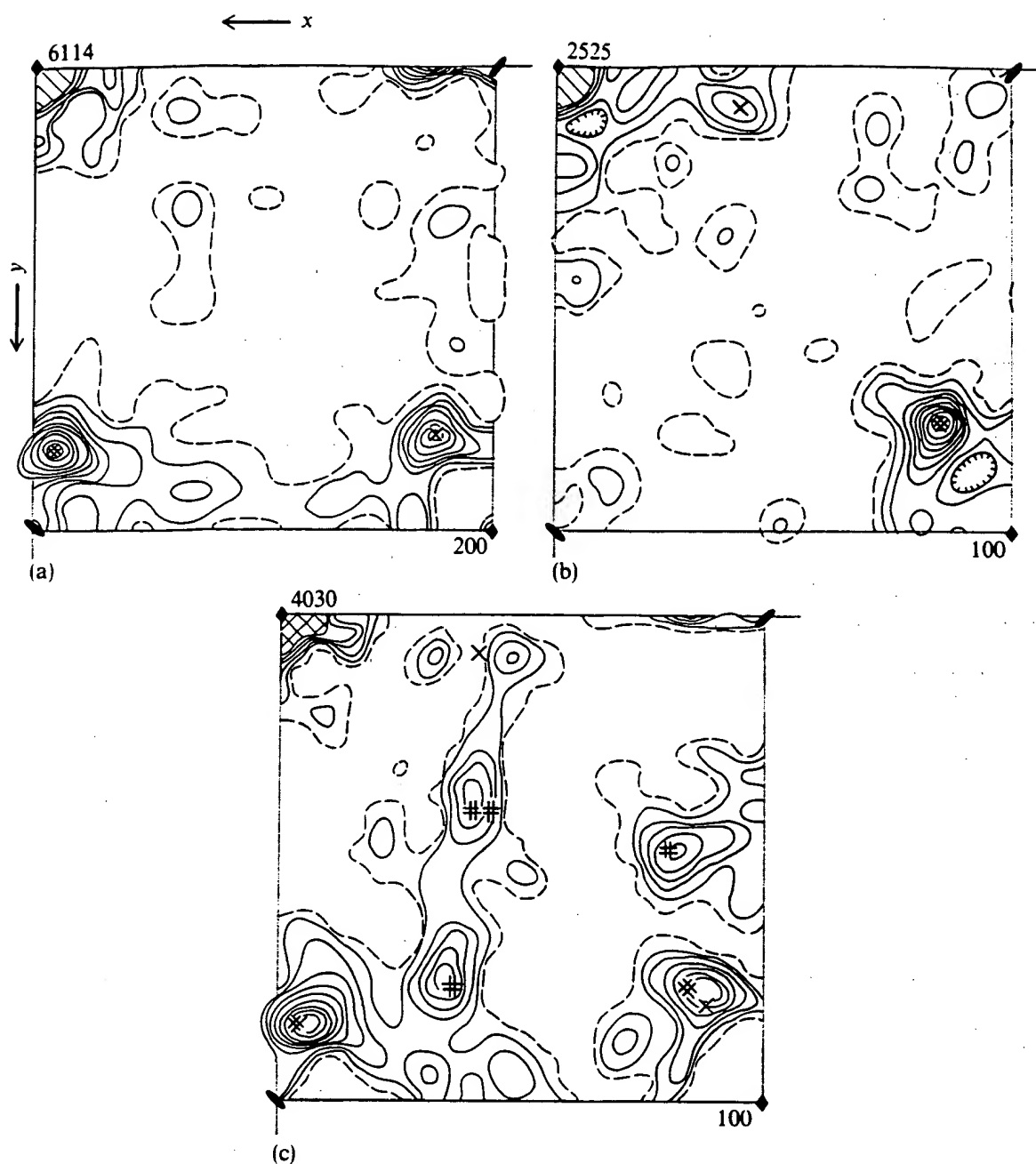


Figure 13-36

Difference Patterson maps, calculated for projections of crystals of cytochrome *c* into the x - y plane. The origin is at the upper left of each map. All maps are drawn to the same scale; contour intervals are marked at the lower right-hand corners; the height of the peak at the origin is indicated at the upper left-hand corners. The zero contours are dashed. The x and y coordinates are indicated; they run only from the origin to one-half the unit-cell dimensions. Single-weight Patterson peaks are shown by X , double-weight Patterson peaks by $*$. (a) A platinum derivative. (b) A mercury derivative. (c) A derivative containing both heavy metals; platinum-mercury cross-vectors are shown by $\#$. [From R. E. Dickerson et al., *J. Mol. Biol.* 29:77 (1967).]

atoms, computes F_H , then uses the analog of Equation 13-102: $F_{PH} = F_P + F_H$. The process of selecting a phase for F_P is repeated again by comparing $|F_{PH}|$ and $|F_P|$, using the known F_H (Fig. 13-37b). In an ideal case, one of the two circle intersections will correspond either to ϕ_a or to ϕ_b , and the other will be some different value ϕ_c .

Box 13-6 AN EXAMPLE OF THE INTERPRETATION OF A DIFFERENCE PATTERSON PROJECTION

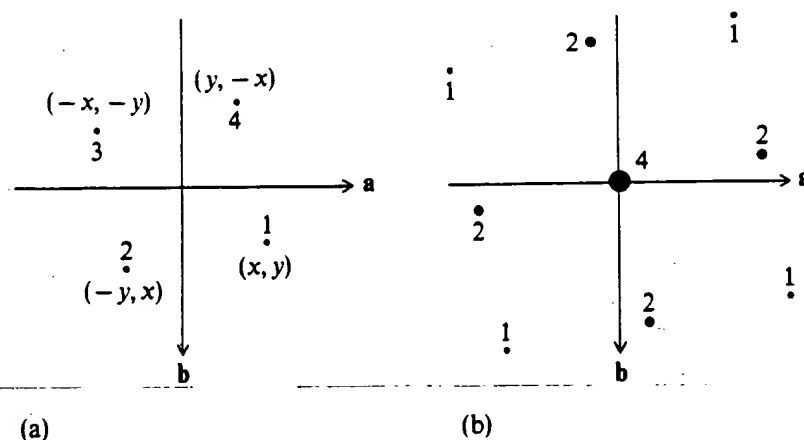
The difference Patterson map shown in Figure 13-36a was calculated for a projection into a plane perpendicular to the c axis of a tetragonal crystal of cytochrome c ($a = b = 58.45$ Å; $c = 42.34$ Å):

$$\Delta P(x, y) = (1/A) \sum_{h=-\infty}^{\infty} \sum_{k=-\infty}^{\infty} [|F_{PH}(h, k, 0)| - |F_P(h, k, 0)|]^2 e^{-2\pi i(hx + ky)}$$

where $|F_{PH}|$ and $|F_P|$ are the square roots of the measured intensities of the heavy-atom isomorphous Pt derivative and the parent crystal, respectively. Thus, $\Delta P(x, y)$ can be calculated from data collected for a single layer of the reciprocal lattice.

The space group of these crystals is $P4_1$. The asymmetric unit is one molecule of cytochrome c . There are four molecules per unit cell, and these are related by a fourfold screw axis. The projection of the structure perpendicular to the c axis places all four molecules in the a - b plane, where they are now related by a fourfold rotation axis. Because of this axis, the two-dimensional structure also has a center of symmetry.

We can use the symmetry to predict what the difference Patterson map should look like for a single heavy atom located at identical positions on each of the four molecules. For



Thus, because F_p can have only one phase, it must uniquely be the angle derived in common from the two isomorphous derivatives.

In real life, the experimental data are not perfect; nor can the heavy atoms be located precisely. Therefore, the points of intersection of circles drawn from two

convenience, we choose the origin of the coordinate system right at the fourfold axis. Then, if the position of one heavy atom is $xa + yb$, the others must be located as shown in part a of the figure. The corresponding heavy atom-heavy atom vectors will be

$$\begin{array}{ll} \mathbf{r}_{12} = (x + y, y - x) & \mathbf{r}_{21} = (-x - y, x - y) \\ \mathbf{r}_{13} = (2x, 2y) & \mathbf{r}_{31} = (-2x, -2y) \\ \mathbf{r}_{14} = (x - y, x + y) & \mathbf{r}_{41} = (y - x, -x - y) \\ \mathbf{r}_{23} = (x - y, x + y) & \mathbf{r}_{32} = (y - x, -x - y) \\ \mathbf{r}_{24} = (-2y, 2x) & \mathbf{r}_{42} = (2y, -2x) \\ \mathbf{r}_{34} = (-x - y, x - y) & \mathbf{r}_{43} = (x + y, y - x) \end{array}$$

plus four heavy-atom self-vectors, which will lie at the origin.

The resulting difference Patterson map will be that shown in part b of the figure (for the relative values of x and y shown in part a of the figure), where the number adjacent to each peak gives its relative weight. Notice that the map has the same fourfold rotational symmetry as the structure that generated it. Concentrate just on the quadrant at lower right, and compare the result with Figure 13-36a. Notice the doubly-weighted peak near the vertical axis. This peak must correspond to the nearly vertical vector that forms two sides of the square of heavy atoms in the structure. The singly-weighted peak (near the lower right of Fig. 13-36a) is produced from a diagonal of the square. The hint of a peak near the horizontal axis arises from the nearby doubly-weighted vector in the upper right-hand quadrant of the map. Thus, a square structure of heavy atoms is fully consistent with the observed difference Patterson map. Once the vectors have been assigned, their locations yield the values of x and y , and thus the actual heavy-atom positions.

It would be a useful exercise for the reader to interpret the Hg difference map in Figure 13-36b and then, using the results of both maps, to attempt to explain the results shown in Figure 13-36c for the Hg, Pt double derivative.

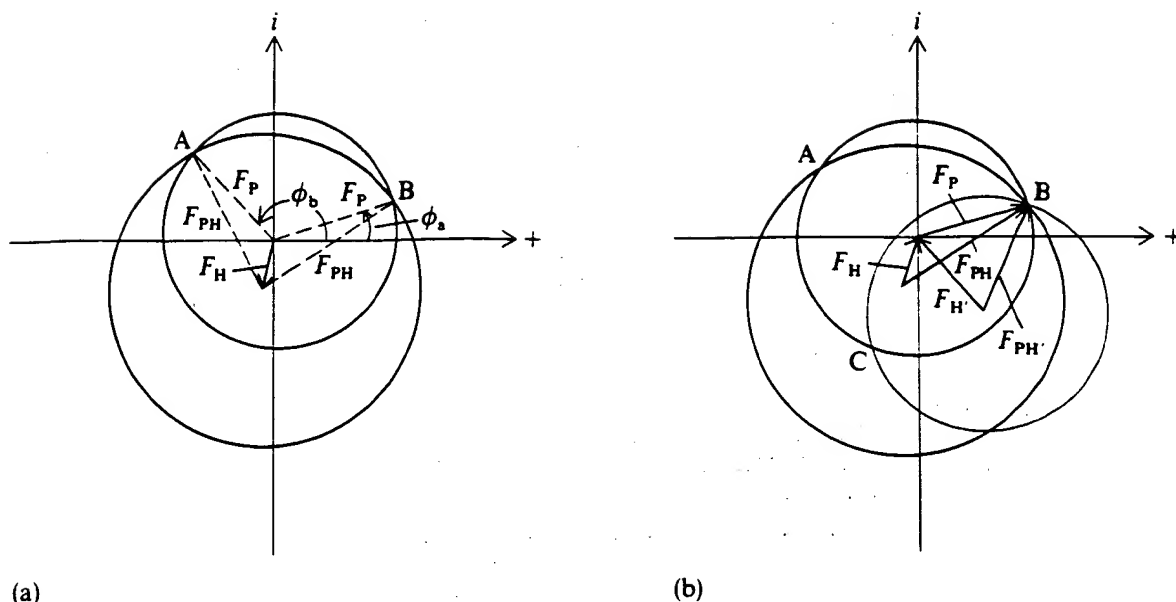


Figure 13-37

Phase determination by isomorphous replacement. Structure factors are plotted in the complex plane, as in Figure 13-34. (a) A single heavy-atom derivative. The circle with radius F_P represents the parent crystal, with measured intensity and unknown phase. The circle with radius F_{PH} represents the isomorphous heavy-atom-containing crystal, with measured intensity and unknown phase. The vector F_H is calculated from the heavy-atom position that had been determined from a difference Patterson synthesis. Because F_H is calculated, both its phase and its amplitude are known. Equation 13-102 will be satisfied by F_P , F_H , and F_{PH} when F_P lies at the origin, but F_{PH} is located at the end of F_H as shown. Therefore, the two circles are displaced, and they intersect at two positions: A and B. These positions define two possible values for the phase of F_P : ϕ_a and ϕ_b . (b) Inclusion of a second heavy-atom derivative. Its scattering amplitude yields a circle (colored) of radius F_{PH}' centered at the end of the vector F_H' , which is calculated from the known position of the heavy atom. This circle also intersects F_P circle at two places: B and C. Because one intersection (B) is the same as an intersection found with the first heavy atom, the only phase choice for F_P consistent with both derivatives is ϕ_b . [After D. Eisenberg, in *The Enzymes*, 3rd ed., vol. 1, ed. P. D. Boyer (New York: Academic Press, 1970), p. 1.]

different isomorphous derivatives may not coincide exactly. Then, to resolve ambiguities, it usually is desirable to have additional derivatives to strengthen the accuracy of phase assignment and to guard against apparent agreement that is accidental. Naturally, the more derivatives available, the more accurately the phase angles are likely to be chosen. Statistical procedures for choosing the best phase estimates from multiple isomorphous derivatives are described by Blundell and Johnson (1976).

Once estimates of the phases of F_P are available, one can use Equation 13-93 to calculate an electron density map of the macromolecule by inserting the measured amplitudes $|F_P(h, k, l)|$ and calculated phases ϕ_{hkl} . However, in most cases, this map will not be very accurate unless the estimates of the heavy-atom positions are first refined.

Phase estimates with a center of symmetry

Suppose one can prepare only a single isomorphous derivative. The prognosis is not completely hopeless. In many cases, a projection of the crystal onto a plane will have a center of symmetry. The advantages of centrosymmetric projections in calculating the *amplitude* of F_H were described earlier. Here we show how such projections also assist the calculation of the *phase* of F_P . Note that only a single layer of reciprocal space is needed to compute the projections, so the structure problem now is purely two-dimensional.

Whenever a center of symmetry exists, the resulting phases can be only 0 or π , and so the only uncertainty remaining for F_P is the sign. The measured change in amplitude of one diffraction spot due to a heavy-atom isomorphous substitution is

$$\Delta F = |F_{PH}| - |F_P| \quad (13-106)$$

All the possible arrangements of F_{PH} , F_P , and F_H are shown in Figure 13-35. When the sign of ΔF (measured) is compared with the sign of F_H (calculated from the known heavy-atom positions), an interesting generalization emerges. Except for two of the rare crossover cases, whenever the sign of ΔF is the same as the sign of F_H , the sign of F_P must be positive ($\phi = 0$). Whenever ΔF and F_H have opposite signs, F_P is negative ($\phi = \pi$).

Thus, even with only a single isomorphous derivative, nearly all of the phases of a centrosymmetric projection of a structure can be computed correctly. Then the electron density of the projection, $\rho(x, y)$ can be calculated by a Fourier synthesis exactly analogous to Equation 13-93. X-ray crystallographers frequently use projections because they can be calculated at earlier stages in the analysis, and because less computer time is required to do two-dimensional sums than to do three-dimensional ones. However, bear in mind that a projection does not uniquely define the three-dimensional structure that produced it.

Narrowing heavy-atom positions with parent-crystal phase estimates

If we knew the phases of each of the diffraction spots of a parent crystal and of a heavy-atom isomorphous derivative, we could calculate an electron density map of each by using Equation 13-39. However, sometimes it is useful to display just the locations of the heavy atoms. This can be done using a difference Fourier synthesis:

$$\begin{aligned} \Delta\rho(x, y, z) &= \rho_{PH} - \rho_P \\ &= (1/V) \sum_{h=-\infty}^{\infty} \sum_{k=-\infty}^{\infty} \sum_{l=-\infty}^{\infty} \\ &\quad \times [|F_{PH}(h, k, l)| e^{i\phi_{PH}(h, k, l)} - |F_P(h, k, l)| e^{i\phi_P(h, k, l)}] e^{-2\pi i(hx + ky + lz)} \quad (13-107) \end{aligned}$$

Here each structure factor has been explicitly shown as a phase plus an amplitude. The amplitudes, $|F_{PH}|$ and $|F_P|$, are measured. The phases of the parent crystal, ϕ_P , are estimated as shown in the preceding sections and are used for *both* amplitudes.

In principle, we could in similar fashion estimate the phases of the derivative, ϕ_{PH} , and use these in Equation 13-107; however, this would lead to problems. Fourier syntheses are dominated by phases, not by amplitudes (Fig. 13-28). Calculated phases of the derivative would contain a heavily weighted contribution from the heavy atoms. The resulting Fourier synthesis would simply give back the same heavy-atom positions one started with, and nothing would have been accomplished. Even the estimates of the parent-crystal phases, ϕ_P , are heavily contaminated with the heavy-atom phases.

In practice, when several heavy-atom derivatives are available, it is best to use parent phases estimated from one or more derivatives to compute the difference Fourier to find other derivatives; these are called cross-phase difference Fourier. Figure 13-38 shows an example for the same cytochrome *c* derivatives discussed earlier. The Pt and Hg atoms show up clearly above a weak background. However, their apparent positions are not yet the true positions in the crystal.

A least-squares refinement of a structural model

There are adjustable parameters used in the calculation of an x-ray scattering pattern. In a least-squares refinement, one attempts to find the values for these parameters that minimize the difference between observed structure factor amplitudes and those calculated from any particular model or technique. We first illustrate this in the general case, and then show the specific application to isomorphous heavy atoms.

The experimental data are measured structure factor amplitudes $|F_o|$. The calculated $|F_c|$ values usually come from Equation 13-70. They are a function of all the structural parameters of the tentative model. These are the *x*, *y*, and *z* coordinates of each atom, and the atomic number of each atom.

In addition, for high-resolution structures, there is another effect we must worry about. Atoms are not fixed in space, even in a crystal. They are vibrating, and the amplitudes will vary for each atom. The x-ray scattering will be an average of the position of each atom. It can be shown that, for isotropic thermal motion, the atomic scattering factor will have the form $f = f_0 e^{-\beta |S|^2/4}$, where *S* is the scattering vector, and β is related to the mean square amplitude of the atomic vibration, $\langle \mu \rangle$, by $\beta = 8\pi^2 \langle \mu \rangle^2$. This relation introduces another parameter. The thermal factor β can be guessed from knowledge of the atom type, but in the most rigorous structure determination it too will be a variable. Furthermore, real vibrations are anisotropic and thus must be represented by a thermal ellipsoid defined by six parameters. So a total of anywhere from three to nine parameters, P_j , are needed for each atom; a very large number (*n*) of parameters are needed for the entire asymmetric unit.

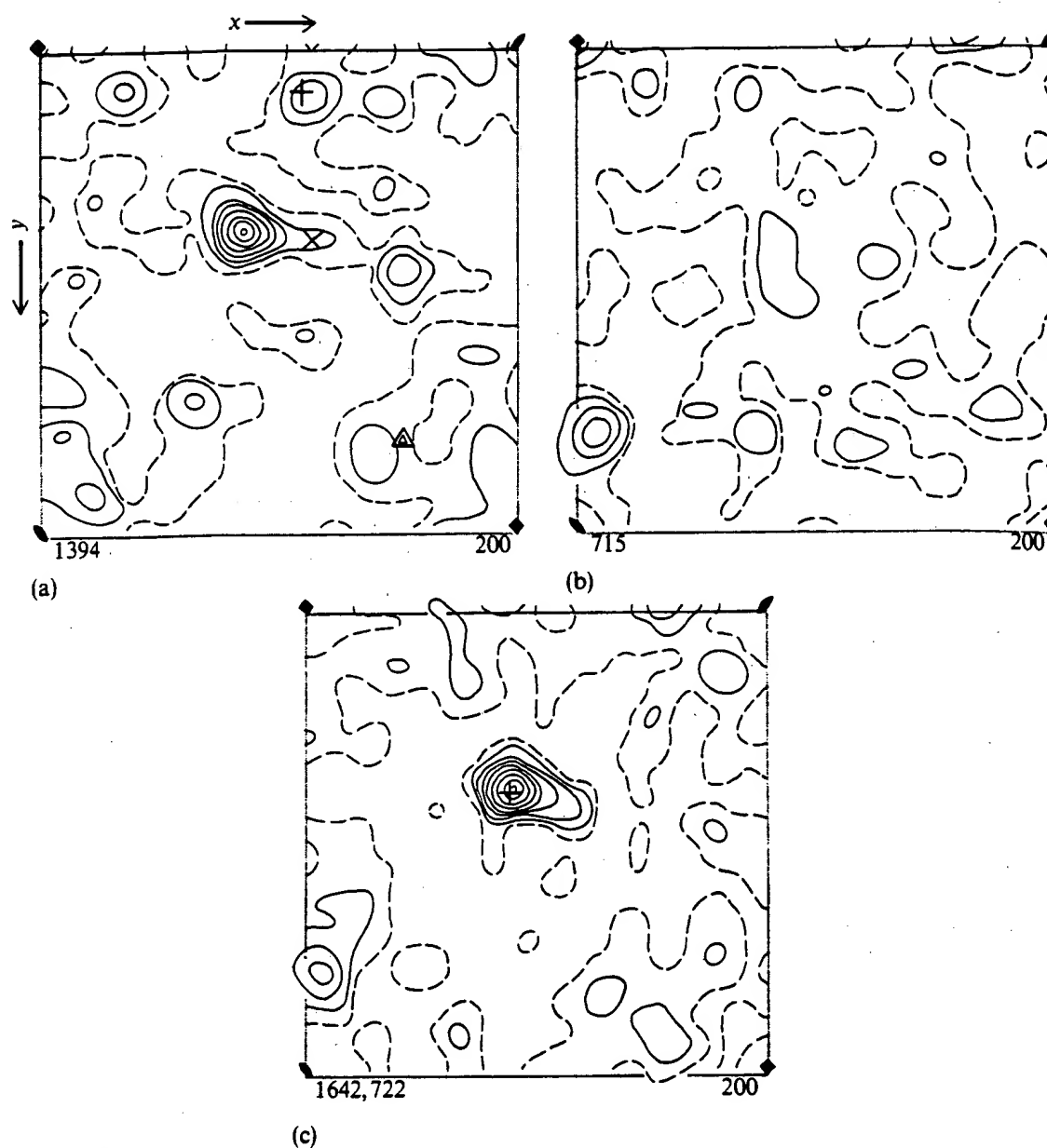


Figure 13-38

Cross-phase difference Fourier maps, calculated for the same crystals of cytochrome *c* as those illustrated in Figure 13-36. All three maps are on the same scale; contours are indicated at lower right; heights of major peaks are indicated at lower left. The origin is at upper left; only one-half a unit cell in each direction is shown. (a) Difference map calculated with Pt amplitudes and protein phases determined from Hg derivative. A true Pt site is indicated by X, a questionable site by +, and a false site by Δ . (b) Difference map calculated with Hg amplitudes and protein phases calculated for Pt derivatives. The mercury site is at lower left. (c) Map for double derivative, using average protein phases from several sets of metal derivatives. [From R. E. Dickerson et al., *J. Mol. Biol.* 29:77 (1967).]

In a least-squares refinement, one wants to adjust these parameters to minimize the difference between observed and calculated structure factor amplitudes. In practice, the actual quantity minimized is

$$D = \sum_{h=-\infty}^{\infty} \sum_{k=-\infty}^{\infty} \sum_{l=-\infty}^{\infty} W_{hkl} [|F_o(h, k, l)| - |\kappa F_c(h, k, l)|]^2 \quad (13-108)$$

where W_{hkl} is a weighting factor measuring one's estimate of the reliability of a given experimental or calculated point, and κ is a scaling parameter. For each parameter P_j , one establishes the condition $\partial D / \partial P_j = 0$. This leads to n equations in the n unknown parameters. Solving these equations simultaneously produces the least-squares fit.

For an example of how such a calculation is set up in matrix form, see Section 8-1. The important thing is that an $n \times n$ matrix must be inverted. For linear equations, a single matrix inversion suffices. However, the equations that result from differentiating Equation 13-108 are not linear in the unknown parameters. Therefore, an iterative technique must be used. This involves inverting an $n \times n$ matrix, taking the resulting parameters, reinserting them into the equations, and repeating the matrix-inversion process. This routine is performed over and over again until the parameters converge on values that minimize D .

Least-squares refinement of heavy-atom positions

In the isomorphous replacement technique, $|F_P|$ and $|F_{PH}|$ have been measured, F_H has been calculated from an estimate of the heavy-atom positions, and ϕ_P has been calculated as described earlier. If all these results were correct, then F_{PH} , F_P , and F_H would form a triangle as shown in Figure 13-34. However, because of errors, the triangle usually is not closed.

We can calculate the structure factor expected for the heavy-atom derivatives as

$$F_{PH(\text{calc})} = |F_H|e^{i\phi_H} + |F_P|e^{i\phi_P} \quad (13-109)$$

To improve the location of the heavy atoms, one attempts to minimize the difference between the amplitude of this calculated structure factor and the observed amplitudes. The equation used, by analogy to Equation 13-108, is

$$D = \sum_{h=-\infty}^{\infty} \sum_{k=-\infty}^{\infty} \sum_{l=-\infty}^{\infty} W_{hkl} [|F_{PH}(h, k, l)| - |F_{PH(\text{calc})}(h, k, l)|]^2 \quad (13-110)$$

This minimization is done by allowing the heavy-atom positions and the thermal parameters to vary.

Such an approach is not necessarily the best one for every crystal, and alternative approaches are discussed by Blundell and Johnson (1976).

Once the heavy-atom positions have been refined, they are used to calculate a final set of phases for the parent crystal. Then, at last, the stage is set for a Fourier synthesis of the entire structure using Equation 13-93.

Anomalous dispersion of heavy atoms

One additional technique for exploiting the presence of heavy atoms has seen increasing use in protein and nucleic acid crystallography. This technique is anomalous dispersion. It occurs when the frequency of the x rays used falls near an absorption frequency of an atom. In practice, the technique is most useful for atoms heavier than sulfur.

Until now we have treated the atomic scattering factor f as a real number. In actuality, f is a complex number because the phase shift upon scattering is not necessarily an integral or half-integral number of oscillations:

$$f(S) = f_0(S) + if'_0(S) \quad (13-111)$$

The term f'_0 is significant only when the x-ray frequency is close to an atomic absorption frequency. It is related to the extinction coefficient of that particular atomic absorption.

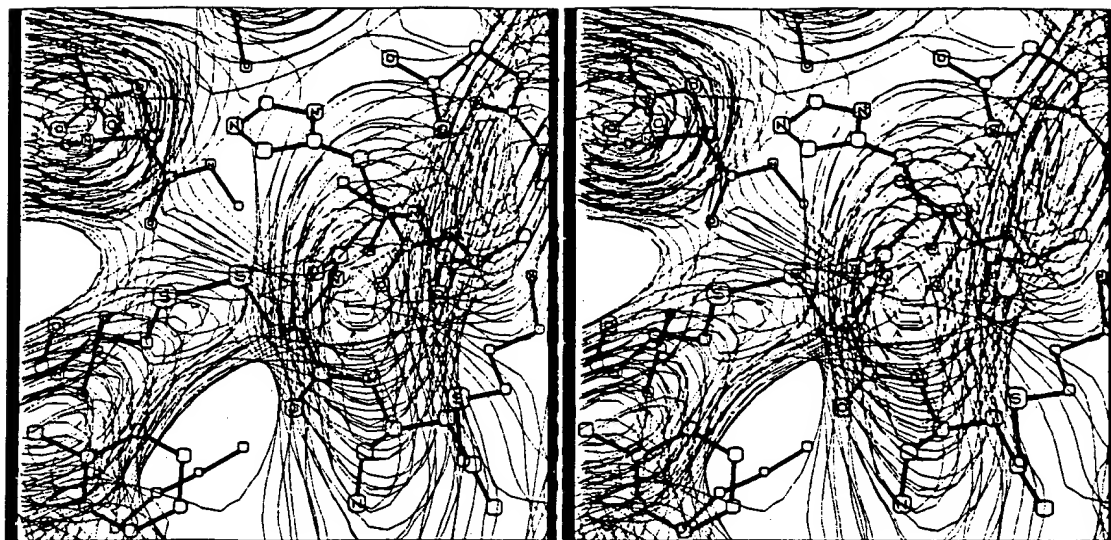
When $f(S)$ was considered to be real, one of the implications was Friedel's law. From Equation 13-18b, for parent-crystal atoms unaffected by anomalous dispersion, we can write

$$|F_P(h, k, l)| = |F_P(-h, -k, -l)| \quad (13-112)$$

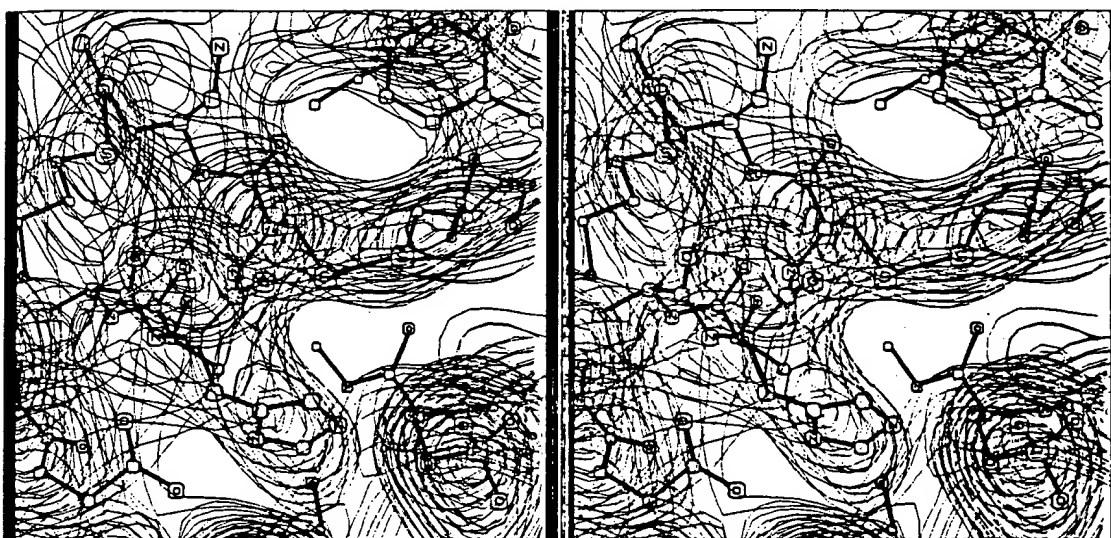
However, for crystals containing heavy atoms, this relationship no longer holds. The breakdown of Friedel's law can be used in a number of different ways (see Blundell and Johnson, 1976). For example, suppose two different x-ray frequencies are used, one allowing anomalous dispersion and one not. The difference in scattered intensities should represent the anomalous scattering, and this is restricted to the heavy atom. Then an analog of the isomorphous methods described above can allow calculation of phases.

Interpretation of the electron density map

Here we describe some typical stages in the solution of the crystal structure of a protein (see Fig. 13-39). Several heavy-atom derivatives have been prepared and located. Isomorphous replacement has been used to estimate phases for all $F_P(h, k, l)$, and an electron density map has been calculated using these phases and all data to a certain resolution. The resolution chosen will be a function of the order of the actual crystal and of how isomorphous the derivatives are. Reliable phases are needed



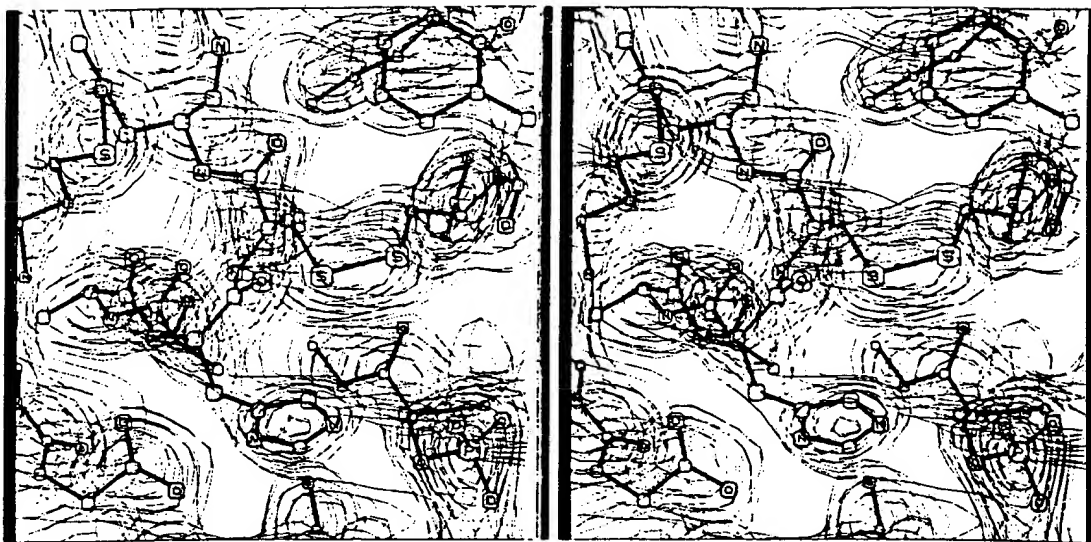
(a)



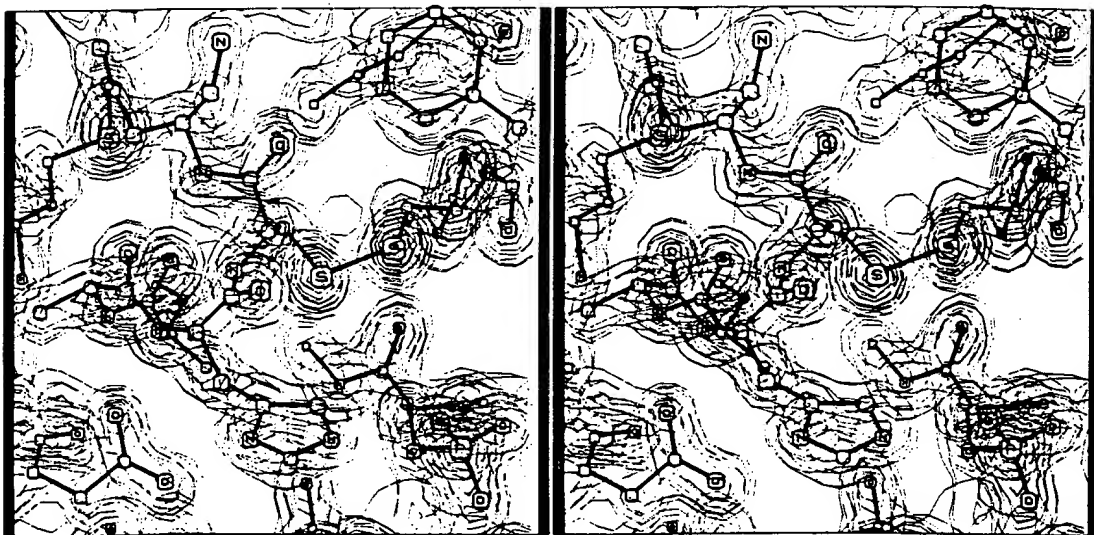
(b)

Figure 13-39

Protein electron density maps as a function of resolution. The maps are calculated from measured intensities and estimated phases. The protein is a diisopropyl fluorophosphate derivative of bovine trypsin. The view is down the y axis of the active site. A ball-and-stick model of the *final* best estimate of the structure is repeated in each map; note the phosphate at lower right and the active-site histidine at lower center; above these two features is a disulfide bond. (a) A map at 6.0 Å resolution, contoured



(c)



(d)

from $0.05 e \text{ \AA}^{-3}$ in steps of $0.05 e \text{ \AA}^{-3}$ (b) A map at 4.5 \AA resolution, contoured from $0.10 e \text{ \AA}^{-3}$ in steps of $0.10 e \text{ \AA}^{-3}$. (c) A map at 3.0 \AA resolution, contoured from $0.35 e \text{ \AA}^{-3}$ in steps of $0.30 e \text{ \AA}^{-3}$. (d) A map at 1.5 \AA resolution, contoured from $0.50 e \text{ \AA}^{-3}$ in steps of $0.50 e \text{ \AA}^{-3}$. All maps are shown as stereo pairs. [Courtesy of John L. Chambers. For further details, see his unpublished Ph.D. thesis, Calif. Institute of Technology, 1977.]

to justify the vastly increasing effort of using more and more scattering data in an attempt to obtain higher resolution.

If the result is around a 6 Å map, the macromolecule usually appears as a blob of electron density; Figure 13-39a shows a typical example. At this resolution, it usually is impossible to recognize the polymer chain backbone for a protein or nucleic acid.

Even at 6 Å resolution, however, considerable useful information emerges. One can learn a fairly detailed shape, and can spot crevices or subunits; α helices will appear as rods. If heavy-atom-labeled ligands or substrates are available, difference Fouriers can allow determination of the locations of their binding sites. If these results seem reasonable, it usually is worthwhile to attempt to proceed to higher-resolution analysis, providing that the quality of the data on available isomorphous derivatives justifies this.

At 3.0 Å resolution, it is possible to trace the path of the polymer chain backbone (Fig. 13-39c). In a protein, only the large amino acid side chains show up as discrete density peaks. It would be difficult to construct a meaningful molecular model at this stage. In nucleic acids, double helices will show up readily.

At 2.5 Å resolution, almost all protein side chains are visible. The carbonyl group of each peptide shows up as a protrusion from the main chain, and so it is possible to fix the orientation of each peptide plane.

If the amino acid sequence is known, one can begin to construct a model of the protein. Various techniques exist for doing this. The simplest is a Richards box, which uses a half-silvered mirror to superimpose a wire model of the structure onto a pile of lucite sections where the electron density map is plotted. Coordinates for atoms then are read off the model. Newer methods use computer searches to trace the most likely continuous paths of electron density and fit a peptide chain to these. Note that both approaches have the built-in assumption that the geometry of the peptide chain (except for dihedral angles) is known. This is a far cry from high-resolution small-molecule x-ray crystallography, where one determines bond lengths and angles *de novo*.

The original fit of the peptide chain to the electron density map at 2.5 to 3.0 Å will not be very precise. Many groups cannot be centered on the electron density peaks that presumably represent them. (See Fig. 13-39c for a typical example.) However, the preliminary model now can be used for one or more cycles of refinement. For example, in real-space refinement, one adjusts the model to try to minimize the difference between $\rho(x, y, z)$ calculated from the x-ray data and $\rho(x, y, z)$ calculated from the model. Alternatively, one can use Fourier refinement or least-squares techniques.

At higher resolution, individual atoms begin to be seen (see Fig. 13-39d for an example of a 1.5 Å map). Here it is actually possible to identify many amino acid side chains directly from the electron density map. In fact, crystal-structure work has revealed a number of serious errors in predetermined amino acid sequences. The more side chains one can see, the more accurate a model one can build and, in turn, the more likely it is that a further improvement in the electron density map can result from additional refinement.

Energetics of protein conformations in interpretation of the electron density map

A question of serious concern among crystallographers is how much knowledge about conformational analysis of proteins should be incorporated into the process of solving crystal structures. As shown in Chapter 5, we know with fair likelihood what ranges of dihedral angles are preferred by peptides. We know much about the forces that govern the interactions of nonbonded residues. Given a trial structure determined from a Fourier synthesis, this conformational knowledge could, by an energy minimization, be used to compute a structure more consistent with the body of acquired thermodynamic information.

M. Levitt and R. Diamond have shown that alternate cycles of Fourier and conformational energy refinement can be synergistic and can lead to convergence to a better structure. This is reasonable. The fact that a crystal forms implies that it must be in a crystal-wide free energy minimum. Alternatively, one can use conformational energies, not to try to obtain a minimal energy structure, but just as a guide on how to shift atoms slightly in the trial structure. A shift that simultaneously improves the fit of that atom to the calculated electron density map and also lowers the conformational energy is likely to be a step in the right direction.

Difference Fourier syntheses in studying ligand-macromolecule interactions

Difference Fouriers are extremely useful for comparing two structures. For example, the difference Fourier map of an isomorphous derivative and the parent should contain just the electron density of the added heavy atoms, as discussed earlier. Similarly, difference Fouriers have been used to locate substrate-binding or ligand-binding sites on proteins. Here the idea is to measure the diffraction intensities of the liganded protein. Then one calculates a difference Fourier using these measured intensities and calculated phases of the unliganded protein. The result can be just the electron density of the bound ligand, plus any difference in density due to changes in structure induced by the ligand binding. Naturally, the technique will work only so long as these differences are not too large.

The difference Fourier technique for locating a bound ligand works well because the presence of the ligand changes the phase of most structure factors relatively little. We can write (by analogy to Eqn. 13-102)

$$F_{PL} = F_P + F_L \quad (13-113)$$

where PL stands for the parent-ligand complex, and F_L is the structure factor of the ligand. Figure 13-40 shows this vector equation graphically. Here, F_P is known, and $|F_{PL}|$ is known. As long as $F_L < F_P$ and $F_L < F_{PL}$, the possible values of F_{PL} must lie within a small range of phase angles. Thus, as a first approximation, the parent phase ϕ_P is a good estimate of ϕ_{PL} .

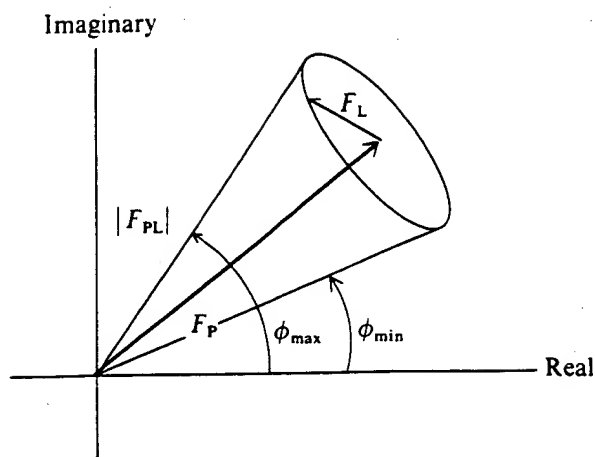


Figure 13-40

Effect on observed structure factors of an added ligand. The parent-crystal structure factor F_P is presumed to be known. Then, so long as the ligand structure factor $|F_L|$ is small, the phase of F_P is a good approximation of the phase of the ligand complex, F_{PL} .

A difference Fourier map thus can be calculated by analogy to Equation 13-107:

$$\Delta\rho(x, y, z) = (1/V) \sum_{h=-\infty}^{\infty} \sum_{k=-\infty}^{\infty} \sum_{l=-\infty}^{\infty} [|F_{PL}(h, k, l)| - |F_P(h, k, l)|] e^{i\phi_P(h, k, l)} e^{-2\pi i(hx + ky + lz)} \quad (13-114)$$

This map will show peaks that correspond to the position of the bound ligand. It also will show adjacent positive and negative regions of electron density that correspond to the movement of an atoms induced by ligand binding. Figure 13-41 shows this schematically in the one-dimensional difference Fourier.

An explicit justification for the validity of the difference Fourier map in representing the structure of the bound ligand can be seen by examining a centrosymmetric projection. The true structure of the bound ligand is

$$\rho_L(x, y, z) = (1/V) \sum_{h=-\infty}^{\infty} \sum_{k=-\infty}^{\infty} \sum_{l=-\infty}^{\infty} |F_L(h, k, l)| e^{i\phi_L(h, k, l)} e^{-2\pi i(hx + ky + lz)} \quad (13-115)$$

We need to know how well $|F_L|e^{i\phi_L}$ is approximated in Equation 13-114 by $||F_{PL}| - |F_P||e^{i\phi_L}$. In the centrosymmetric case as long as $|F_L|$ is small, Equation 13-114 is exact, as you can see by applying the same arguments used in Figure 13-35. For the general case, it is known that Equation 13-114 will correctly represent the electron density of the ligand, except that the peaks will be only half the correct height, and that there will be some noise in the data.

Much of our knowledge about the structure of enzyme active sites comes from difference Fourier calculations on crystals containing bound substrates or bound

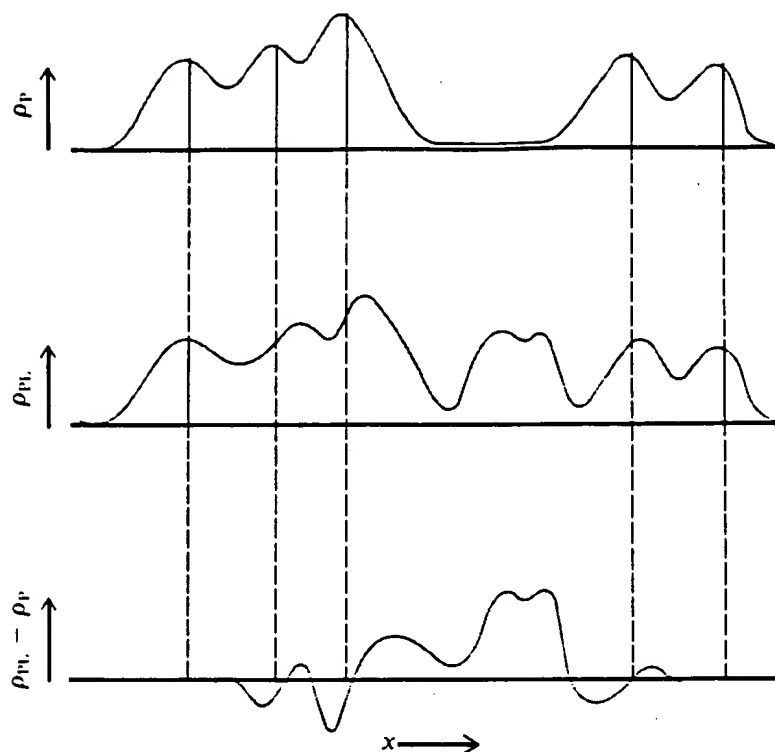


Figure 13-41

Using difference Fourier syntheses to study ligand binding. Such syntheses can be used to identify ligand binding sites and any conformational changes that accompany addition of the ligand. Shown are one-dimensional schematic drawings of the parent electron density map (ρ_P), the map that would be computed by solving the structure of the ligand complex (ρ_{PL}), and a difference Fourier ($\rho_{PL} - \rho_P$) that could be calculated in a relatively simple fashion (see text). Note that ligand atoms simply lead to increased density, whereas atom movements yield adjacent peaks and troughs in the difference Fourier. [After T. L. Blundell and L. N. Johnson, *Protein Crystallography* (London: Academic Press, 1976).]

inhibitors. The availability of this technique means that, in many cases, the determination of a macromolecular crystal structure is not so much the end of a massive effort as it is a starting point in the study of macromolecular function.

Summary

The x-ray scattering from an atom depends on its position in space and on the number of electrons it contains. The x-ray scattering from an array of atoms can be computed by summing the contributions of individual atoms. Periodic arrays of identical atoms restrict the observation of significant scattered intensity to only a discrete set of experimental geometries. Arrays of molecules can be treated in the same way as

arrays of atoms. A crystal is a three-dimensional periodic array that consists of a unit cell replicated in space. The vertices of the cell define a crystal lattice. The periodicity of the array restricts observable scattering to a very limited set of geometries, which form the reciprocal lattice of the crystal.

The x-ray scattering can be described as the Fourier transform of the electron density of the object that generated it. Thus, if one could measure both the phase and the intensity of the scattered radiation, one could directly perform an inverse Fourier transfer and reproduce the structure. Unfortunately, all one can measure is the intensity. In principle, the pattern of scattered intensities still contains sufficient information to reconstruct the array that generated it. However, this information is not as easy to use or interpret. The inverse Fourier transform of the scattered intensity is called the Patterson function. It is a map of all interatomic vectors. Thus, if the structure contains n atoms per unit cell, there will be n^2 vectors per unit cell of the Patterson function.

The structure of macromolecular crystals usually is solved by the technique of multiple isomorphous replacement. Heavy-metal derivatives of a parent crystal are prepared, and the scattered intensities of the parent and the derivatives are compared. A difference Patterson map calculated directly from the intensities mostly shows just heavy atom-heavy atom vectors. This allows a preliminary estimate of the heavy-atom positions. Using these positions and the differences between scattered intensities of the parent crystal and the derivatives, it is possible to estimate the phase of the scattered radiation. Once this estimate is available, the estimates of the heavy-atom positions can be made more precise. The procedure is repeated, or other refinement techniques are used. Finally, phases are available accurate enough to use in conjunction with the measured intensities to compute an image of the structure.

Problems

- 13-1. Calculate the x-ray structure factor of the array of identical atoms shown in Figure 13-42, and compare it with the calculations in the text for similar arrays. Extend the result to the infinite array. Atoms are shown as circles, lattice points as dots.

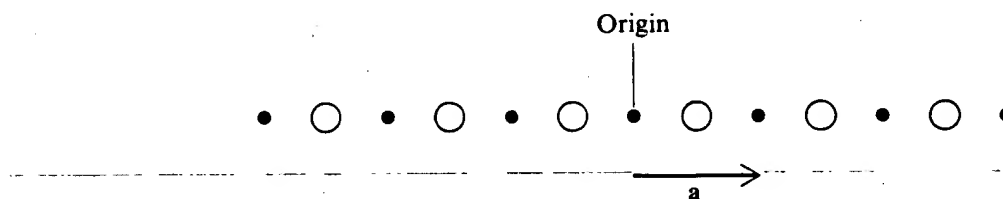


Figure 13-42

Array of atoms for Problem 13-1.

- 13-2. Calculate the x-ray scattering intensity expected from the infinite two-dimensional crystal shown schematically in Figure 13-43, where $|a| = R$, and $|b| = 4R$. You may

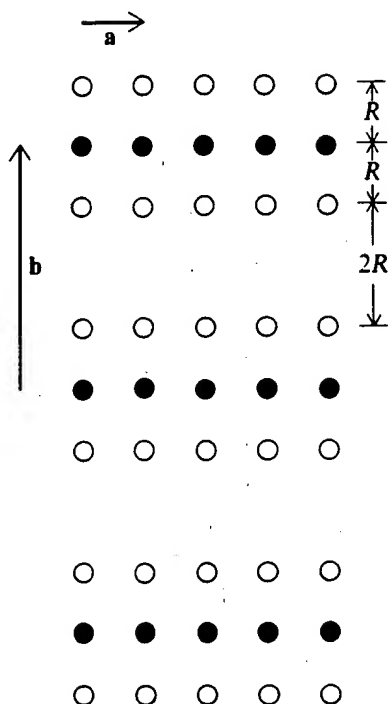


Figure 13-43

Crystal array for Problem 13-2.

assume that the atomic scattering factor of the central atom of each molecule is twice that of the other two atoms. Ignore the dependence of f on S . You should be able to demonstrate that, if the intensity is plotted on the reciprocal lattice, it is constant for all values of h but varies periodically with k , such that the strongest intensity is seen for $k = 0, 4, 8, \dots$, and the weakest for $k = 2, 6, 10, \dots$. HINT: Calculate the reciprocal lattice; calculate the scattering expected for one molecule placed at the origin; then use the principles of convolutions to compute the structure factor of the crystal; finally, square the amplitude to calculate the intensity. [This problem was adapted from one suggested by Bruno Zimm.]

- 13-3. Starting from the vector diagram in Figure 13-34, derive the following expression for the difference between the amplitude of the parent crystal (P) and that of a heavy-atom isomorphous derivative (PH):

$$|F_{PH}| - |F_P| = |F_H| \cos(\phi_{PH} - \phi_H) - 2|F_P| \sin^2[(\phi_P - \phi_{PH})/2]$$

Under what conditions can a comparison of the differences in observed intensities be used to obtain a good estimate of the heavy-atom structure-factor amplitude $|F_H|$?

- 13-4. Draw the molecule that would produce the Patterson map shown in Figure 13-44. (Assume that all atoms are equal.) If you can't see how to do this, first choose a few arbitrary

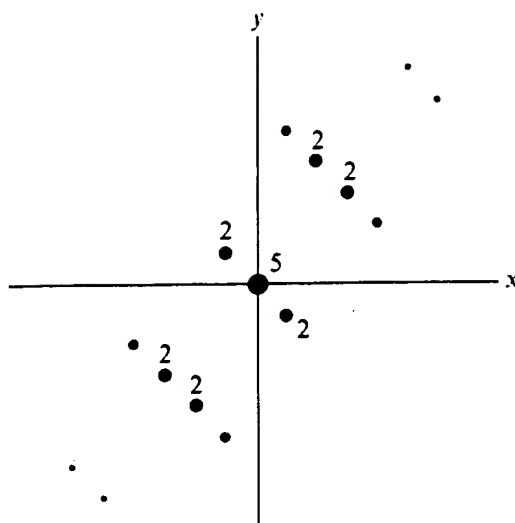


Figure 13-44

Patterson map for Problem 13-4.

small molecules and construct their Patterson maps. Multiple-weighted peaks are indicated in the figure; others have a weight of one.

- 13-5. A one-dimensional crystal has a unit cell 4 Å long. Measured x-ray scattering intensities—ignoring the dependence of $f(S)$ on S —are shown in Table 13-4. An isomorphous “heavy”-atom derivative can be prepared, in which one atom with an atomic scattering factor of 5 is added per unit cell; its scattering intensities also are shown in the table.

Table 13-4

Measured x-ray scattering
intensities for problem 13-5

h	$ F_P(h) ^2$	$ F_{PH}(h) ^2$
0	49	144
1	5	20
2	25	0
3	5	20
4	49	144
5	5	20
6	25	0
7	5	20
\vdots	\vdots	\vdots

- a. Try to find the location of the heavy atom by using $|F_H| \cong ||F_{PH}| - |F_P||$ in a difference Fourier synthesis. Convince yourself that only the diffraction spots at $h = 0, 1, 2, 3$ need be considered. Assume for the moment that all phase terms are $+1$, and perform the calculation only for $x = 0, R/4, R/2$, and $3R/4$, where R is the length of the unit cell.

- b. Because the result in part a gives two intensity maxima as possible positions for the heavy atom, calculate the contribution each makes to the structure factor. Use the *phases* calculated from each position, along with the *intensities* estimated as in part a, to repeat the difference Fourier. Is there any improvement?
 - c. Because the information that $|F_H| = 5$ has been given, use the isomorphous replacement replacement technique outlined in the text to estimate the phases of $|F_P(h)|$ for the two possible positions of the heavy atom. Now, using the criterion that $\rho(x)$ must be real for all x , select among these phases for four acceptable choices, and perform a Fourier synthesis of the $|F_P(h)|$ data to yield the structure. Note that each synthesis produces the same structure, except for changes in the origin of the unit cell and the direction of positive x .
-

References

GENERAL

- Blundell, T. L., and L. N. Johnson. 1976. *Protein Crystallography*. London: Academic Press. [An excellent up-to-date monograph.]
- Dickerson, R. 1964. X-ray analysis and protein structure. In *The Proteins*, 2d ed., vol. 2, ed. H. Neurath (New York: Academic Press), p. 603.
- Eisenberg, D. 1970. X-ray crystallography and enzyme structure. In *The Enzymes*, 3d ed., vol. 1, ed. P. D. Boyer (New York: Academic Press), p. 1.
- Glusker, J. P., and K. N. Trueblood. 1972. *Crystal Structure Analysis: A Primer*. London: Oxford Univ. Press. [A clear, elementary treatment.]

SPECIFIC

- Fraser, R. D. B., and T. P. MacRae. 1969. X-ray methods. In *Physical Principles and Techniques of Protein Chemistry*, part A, ed. S. J. Leach (New York: Academic Press).
- Guinier, A. 1963. *X-Ray Diffraction in Crystals, Imperfect Crystals, and Amorphous Bodies*. San Francisco: W. H. Freeman and Company. [An advanced mathematical treatise.]
- Lipson, H., and C. A. Taylor. 1958. *Fourier Transforms and X-Ray Diffraction*. London: G. Bell & Sons.
- Matthews, B. W. 1974. Determination of molecular weight from protein crystals. *J. Mol. Biol.* 82:513.
- Stout, G. H., and L. M. Jensen. 1968. *X-Ray Structure Determination: A Practical Guide*. New York: Macmillan.
-

TAB C

background if exposure is too short. A low-power microscope is also useful for judging color slides or black-and-white positives, but they should also always be projected.

To make a positive slide from a 35-mm negative it is useful to have a slide copier with bellows, to adjust magnification; a light box makes a reasonable light source. Exposure latitude is wide enough with high-contrast copy film so that once you have worked out the correct *f*-stop and exposure for your setup, you should not need to bracket exposures each time.

Another useful black-and-white film is Kodalith, either for 35-mm negatives or positives, or for 4 × 5 high-quality negatives for publication. The exposure latitude for producing a good negative is much narrower than for copy film, but once achieved it will produce good prints over a very broad range since the blacks are totally opaque. They may, however, show tiny clear pinhole defects which need to be blacked out on the negative.

Sources of Materials

For graphics supplies, including Formatt dot screen overlays, Pantone color overlay films both solids and % shades, Amberlith masking film (for color separations), stick-on register marks, Olfa or HT cutters with snap-off blades, etc.:

Graphic Supplies and Services
2166 Faulkner Road, N.E.
Atlanta, Georgia 30324
Charrette Corporation
31 Olympia Avenue
Woburn, Massachusetts 01801
A. I. Friedman
25 West 45th Street
New York, New York 10036

For Leroy lettering pens, high-quality tracing paper, drop bow pens, etc.:

Keuffel and Esser Co.
Morristown, New Jersey 07960

[25] Computer-Generated Pictures of Proteins

By ARTHUR M. LESK and KARL D. HARDMAN

Goethe wrote, "Architecture is frozen music." Molecular biologists find this an apt remark as they investigate themes and their variations and interactions in the architecture of proteins and nucleic acids. In this chapter we describe the applications of a computer program that draws stereoscopic pictures of biological macromolecules.¹ The program makes it easy to explore various ways of depicting a structure, including the free mixing in a single drawing of different styles of representation of different portions of a molecule, together with labels and comments.

Computer Graphics in Molecular Biology

The visual display of structures is a principal tool of computational molecular biology. The initial motives for applying computer graphics were the unwieldiness and instability of physical models and their readiness to denature, together with the fact that the space and material requirements increase as more structures appear. Recently, it has become clear that the real struggle is for intelligibility against the pressure of growing complexity. The structures being solved are increasing in size and accuracy as well as in number, and the questions we want to ask are increasing in subtlety.² Furthermore, although not all calculations are intrinsically pictorial, it is important to be able to *integrate* graphics into the operation of many computer programs. For example, it is frequently very useful to superpose pictures of two or more molecules in order to compare their structures, or to look at a "movie" of the course of a molecular dynamics simulation.

To design software it must be recognized that no single type of representation of a protein or nucleic acid structure is adequate for all purposes.^{3,4} Various modes of representing structures have been tried, both by draughtsman and computer. Initially there were attempts to reproduce the appearance of the physical models which the computer programs were

¹ A. M. Lesk and K. D. Hardman, *Science* **216**, 539 (1982).

² A. M. Lesk and K. D. Hardman, in "Supercomputers in Chemistry" (P. Lykos and I. Shavitt, eds.), p. 143. Am. Chem. Soc., Washington, D.C., 1981.

³ A. M. Lesk, *Trends in Biochem. Sci.* **6**, XIV (1981).

⁴ A. M. Lesk, "Introduction to Physical Chemistry," pp. 466 and 542. Prentice-Hall, Englewood Cliffs, New Jersey, 1982.

superseding. Thus some representations correspond to a fairly direct translation—atom by atom or bond by bond—of the structure into a picture.^{5,6} These are most useful for detailed analysis of a small portion of a large molecule, or the environment of a substrate or other small molecule bound to a large one.

The complexities of large structures have demanded an evolution of other representations, including abstractions. These include the schematic diagrams used first by A. Rossmann, A. Liljas, and B. Furugren, in which cylinders represent α -helices and arrows represent strands of β -sheet, and related representations which have been applied extensively by J. Richardson. Questions of the gross folding pattern, or topology, of a macromolecule are better served by these more abstract representations.

In order to gain the ability to produce stereoscopic diagrams, and to provide the flexibility essential to mix different representations in one picture, we have compiled into one coherent computer program the many ways of depicting biological macromolecules that have proved their utility. The options range from wire or skeletal models to schematic diagrams, or "cartoons." Any structural segment may be assigned a color, or may be drawn with broken rather than solid lines. The program can produce stereo pairs, and remove hidden lines whenever appropriate and desired.

Basic Operation of the Program

Line Drawings

Execution of the line-drawing version of the program may be divided into four phases: (1) Input of coordinates and picture composition information; (2) Creation of the geometry of the picture, in three-dimensional space; (3) Hidden-line removal, if desired; and (4) Projection into two dimensions, character generation, and output. For stereo pairs, steps 2, 3, and 4 are repeated for two orientations of the molecule (rotated by approximately 6° around an axis perpendicular to the line of sight).

The Input Phase. The program begins by reading the two input files: the coordinates, and the description of the contents and appearance of the picture. The picture composition file selects regions of a structure to draw, and specifies how they are to appear. This file is read in free-format

⁵ C. K. Johnson, "ORTEP: A Fortran Thermal-Ellipsoid Plot Program for Crystal Structure Illustrations," ORNL-3794 revised. Oak Ridge Natl. Lab., Oak Ridge, Tennessee, 1965.

⁶ C. K. Johnson, in "Crystallographic Computing" (F. R. Ahmed, S. R. Hall, and C. P. Huber, eds.), p. 227. Munksgaard, Copenhagen, 1970.

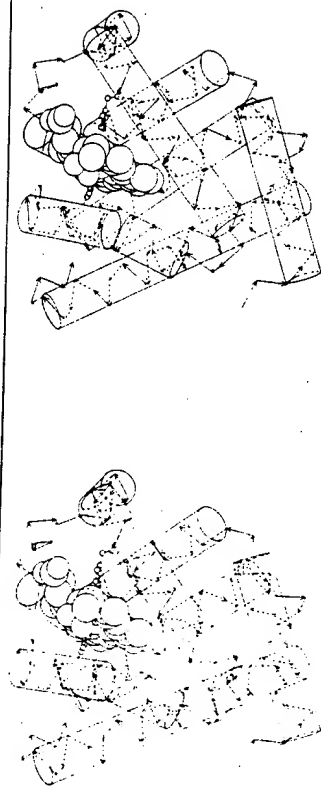


Fig. 1. Sperm whale myoglobin, showing the representation of helices as translucent cylinders, the tracing of the backbone by arrows linking successive C_α atoms, the heme group as an opaque space-filling model, and proximal and distal histidines as ball and stick models.

style, with keywords introducing lists of parameters. Sensible defaults are provided whenever possible. A user's manual describes the conventions.

Picture Generation. Next, the program prepares a picture by appropriate geometric transformations of coordinates into picture elements. For example, for each α -helix that is to be represented by a cylinder, the program generates a cylinder of appropriate size and orientation, by superposing the coordinates onto a standard polyaniline helix. Two sets of information about each cylinder are retained. First, the endpoints of the line segments that define its outline are placed in a file of draw commands.



Fig. 2. A halftone picture of the four-zinc insulin hexamer, viewed down the 3-fold axis.

Second, the surfaces of the cylinder, which are potentially opaque, are saved in a file of "windows" for a subsequent hidden-line removal step. (Windows may be open = transparent = inactive in hidden-line removal, or screened = active in hidden-line removal). Both drawing commands and window data are stored by pointers to a list of coordinates extracted from, or computed from, the initial atomic coordinates.

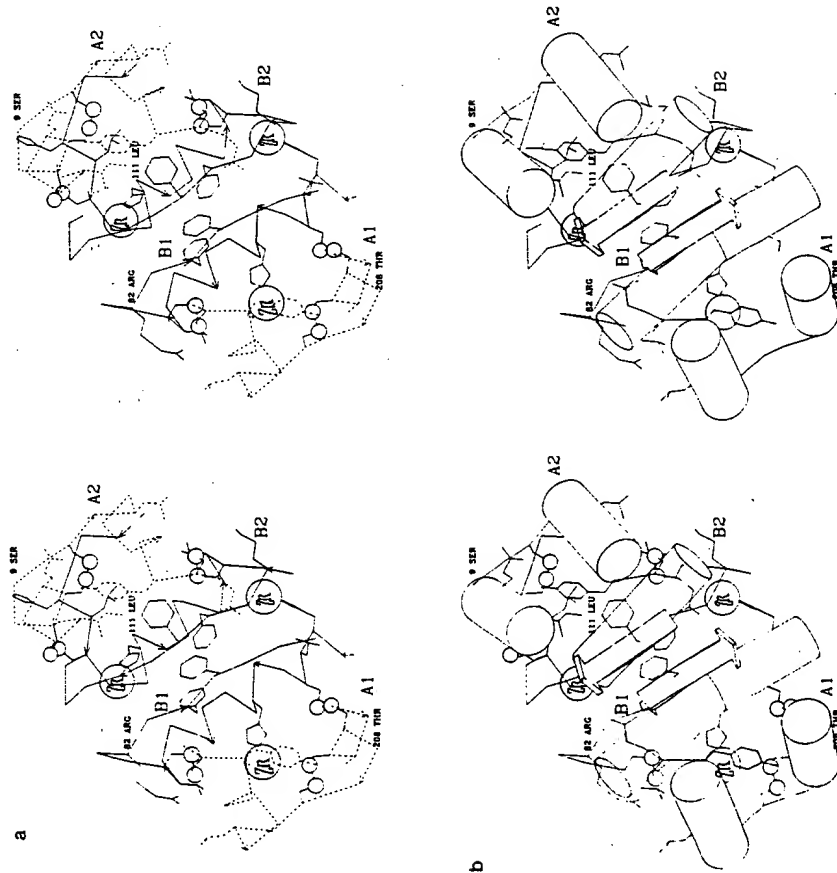


FIG. 3. Comparison of two representations of the dimer of four-zinc insulin, showing the backbone, selected side chains, disulfide bridges, and zinc atoms. Each monomer contains two polypeptide chains: A chains drawn with broken lines and B chains and disulfide bridges drawn with solid lines. The A1-B1 and A2-B2 monomers are related by an approximate (noncrystallographic) 2-fold axis perpendicular to the paper, and perpendicular to the crystallographic 3-fold axis shown in Fig. 2. (a) A predominantly linear drawing; (b) a schematic drawing.

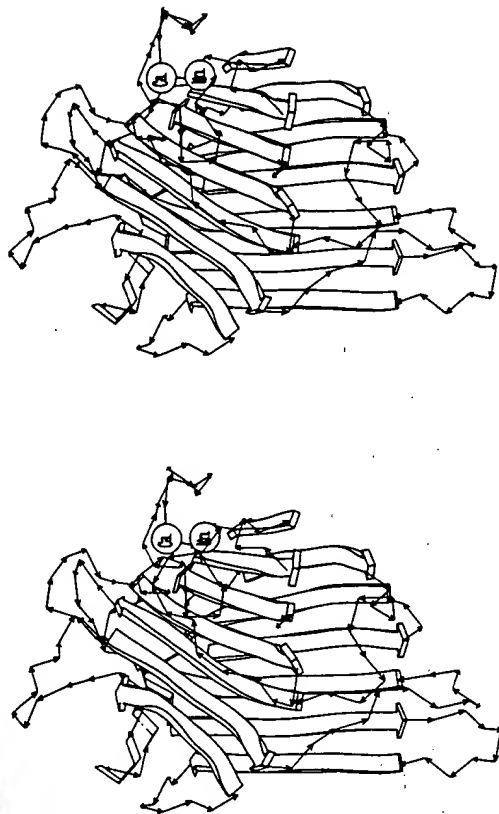


FIG. 4. Jack bean concanavalin A, a double- β -sheet protein containing manganese and calcium.⁷

All of the data at this stage are still in three-dimensional form. Indeed, we can "tap off" these data at this point in the computation, and send them directly to a three-dimensional display device.

Hidden-Line Removal. Some of the possible representations of sections of protein structures may have the appearance of solid objects, such as cylinders representing α -helices, or arrows representing strands of β -sheet. Only these representations generate windows for the hidden-line removal step; skeletal models do not. Associated with every potentially

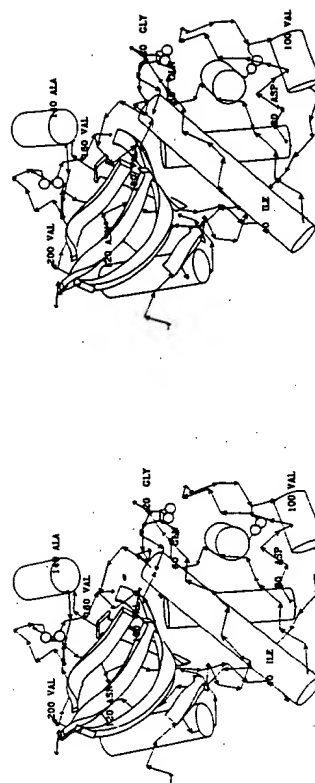


FIG. 5. Actinidin, a sulfhydryl protease.⁸

opaque element of the picture is an effective "optical density": the object may be regarded as *transparent*, *translucent*, or *opaque*. If it is transparent, lines passing behind it are left unchanged. If it is translucent, lines passing behind it are converted to dashed lines. If it is opaque, lines passing behind it are deleted entirely.

It is useful to be able to assign different optical densities to different portions of a protein. For example, to show the geometrical relationship between two occluding helices while deleting everything lying beyond the further helix, the front helix might be made translucent and the back helix opaque. It is possible to override hidden-line removal selectively: any object may be assigned the BURN attribute, in which case it will appear in the drawing even if it lies behind one or more opaque objects (these lines will be "burned through" the opaque material that lies in front of them).

In saving the data for hidden-line removal, it is important to ensure that objects do not obliterate themselves. To avoid this, and also to facilitate such options as BURN, there is a system of assignments of "immunity," by which certain lines are rendered immune from clipping by certain windows. This is a useful general technique for manipulating pictures.

The output from the hidden-line removal step is a modified set of draw commands. Certain "drawto's" have been converted to "moveto's" to effect the deletion of a line segment; conversion of solid lines to dashed lines (when a line segment passes behind a translucent object) is accomplished by changing an attribute of the line segment.

Output. After the hidden-line removal step, the line segments are projected to two-dimensional space. At this stage character strings are expanded to sets of line segments, via a set of stroke tables based on the Hershey fonts. The final output file contains only commands of the following three types: "MOVETO X Y," "DRAWTO X Y," and

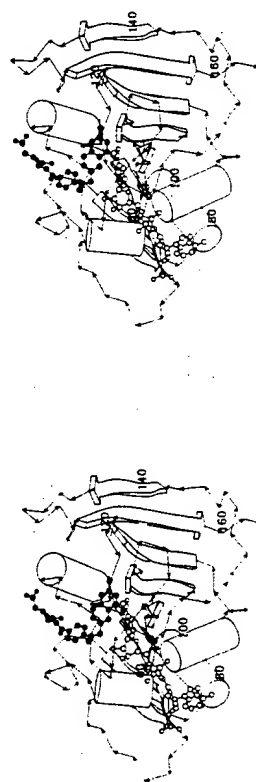


FIG. 6. The ternary complex of dihydrofolate reductase, cofactor NAD (light atoms), and inhibitor methotrexate (dark atoms).⁹

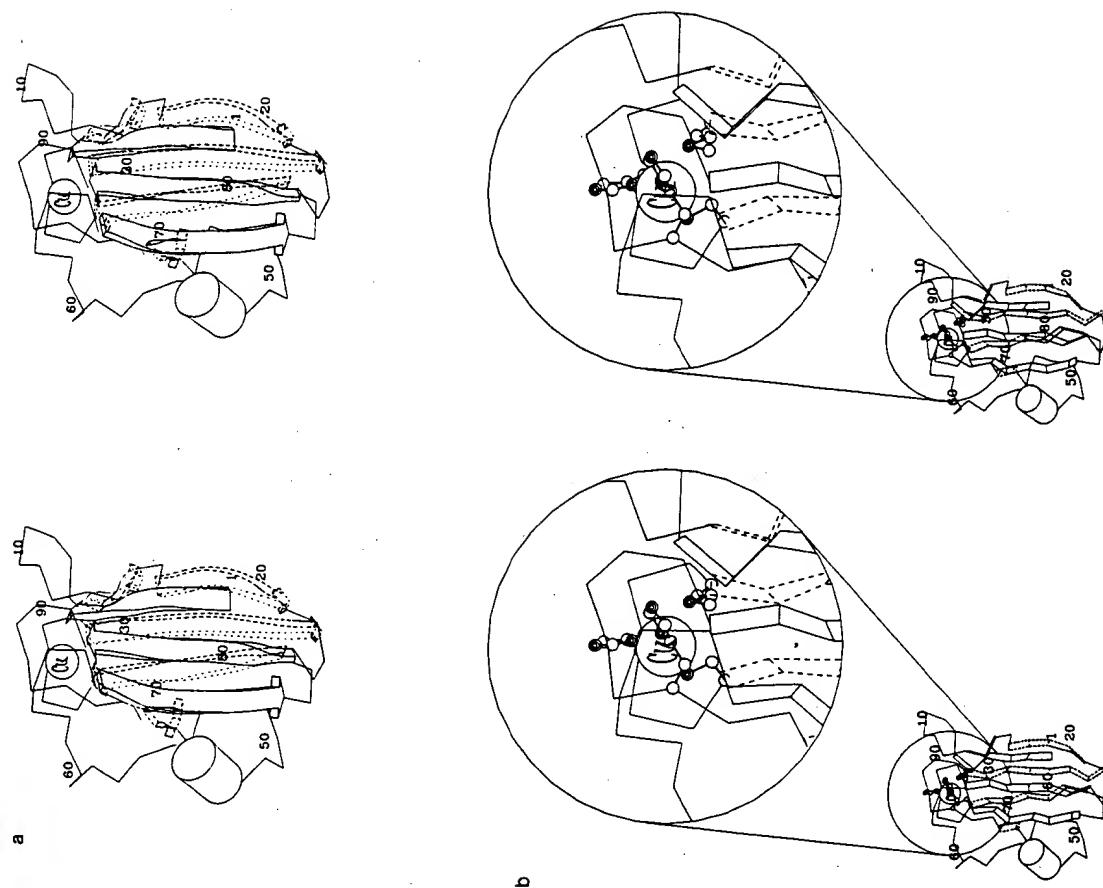


FIG. 7. Poplar leaf plastocyanin, a double- β -sheet protein containing a copper atom.¹⁰ The front sheet is drawn with solid lines, the back sheet with dashed lines. (a) Representation of sheets by ribbons, with a close-up view of the copper binding site. The copper ligands are His 37, Cys 84, His 87, and Met 92. Nitrogen and sulfur atoms of these side chains are darkened.

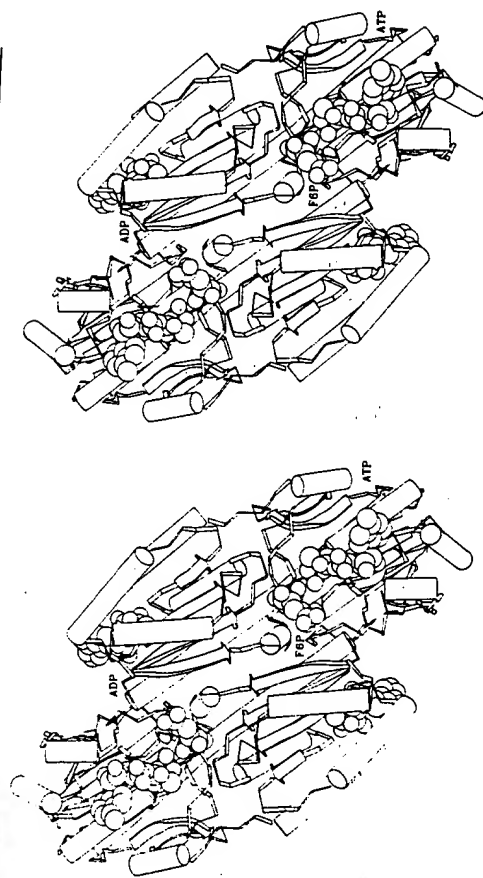


FIG. 8. Phosphofructokinase (R state), binding substrates ATP, and fructose 6-phosphate; and activator, ADP.¹¹ This view shows one dimer of a tetramer. There is a 2-fold axis perpendicular to the page.

"CHANGE PEN COLOR to n." The coordinates X and Y are scaled to a frame $0.0 \leq X, Y \leq 100.0$.

Color-Raster Output

To create color-raster output, an alternative step parallel to the hidden-line removal step is executed, in which the drawn lines are ignored

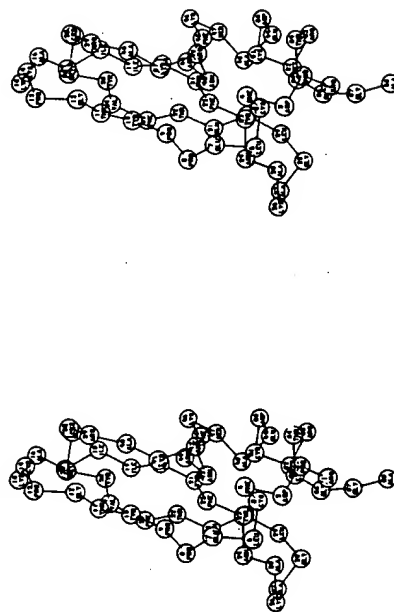


FIG. 9. Bovine pancreatic trypsin inhibitor, showing the amino acid sequence and backbone conformation.¹²

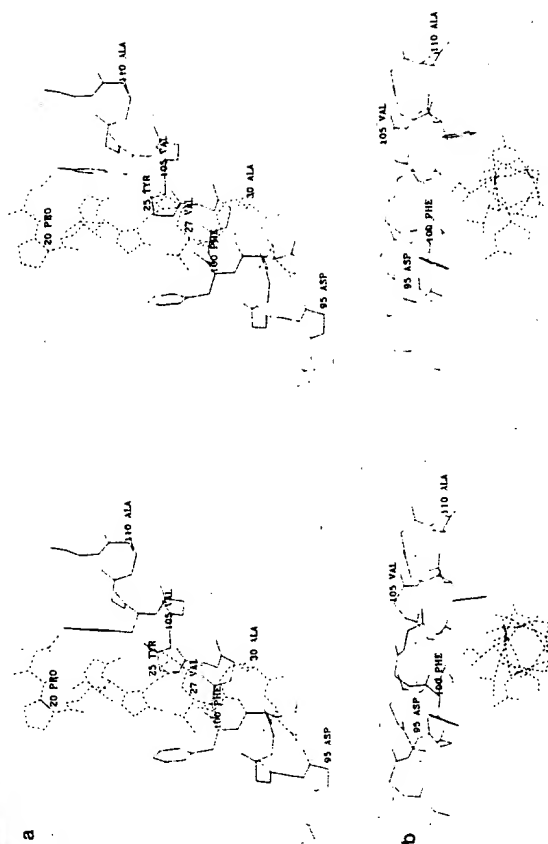


FIG. 10. The interdigitation and packing of side chains in the B-G helix contact in *Chironomus erythrocytorin*.¹³ B helix residues are drawn with solid lines, and G helix residues with broken lines. (a) and (b) Skeletal drawings of the two helices viewed in directions perpendicular and parallel to the contact between the helices. (c) Space-filling representation of the packing at the contact. Slices are drawn through spheres of the van der Waals radius around each atom. Several parallel planes are assembled in this picture. This figure may be compared to the hand-drawn version in Ref. 14, p. 248. (d) Overlay of the skeletal model onto the space-filling representation.

and the windows are painted in, on the basis of the user-assigned color and the reflected light intensity computed from the orientation of the window polygon relative to a simulated light source.

Examples

Figures 1-10 illustrate the use of various combinations of representations to portray a number of interesting structural features of proteins.^{6a-14}

^{6a} All pictures were photographed directly from computer output.

⁷ K. D. Hardman and C. F. Ainsworth, *Biochemistry* **11**, 4910 (1972).

⁸ E. N. Baker, *J. Mol. Biol.* **141**, 441 (1980).

⁹ D. A. Mathews, R. A. Alden, J. T. Bolin, D. J. Filman, S. T. Freer, R. Hamlin, W. G. J. Hol, R. L. Kisiuk, E. J. Pastore, L. T. Plante, N.-H. Xuong, and J. Kraut, *J. Biol. Chem.* **253**, 6946 (1978).

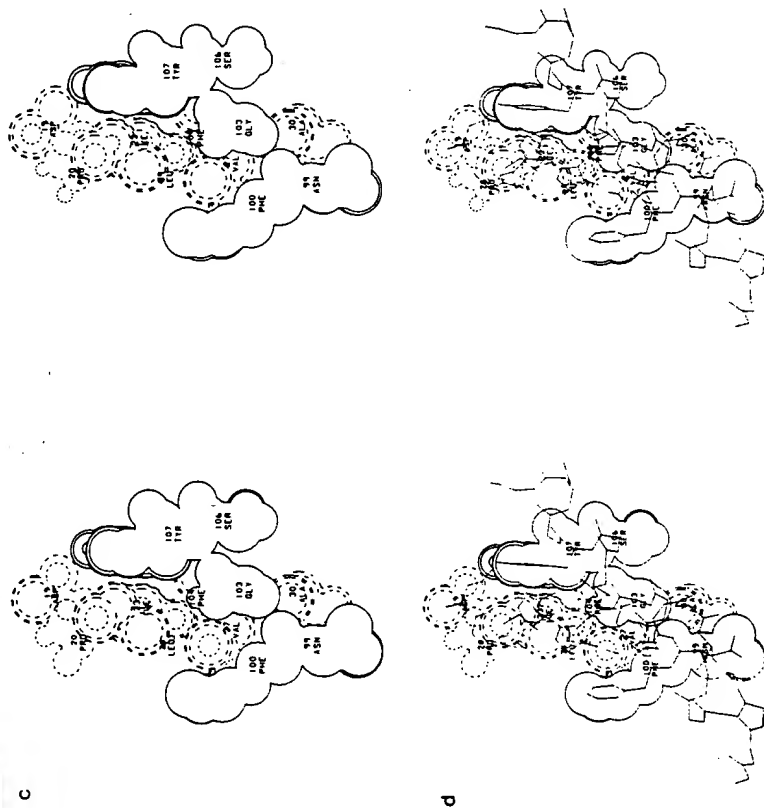


FIG. 10. (continued)

Acknowledgments

Work supported in part by the National Science Foundation Research Grant (PCM83-20171), the North Atlantic Treaty Organization Division of Scientific Affairs (RG275.80), the European Molecular Biology Organization (SF4-1980), and the Thomas J. Watson Research Center, IBM Corporation. A. M. L. is grateful to the Medical Research Council Laboratory of Molecular Biology for their hospitality during part of the time this work has been carried out. We thank Drs. P. R. Evans and M. C. Lawrence for their picture of phosphofructokinase.

- ¹⁰ P. M. Colman, H. C. Freeman, J. M. Guss, M. Murata, V. A. Norris, J. A. M. Ramshaw, and M. P. Venkatarappa, *Nature (London)* **272**, 319 (1978).
- ¹¹ P. R. Evans, G. W. Farrants, and P. J. Hudson, *Philos. Trans. R. Soc. London, Ser. B* **293**, 253 (1981).
- ¹² J. Deisenhofer and W. Steigemann, *Acta Crystallogr., Sect. B* **B31**, 238 (1975).
- ¹³ E. Weber, W. Steigemann, T. A. Jones, and R. Huber, *J. Mol. Biol.* **120**, 327 (1978).
- ¹⁴ A. M. Lesk and C. Chothia, *J. Mol. Biol.* **136**, 225 (1981).

[26] Macromolecule Backbone Models

By BYRON RUBIN

There has long been a need for a simple method for easily visualizing the conformations of biological macromolecules. X-Ray crystallographic reports generally provide lists of atomic coordinates and several diagrams of each protein. Without some means for using the atomic coordinates to construct other representations, however, the perception of a protein's structure is limited to those diagrams. Graphical representations, ribbon diagrams, cylinder and arrow figures, stereo drawings, and even xograph¹ illustrations (now Nimslo photographs)² are limited to a small number of views. Computer graphics systems³⁻⁶ overcome this problem, but the difficulty of stereo viewing and limited accessibility of these systems to the general scientific community suggest the need for a simpler alternative. The AMSON⁷ approach provides a large number of mono and stereo views of each protein in microfiche format. Its modest cost makes it attractive for a number of applications but it and the other graphical approaches to macromolecule structure display presently available fail to provide the ease of visualization which comes from a solid, three-dimensional model.

Construction of comprehensive models in which all of the nonhydrogen atoms in a macromolecule are shown,⁸⁻¹² however, is a large and

¹ R. A. Harte and J. A. Rupley, *J. Biol. Chem.* **243**, 1663 (1968).

² Nimslo Inc., Atlanta, Georgia 30340.

³ R. Diamond, "Bilder: A Computer Graphics Program for Biopolymers," International Symposium of Biomolecular Structure, Conformation, Function, and Evolution, Madras, Vol. 1, (Srinivasan Ramachandran, ed.), pp. 567-588, Pergamon, Oxford.

⁴ Evans and Sutherland Computer Corporation, 580 Arpeen Drive, Salt Lake City, Utah 84108.

⁵ R. Langridge, T. E. Ferren, I. D. Kuntz, and M. L. Connolly, *Science* **211**, 661 (1981).

⁶ E. F. Meyer, Jr., C. N. Morimoto, J. Villareal, H. M. Berman, H. M. Carrell, R. K. Stodola, T. F. Koetzle, L. C. Andrews, F. C. Bernstein, and H. J. Bernstein, *Fed. Proc., Fed. Am. Soc. Exp. Biol.* **33**, 2402 (1974).

⁷ R. J. Feldmann, "AMSON: Atlas of Macromolecular Structure on Microfiche," Tracor Jitco, Inc., Rockville, Maryland, 1976.

⁸ J. C. Kendrew, H. C. Watson, B. E. Strandberg, and R. E. Dickerson, *Nature (London)* **190**, 666 (1960).

⁹ Cambridge Repetition Engineers Ltd., Green's Road, Cambridge, England.

¹⁰ F. M. Richards, *J. Mol. Biol.* **37**, 225 (1968).

¹¹ Nicholson Models Labquip Inc., 18 Rosehill Park Estate, Caversham, Reading RG4 8XE, England.

¹² The Ealing Corporation, South Natick, Massachusetts 01760.